CHALMERS
UNIVERSITY OF TECHNOLOGY

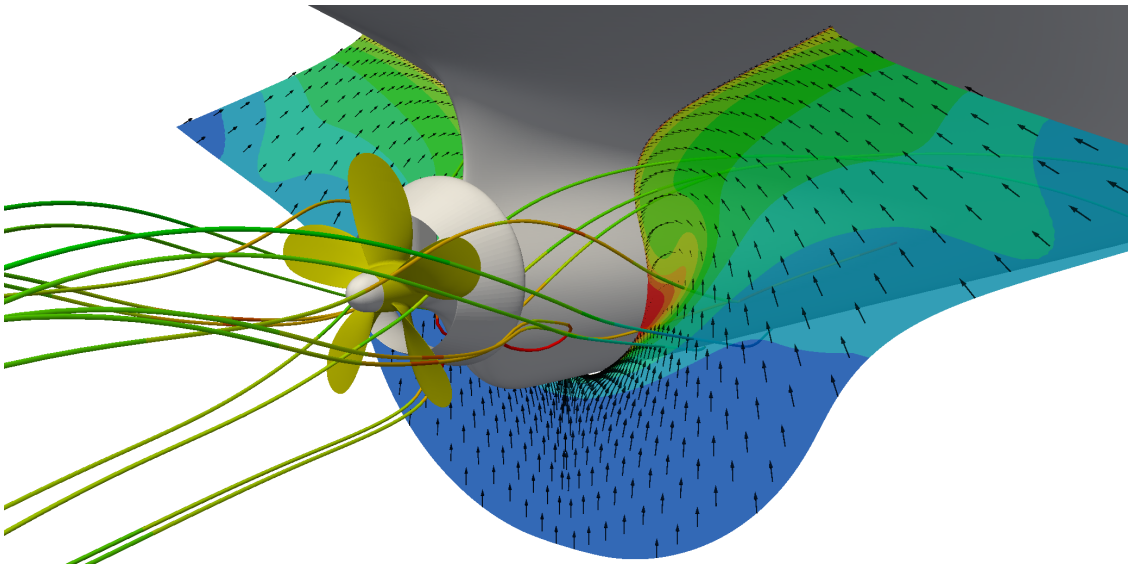

CFD Predictions of Resistance and Propulsion for the JAPAN Bulk Carrier (JBC) with and without an Energy Saving Device

Master's Thesis in the International Master's Program Naval Architecture and Ocean Engineering

KADIR BURAK KORKMAZ

Department of Shipping and Marine Technology
CHALMERS UNIVERSITY OF TECHNOLOGY
Gothenburg, Sweden 2015

Master's Thesis

X - 15/334

CFD Predictions of Resistance and Propulsion for the JAPAN Bulk Carrier (JBC) with and without an Energy Saving Device

KADIR BURAK KORKMAZ

CHALMERS
UNIVERSITY OF TECHNOLOGY

Department of Shipping and Marine Technology
Division of Marine Technology
Chalmers University of Technology
Gothenburg, Sweden 2015

CFD Predictions of Resistance and Propulsion for the JAPAN Bulk Carrier (JBC) with and without an Energy Saving Device
KADIR BURAK KORKMAZ

Examiner: Lars Larsson, Department of Shipping and Marine Technology

Supervisor: Lars Larsson, Department of Shipping and Marine Technology
Supervisor: Michal Orych, FLOWTECH International AB

Master's Thesis X - 15/334
Department of Shipping and Marine Technology
Division of Marine Technology
Chalmers University of Technology
SE-412 96 Gothenburg
Telephone +46 31 772 1000

Cover: Visualisation of the flow at the stern of the JBC with ESD

Printed by Chalmers Reproservice
Gothenburg, Sweden 2015

Resistance and Propulsion Predictions for JAPAN Bulk Carrier (JBC) with and without Energy Saving Device

KADIR BURAK KORKMAZ
Department of Shipping and Marine Technology
Division of Marine Technology
Chalmers University of Technology

Abstract

Resistance and propulsion predictions for a ship is one of the most important tasks at the design stage in order to ensure that the ship can sail at a desired speed with the installed engine capacity and fulfill the mandatory regulations imposed by IMO such as Energy Efficiency Design Index (EEDI). Since new concerns on environment and efficiency have risen, predictions are getting more important and as a result the interests on Energy Saving Device (ESD) increased significantly. Traditional prediction tools can provide reliable results for resistance and propulsion but it is time-consuming, expensive and most importantly, scaling problems cannot be eliminated. Since Reynolds similarity is not fulfilled at model test, flow characteristics in experiments differ significantly from full scale. On the other hand, Computational Fluid Dynamics (CFD) solves this problem by offering both model and full scale results with a great detail of flow fields. Nevertheless accuracy of CFD is still limited and accuracy obtained from computations is always a concern.

In this thesis, resistance, sinkage & trim, self-propulsion characteristics and local flow around the stern are predicted for the new test case JAPAN Bulk Carrier (JBC) for the Japan 2015 Workshop on CFD in Ship Hydrodynamics. Local flow is examined through mean velocity components, turbulent kinetic energy and Q-criterion at the stern region. Also, a comprehensive study is performed for revealing the best settings and procedures for POW tests and self propulsion tests using SHIPFLOW code. Free surface wave elevation, sinkage & trim are computed with the potential flow solver, viscous flow is evaluated by the Reynolds Averaged Navier-Stokes (RANS) solver. Propeller simulation is calculated through lifting line based propeller analysis module (LL) of SHIPFLOW. Additionally, a Verification and Validation (V&V) procedure is applied to the resistance, POW and self-propulsion results in order to assess the uncertainties and numerical errors.

Keywords: CFD, energy saving device, JBC, ESD , verification, validation, RANS , ship, hydrodynamics , SHIPFLOW

Acknowledgements

I would like to express my gratitude to my supervisors Professor Lars Larsson, for his valuable instructions and discussions, for his enthusiasm and willingness to help and Michal Orych at FLOWTECH International AB for his constant support and guidance. This thesis would not have been possible without the help of my supervisors.

Many thanks go to Rickard Bensow for providing me support and an office at the Department of Shipping and Marine Technology. The Chalmers Centre for Computational Science and Engineering (C^3SE) is also acknowledged for providing the computational resources.

Last but not least, my great appreciation goes to my friends for turning my two years of studies into unforgettable memories and experiences. Finally, I would like to express my deepest and warmest gratitude to my dear family for their never ending support and encouragement.

Kadir Burak Korkmaz, Gothenburg, May 2015

Contents

List of Figures

List of Tables

Nomenclature

Acronyms

Symbol	Description
CFD	Computational Fluid Dynamics
DNS	Direct Numerical Simulation
$EASM$	Explicit Algebraic Stress Model
$EEDI$	Energy Efficiency Design Index
EFD	Experimental Fluid Dynamics
ESD	Energy Saving Device
GCI	Grid Convergence Index
IMO	International Maritime Organisation
$ITTC$	International Towing Tank Conference
JBC	JAPAN Bulk Carrier
KCS	KRISO Container Ship
LDV	Laser Doppler anemometry
LES	Large Eddy Simulation
LL	Lifting Line
LSR	Least Squares Root
$NACA$	National Advisory Committee for Aeronautics
$NMRI$	National Maritime Research Institute
$ONRT$	ONR Tumblehome Ship
OU	Osaka University
PIV	Particle image velocimetry

POW	Propeller Open Water
$RANS$	Reynolds Averaged Navier-Stokes
RE	Richardson Extrapolation
SFC	Skin Friction Correction
SRC	Ship Building Research Centre of Japan
SST	Menter shear stress transport
$TUHH$	Hamburg University of Technology
$V\&V$	Verification and Validation
WED	Wake Equalizing Duct

Greek Symbols

Symbol	Description
$\alpha, \alpha_{02}, \alpha_{11}, \alpha_{12}$	Constants
δ_{ij}	Kronecker's delta
$\delta_{RE}, \delta_{RE}^{02}, \delta_{RE}^{12}, \delta_{\Delta_M}$	Error Estimates
ϵ_{RE}	Discretization error in the Least Squares Root method
η_D	Propulsive efficiency
η_H	Hull efficiency
η_O	Propeller efficiency
η_R	Relative rotative efficiency
μ	Dynamic viscosity
∇	Gradient operator
ω	Vorticity
ϕ	General variable
ρ	Density
σ_{ij}	Total stress tensor

Roman Symbols

Symbol	Description
A_0	Propeller disc area

A_E	Expanded blade area
AP	Aft peak
B_{WL}	Maximum beam of waterline
C_B	Block coefficient
C_F	Frictional resistance coefficient
C_M	Midship section coefficient
C_P	Pressure coefficient
C_PV	Viscous pressure resistance coefficient
C_T	Total resistance coefficient
D	Depth
D_R	Propeller diameter
F_A	Forces applied to the background grid (as body force) in x-direction
F_P	Forces generated by propeller grid in x-direction
F_S	Factor of safety
FP	Fore peak
Fr	Froude number
$FR_{z\theta}$	Free to heave and pitch
FX_0	Propeller disc area
h_i	Step size (grid spacing) of the i-th grid; i=1,2,..n$_g$
J_{TM}	Advance ration from thrust identity
k	Turbulent kinetic energy
K_Q	Torque Coefficient
K_T	Thrust Coefficient
L_{PP}	Length between perpendiculars
L_{WL}	Length of waterline
LCB	Longitudinal Center of Bouyancy
LE	Leading edge
n	Revolution rate of the propeller

P	Instantaneous pressure
p	Order of accuracy in numerical method
P_D	Delivered power
P_E	Effective power
p_i	Time average pressure, $\bar{P}_i$
p'_i	Fluctuating pressure
P_R	Pitch ration
Q	Torque
r, r^{12}, r^{23}	Grid refinement ratio
R	Resistance in resistance test
Re	Reynolds number
S	Simulated solution
S_0	Extrapolated solution to the zero step size
S_E	Wetted surface area of ESD
S_i	Simulated solution of i-th grid; i=1,2,..n$_g$
S_W	Wetted surface area w/o ESD
S_{ij}	Strain-rate tensor
SS	Section
T	Draft
T	Thrust
t	Thrust deduction
U_D	Data uncertainty
U_G	Grid discretization uncertainty
U_I	Iterative uncertainty
U_i	Instantaneous velocity components in Cartesian directions
u_i	Time average velocity components in Cartesian directions, $\bar{U}_i$
u'_i	Fluctuating velocity components in Cartesian directions

$U_{SD}, U_{SD}^{02}, U_{SD}^{12}$	Standard deviations
U_{SN}	Numerical uncertainty
w_{TM}	Effective (mean) wake fraction
WL	Waterline
x_i	Cartesian coordinates

1
Introduction

1.1 General Background

Prediction of resistance is a vital problem for a naval architect at all stages of a new design because of the speed attained at a certain power consumption in a trial run, so called contract speed, is specified at the contract of a new ship order. In a condition that speed demand does not meet the specifications, the yard will have to pay a penalty to the owner depending on the difference between the contract speed and attained speed. If the speed gap is too large, owner might refuse the ship. Therefore designers are under pressure of being just in the limits. The dilemma for the designer and the yard as stated by Lars Larsson and Hoyte C. Raven (2010) is that too optimistic predictions might end up in a big burden for the yard while too conservative predictions will be a lost order. Fulfilling the contract speed with a reasonable margin is not only dependent on the resistance but also propulsive efficiency which includes propeller performance, mechanical losses in drive train and propeller-hull-appendage interaction.

Recently pressure on designers and yards is increasing considerably due to escalating environmental concerns. As a result, International Maritime Organisation (IMO) published a new mandatory concept named as Energy Efficiency Design Index (EEDI), in order to improve energy efficiency and eliminate inefficient ships from the market. IMO points out that in addition to the optimisation of the resistance, EEDI stimulates the new technical and operational developments. Technical developments than can be achieved by using unconventional propulsion arrangements together with the resistance optimisation. The main purpose of these arrangements is to provide a better flow at the stern where propeller operates and enhance propeller efficiency by using advanced configurations. Some of these arrangements described by Schneekluth & Bertram (1998) are overlapping propellers, contra-rotating propellers, controllable-pitch propellers, Kort nozzles, the Grim vane wheels, asymmetric aftbodies, Grothues spoilers and Wake Equalizing Duct (WED). However WEDs are the most commonly used Energy Saving Device (ESD) types according to (Schneekluth & Bertram, 1998).

There are three different ways to predict resistance and propulsive factors. Empirical methods are the simplest and fastest among them. Empirical formulas can be used only at the earliest design stage, when main dimensions and hull coefficients often vary, due to lack of accuracy. However at the very early design stage reasonable and fast approximations for a whole possible design variations are highly

valued. Another tool for predictions is model testing which is the most reliable and accurate method. Nevertheless it is very costly, time consuming and problematic when it comes to scaling from model scale to full scale, because model tests carried out at Froude similarity while Reynolds similarity cannot be fulfilled. Error caused by this phenomenon can be compensated for the conventional hulls and applications with the experience of testing facility and procedures recommended by International Towing Tank Conference (ITTC). Alternative to model tests and the last method of prediction is numerical simulations. As defined by Versteeg & Malalasekera (2007, p.1) "Computational Fluid Dynamics or CFD is the analysis of systems involving fluid flow, heat transfer and associated phenomena such as chemical reactions by means of computer-based simulation". One of the main fields of CFD is now ship hydrodynamics and it became a widely used tool for optimization. Lars Larsson and Hoyte C. Raven (2010) states that using potential flow methods for forebody optimisation is now widely used and recently afterbody optimisation using viscous flow methods has started to appear in design offices. As indicated by Kim et al. (2014) the main advantage of CFD comes from its ability to fulfill both Froude and Reynolds similarities meaning that model-scale results and full-scale results can be directly calculated while providing a great deal of detail about the flow. However the absolute accuracy of CFD is still under concern and final decisions about the predictions of resistance and propulsive factors are still made by model tests. After all, Lars Larsson and Hoyte C. Raven (2010, p.4-5) sums the situation between model tests and numerical simulations as "there is no question,however, that the regular testing of ship models will be replaced by numerical predictions,sooner or later".

The procedure of numerical simulation, also known as Computational Fluid Dynamics (CFD), as described by Lars Larsson and Hoyte C. Raven (2010) starts with building the conceptual model. At this stage physical phenomena behind the specified problem are identified. A conceptual mathematical model ,which consists of sets of differential or integral equations, is formed. In order to solve these equations numerically, they have to be discretized first and then solved by numerical methods. Iterative approach is used by most of the numerical methods. When convergence criterion is satisfied, iterative solver stops and the solution is supposed to be calculated. However, as shown in Figure 1.1 each step introduces errors to the solution. Modelling errors occur due to assumptions needed to construct the conceptual model and approximations in equations such as linearization or usage of empirical data. Numerical errors are discretization errors, convergence errors and roundoff errors which is introduced due to internal representation of numbers. Depending on the type of problem, numerical method can be based on potential/inviscid flow theory, viscous flow theory or even a combination of potential and viscous flow. Reynolds Averaged Navier-Stokes (RANS) is still the most common technique for predictions of resistance and propulsive factors. RANS solutions provide reasonable solution and there is still room for improvements however "the inherent problem of modelling the turbulence cannot be avoided. To overcome this difficulty, the much more computer-demanding methods of Large Eddy Simulation (LES) or Direct Numerical Simulation (DNS) type must be employed, and this will call for very substantial enhancements in computer power" (Lars Larsson and Hoyte C. Raven, 2010).

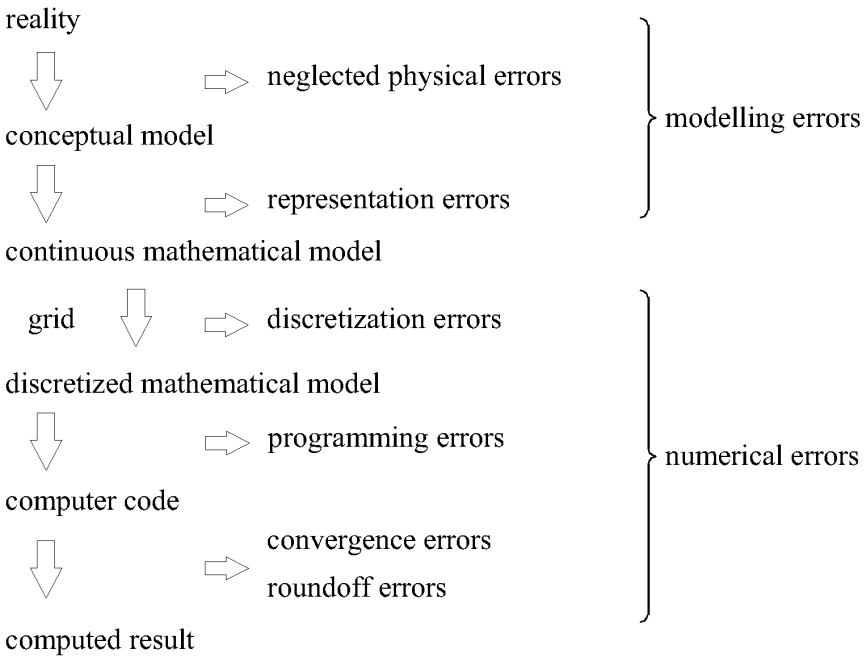

Figure 1.1: Sources of errors in computed results (Lars Larsson and Hoyte C. Raven, 2010)

Due to the errors described, there is no guarantee that computed results will match with the physical reality. Therefore a systematic approach should be used in order to determine the quality of method. Comparing the result of a computation with an experimental result can be thought of simple or straight forward way to do it. As Lars Larsson and Hoyte C. Raven (2010, p.109) stated, "however, if a comparison is favourable, that might be due to a fortuitous cancelling of modelling errors and numerical errors for the particular case considered". In another case these errors might add up rather than cancel each other. More thorough understanding of the effects of numerical errors and modelling errors on computed results can be achieved if they are considered separately.

Discretization errors are dependent on the numerical scheme and grid quality which is limited by the cell aspect ratio, smooth distribution of cell sizes, deviation from orthogonality, refinement in regions of high gradients, alignment of grid lines with flow directions, etc. When the step size of the grid is reduced substantially, discretization errors must die out in a flawless numerical method. "In other words, on refinement of the grid, the result should converge toward a grid-independent result" (Lars Larsson and Hoyte C. Raven, 2010, p.109). The effect of the numerical errors can be determined by checking the solutions of grids with different step-sizes. This method is called verification. After this step, validation of computed results against experimental data takes places. If the comparison of experimental data and grid-independent computation shows conflicting results, continuous mathematical model is to be blamed as a result of modelling errors.

As it is stated a V&V method is needed for determining the errors and uncertainties. Thus, there has been many studies for developing a standard V&V methodology such as:

> "Several constructive V&V methods based on Richardson Extrapolation (RE) have been put forward in the past decade. Roache (1998) introduced a Grid Convergence Index (GCI) with a safety factor for numerical uncertainty estimation; the ITTC (1999 and 2002) recomended an uncertainty assessment methodology based on the approach by Stern et al. (2001), in which the error and uncertainty are estimated with a correction factor taking the closeness to asymptotic range into consideration: Eça and Hoekstra (2002, 2006a, 2010a and 2010b) developed a methodon basis of RE and GCI, but with a Least Squares Root approach to take the numerical scatter into account."(Zou, 2012, p.4)

In order to extend the applications of V&V methods and highlight it's importance in CFD, workshops has been organised. However applications on ship hydrodynamics is still very limited. For the purpose of filling this gap and assessing the state of art in numerical hydrodynamics, the series of international Workshops on CFD in Ship Hydrodynamics was introduced(Larsson et al., 2014). Test cases, conditions and EFD data will be provided by the organisers and based on a questionnaire, participants will submit the results of computations together with the V&V results. As stated by (NMRI, 2015), 7^th of the series will be held in Japan in 2015 with 3 hulls; JAPAN Bulk Carrier (JBC), KRISO Container Ship (KCS) and ONR Tumblehome Ship (ONRT).

1.2 Motivation

The predictions of resistance and propulsion, which have always been biggest concern in ship design, has a crucial importance for designers and yards. Recently, efficiency gained a great deal of emphasis, therefore designers are forced to optimize the existing solutions and search for new designs (Kim et al., 2014). In order to achieve these tasks, the features of the flow must be well-understood and measured accurately in a way that designers can try many hulls and propulsion arrangements without spending too much time, effort and resources. Available literature and practice shows that neither empirical formulas nor towing tank test can provide these demands. On the other hand, numerical predictions promise a whole new era of design and optimisation by providing great deal of information on the flow with considerably fewer resources and time.

The objective of this Master's thesis is to predict resistance, propulsive factors and local flow around the stern region. The state of art CFD techniques will be used for computing the JAPAN Bulk Carrier (JBC) test case with and without ESD. In addition, a formal Verification and Validation (V&V) method is applied to control and understand the modelling and numerical errors in the computations. Propulsive power, which maybe the most important outcome of these tests, is investigated in order to yield the effects of the ESD.

1.3 Structure of the Thesis

The thesis contains 5 chapters in total. The current chapter presents a general background and the motivation for the origin of the problem and possible approaches to solve it. In the next chapter methods and theory of the motivated approach are described. Details of the applied CFD solver, verification and validation model; governing equations, boundary conditions, grids and numerical methods of both potential flow and viscous flow will be mentioned in the second chapter. At the third chapter the hull and appendages of JAPAN Bulk Carrier (JBC) and the conditions of resistance, POW, self propulsion and local flow measurement tests are presented. All results of the test cases and investigations on POW and self propulsion settings in SHIPLOW code are covered in the fourth chapter by giving the details of computational domains and boundary conditions, grid dependence studies and V&V results. Since the same grid and conditions are used for calculation of local flow and turbulence; grid dependence study is skipped in this section. Finally, the last chapter offers a conclusion and summary of whole thesis.

2
Methods & Theory

2.1 Governing Equations

Equations governing the flow around a ship will be presented in this section. A global Cartesian coordinate system x, y, z is defined at a fixed position on the ship. Entire flow field is assumed to be incompressible and steady in a time-averaged sense. Conservation of mass and momentum or in other words continuity equation (2.1) and Navier-Stokes equations (2.2) respectively in Einstein notation read (Broberg et al., 2007):

$$\frac{1}{\rho}\frac{\partial \rho}{\partial t} + \frac{\partial U_i}{\partial x_i} = 0 \tag{2.1}$$

$$\rho\frac{\partial U_i}{\partial t} + \rho\frac{\partial U_j U_i}{\partial x_j} = \rho F_i + \frac{\partial \sigma_{ij}}{\partial x_j} \tag{2.2}$$

where U_i denotes instantaneous velocity components, t is time, ρ represents density, F_i is body force components. σ_{ij} is total stress and is described for the Newtonian fluids as:

$$\sigma_{ij} = -P\delta_{ij} + 2\mu(S_{ij} - \frac{1}{3}S_{kk}\delta_{ij}) \tag{2.3}$$

where μ represents the dynamic viscosity and S_{ij} is the strain-rate tensor and can be written

$$S_{ij} = \frac{1}{2}(\frac{\partial U_i}{\partial x_j} + \frac{\partial U_j}{\partial x_i}) \tag{2.4}$$

Note that S_{kk} the Eq.2.3 is zero for incompressible flows because of the continuity equation (2.1).

2.1.1 Inviscid Flow

Having introduced the equations needed for describing the flow around a ship such as continuity and Navier-Stokes equations (2.1), (2.2), in some cases viscosity related terms can be dropped. This equations are called as *Euler equations* and describe the inviscid flow (Lars Larsson and Hoyte C. Raven, 2010). Euler equation can be written as

$$\rho\frac{\partial U_i}{\partial t} = -\frac{\partial P}{\partial x_i} + \rho F_i \tag{2.5}$$

Another simplification is that the inviscid flow is *irrotational* meaning that the curl of the velocity vector or the vorticity is zero.

$$\omega = \nabla \times \mathbf{u} = 0 \tag{2.6}$$

Velocity terms being expressed as the gradient of velocity potential $\phi(x, y, z)$, such that

$$\mathbf{u}(x, y, z) = \nabla\phi \tag{2.7}$$

Substitution of Eq.2.7 into the continuity equation 2.1 in steady flow will yield *Laplace equation*

$$\nabla^2\phi = 0 \tag{2.8}$$

Last equation for inviscid flow is derived from the Euler equations called *Bernoulli equations*

$$\frac{\partial\phi}{\partial t} + \frac{U^2}{2} + \frac{P}{\rho} + \hat{\phi} = C(t) \tag{2.9}$$

where $\hat{\phi}$ is usually the gravity force (per unit mass) times the height. For steady flows $\frac{\partial\phi}{\partial t}$ term is dropped and the constant term on RHS of the equation becomes time independent.

2.2 Turbulent Flow Simulation : RANS Method

There are different types of methods to compute the turbulent flow depending on the approximation or modelling the turbulence. Direct Numerical Simulation (DNS) method is based on the instantaneous continuity and Navier–Stokes equations (2.1), (2.2) and "developes a transient solution on a sufficiently fine spatial mesh with sufficiently small time steps to resolve even the smallest turbulent eddies and the fastest fluctuations." (Versteeg & Malalasekera, 2007). According to Zou (2012) this conditions for ship hydrodynamics however are extremely expensive in terms of computational power since full scale ships are mostly order of 100 m on the other hand smallest scale eddies are down to 0.1 mm. Large Eddy Simulation (LES) resolves the the large scale turbulent motions in order to model the small scale eddies using sub-grid scale models. Reynolds Averaged Navier-Stokes (RANS) method solves the mean flow by time-averaging the Navier-Stokes equation and models the turbulence. Due to the limited computational resources, Zou (2012) indicates that RANS method is the most widely used CFD technique in practice.

The Reynolds-averaged Navier Stokes equations are obtained by splitting the instant velocity, pressure and stress tensor into two parts; a mean value in time and a fluctuating value in time

$$U_i = \bar{U_i} + u_i' \equiv u_i + u_i' \ , \ P_i = \bar{P_i} + p_i' \equiv p_i + p_i' \ , \ \sigma_i = \bar{\sigma_i} + \sigma_i' \tag{2.10}$$

For incompressible flow, time-averaged continuity equation (2.11) and Navier-Stokes equations (2.12) can be written (Broberg et al., 2007)

$$\frac{\partial u_i}{\partial x_i} = 0 \tag{2.11}$$

$$\frac{\partial u_i}{\partial t} + \frac{\partial(u_j u_i + \overline{u_j' u_i'})}{\partial x_j} = \bar{F}_i - \frac{1\partial p}{\rho \partial x_i} + \frac{\partial}{\partial x_j}\left(\nu(\frac{\partial u_i}{\partial x_j} + \frac{\partial u_j}{\partial x_i})\right) \tag{2.12}$$

where

$$\nu = \frac{\mu}{\rho} \tag{2.13}$$

2.3 Turbulence Modelling

As can be seen in left hand side of the time averaged Navier-Stokes equation (2.12), convective term has a new tensor unknowns, $-\rho\overline{u_j' u_i'}$, called Reynolds stress. In total six additional unknowns are added since $-\rho\overline{u_j' u_i'}$ is a symmetric tensor. Therefore, in order to solve this closure problem, more equations are needed.

There are some approaches for solving the closure problem, such as eddy viscosity models, based on the Boussinesq assumption; Algebraic Stress and Reynolds stress models, based on dynamic equations directly for the six unknowns introduced by Reynolds stress tensor (Zou, 2012). Eddy viscosity models requires much less computational resources than Algebraic Stress and Reynolds stress models because Boussinesq assumption consider the relation between Reynolds stress tensor and strain-rate tensor linearly.

2.3.1 Explicit Algebraic Stress Model

Linear eddy viscosity models sometimes fails to give provide satisfying results due to the linear approximation done by Boussinesq assumption. Therefore nonlinear terms should be taken into account. Explicit Algebraic Stress Model (EASM) computes the components of the Reynolds stress using algebraic equations with nonlinear terms in mean strain-rate and rotation-rate(Broberg et al., 2007).

2.4 Numerical Methods in SHIPFLOW

2.4.1 CFD Solver: SHIPFLOW

The CFD code implemented in this thesis is SHIPFLOW which has been developed by FLOWTECH International AB with close cooperation of Shipping and Marine Technology Department at Chalmers University of Technology and SSPA. The code is specially optimised for ship hydrodynamics and all outputs of resistance and propulsion are presented in the naval architects way.

SHIPFLOW has six modules (Broberg et al., 2014) : XMESH, XPAN, XBOUND, XGRID, XCHAP and XPOST. XMESH and XPAN are potential flow modules:

panel generator and potential flow solver respectively. Panelization of the body and free-surface is done by XMESH before the computation is executed and during the computation panelization is updated due to sinkage & trim conditions which are updated in each iteration. Potential flow around three dimensional bodies is solved by XPAN based on a surface singularity panel method. XBOUND module is for thin turbulent boundary layer computations, however it is also capable of computing the streamlines traced from a potential flow computation, laminar boundary layer and the transition to the turbulent later for simpler cases. For the viscous flow computations (RANS), XGRID and XCHAP modules are used. XGRID generates the grid (without appendages) while taking into account the sinkage & trim and it is capable of generating grids for mono hulls, twin skeg hulls and submerged bodies. XCHAP solver can handle complicated geometries with overlapping grids with parametrized models of appendages that are available in the system. Importing the grid from an exernal grid generator is also possible. The solver can be used in a global approach or a zonal approach and flow can be computed with a double model or with a prescribed free surface computed by XPAN module.

2.4.2 Numerical Methods in XCHAP

XCHAP solves the Reynolds Averaged Navier-Stokes equations with a finite volume code. $EASM$, $k-\omega$ SST turbulence models are available (Broberg et al., 2007). The convective terms are discretized with a Roe scheme which is only first order accurate. Therefore in order to increase the accuracy a flux correction is applied explicitly. Two different second order schemes are applied. A MinMod limiter selects which scheme will be applied. The diffusion terms are discretized with central differences and a finite difference way with central differences. Alternating Direction Implicit (ADI) is used for solving the equations. The tri-diagonal systems are solved for the first order convective terms and the second order diffusion terms. A local artificial time-step is calculated for each ADI sweep based on CFL and von Neumann numbers in all directions except the implicit one (Broberg et al., 2007).

2.4.3 Boundary Conditions

In order to solve the partial differential equations, boundary conditions are defined in the computational domain. Two layers of ghost cells are used in XCHAP (Broberg et al., 2007). Two boundary conditions are used; Dirichlet and Neumann conditions. Boundary types employed in XCHAP are noslip, slip, inflow, outflow and interior. Inlet condition sets a fixed uniform velocity inlet, estimated turbulent quantities and a zero pressure gradient normal to the inlet boundary. Outflow condition only consists of Neumann boundary condition that sets the gradient of velocity, k and pressure to zero, normal to the outflow plane. Slip condition simulates a symmetry condition by setting the normal velocity and normal gradient of other variables to zero. Noslip condition specifies the velocities components, k and normal pressure component as zero at the wall. Since there are no wall-functions are used in XCHAP, cell density near the hull and appendages should be fine enough. Therefore y^+ values are to be kept smaller than one.

2.4.4 Grid

Finite volume method requires grid cells in order to discretize the partial differential equations and approximate algebraic equations. In XCHAP module only structured grids are used. A simple geometry such as bare hull can be represented by a single-block structured grid while more complex geometries such as hull with appendixes can be expressed by the multi-block structured grid and overlapping grid.

Three grid topologies used in XCHAP are H-H, H-O and O-O types. Figure 2.1 presents examples of grids with very coarse grid densities for clarity. Although it is possible to import grids from externally generated structured grids, all grids in this thesis work is created by in-house modules; XGRID and XCHAP.

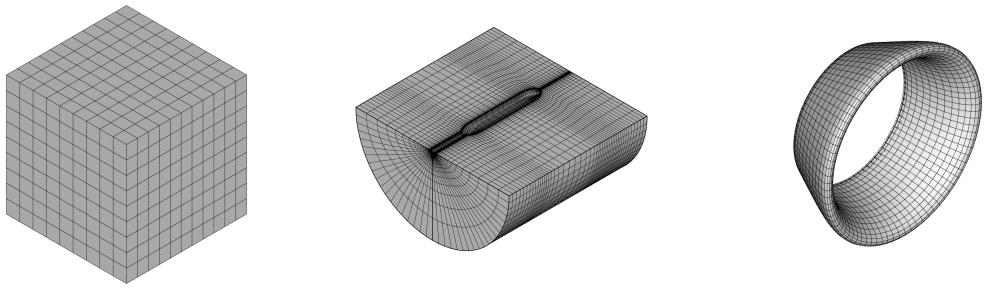

(a) H-H grid topology **(b)** H-O grid topology **(c)** O-O grid topology

Figure 2.1: Examples of grid topologies

2.4.4.1 Overlapping Grids

Overlapping grids were introduced to XCHAP in order to compute the flow around more complicated geometries (rudders, shafts, brackets, or fins) than a single block of structured grids (Regnström, 2008). Overlapping grid technique is powerful because it mostly offers the generality of unstructured grids while most of the advantages of structured grids is retained. One more advantage of overlapping grids is that they are not depending on the use of structured component grids even though all component grids are structured in SHIPFLOW. It is very useful in ship hydrodynamics because it allows to create a library of ready made grids for standard shapes such as rudders, struts , fins, possibly parametrized so that they can be customized (Regnström, 2008).

Another important application of overlapping grids is the refinements on the single block of structured grids. Often stern region of the ship is expected to have denser grids than other regions. In order to refine the grid only at the desired region such as stern, overlapping grids works with high accuracy and cost effective. Overlapping grids are widely used in this thesis work for generating the Energy Saving Device (ESD) and the refinements at the stern region.

2.4.5 Propeller Simulation

An operating propeller will affect the flow by creating a sudden pressure jump across the propeller plane. Due to the pressure difference, the flow ahead of the propeller will be accelerated in both the axial and tangential directions. In SHIPFLOW code, XCHAP module simulates the effect of the propeller with the body force approach induced in a cylindrical component in overlapping grid (Broberg & Orych, 2012). The body forces are calculated with a built in Lifting Line (LL) propeller analysis program, then added to the momentum equations at the grid elements where the propeller is located. The flow passes through the cylindrical propeller grid, linear and angular momentum of the flow increase as if it passed a propeller of infinite number of blades (Zhang, 1990). The forces induced by body forces vary in space but are independent of time.

2.5 Verification and Validation

As mentioned in Section 1.1, the real problem is not directly solved. Since numerical modelling and computation brings errors and uncertainties as seen at Figure 1.1, the degree of accuracy must be under concern. It is a well known fact from the literature that assessing accuracy just by comparing the EFD results and CFD results is not sufficient. However formal V&V methods has the capacity of determining the numerical errors and modelling errors. Least Squares Root approach is used for verification in order to address topics such as numerical uncertainty or achieved order of accuracy. Richardson Extrapolation (RE) and Grid Convergence Index (GCI) concepts will be introduced since LSR method is based on them.

2.5.1 Verification Method

Estimation of numerical uncertainty in a numerical computation is called verification. It consists of solution verification and code verification. Latter can be ignored since it is assumed that the code has been developed correctly(Zou, 2012). Therefore main focus will be on the solution verification.

Governing equations of ship hydrodynamics have non-linear nature that can be solved through iterative methods. This approach brings an inevitable error when the flow is complex such as flow around the ship. Another source of error is discretization, assuming that round-off error is negligible. Therefore numerical uncertainty becomes:

$$U_{SN} = \sqrt{U_I^2 + U_G^2} \tag{2.14}$$

where U_G is the discretization uncertainty and U_I is the iterative uncertainty due to lack of convergence. If discretization uncertainty is much bigger than iterative uncertainty, then U_I can be ignored in the eq. (2.14).

The classical method of determining the discretization uncertainty is Grid Convergence Index (GCI). Grid convergence with a series of systematically similar grids

is done by Richardson Extrapolation (RE). In a numerical solution, discretization error δ_{RE} can be expressed as

$$\delta_{RE} = S_i - S_0 = \alpha h_i^p + H.O.T \tag{2.15}$$

where $H.O.T$ stands for higher order terms, S_i is the solution from computation on the i-th grid (i=1,2...n_g) ; S_0 is the extrapolated solution to the zero step size ; h_i is the step size of the i-th grid , α is a constant and p is the order of accuracy. If the grid i is fine enough, $H.O.T$ terms can be neglected and solution is considered in "asymptotic range". Zou (2012) states that "this is classical Richardson Extrapolation (Roache,1998)"

$$\delta_{RE} = S_i - S_0 = \alpha h_i^p \tag{2.16}$$

In Grid Convergence Index (GCI) method, the absolute value of the RE error (2.18) and a factor of safety F_S (empirical value) are used for evaluating the uncertainty :

$$U_G = F_S|\delta_{RE}| \tag{2.17}$$

where F_S =3 for two grids and F_S =1.25 for at least three grids.

2.5.1.1 LSR method

This method considers the scatter of numerical solutions (more than three grid densities), since in ship hydrodynamics applications variation of grid cannot be exactly systematic (Zou & Larsson, 2014). However effect of the scatter is thought to be reduced by using Least Squares Root (LSR) method. As stated before, the discretization error in LSR method is based on general RE :

$$\epsilon_{RE} \approx \delta_{RE} = S_i - S_0 = \alpha h_i^p \tag{2.18}$$

where ϵ_{RE} refers to discretization error in LSR method ; n_g is available number of grids ($n_g > 3$).
In order to determine the unknowns (S_0, α, p), the curve fit of LSR approach is used for minizing the function :

$$f(S_0, \alpha, p) = \sqrt{\sum_{i=1}^{n_g} (S_i - (S_0 + \alpha h_i^p))^2} \tag{2.19}$$

Convergence condition is determined as below:

1. Monotonic divergence : $p < 0$
2. Monotonic convergence : $p > 0$
3. Oscillatory convergence : $n_{ch} \geqslant \mathrm{INT}(n_g/3)$, where $n_c h$ is the number of triplets with $(S_{i+1} - S_i)(S_i - S_{i-1})$
4. Otherwise, anomalous

Estimation of error is not only based on general RE form, but also three alternative methods due to fact that order of accuracy depends on the scatter.

$$\delta_{RE}^{02} = S_i - S_0 = \alpha_{02} h^2 \tag{2.20}$$

$$\delta_{RE}^{12} = S_i - S_0 = \alpha_{11} h + \alpha_{12} h^2 \tag{2.21}$$

$$\delta_{\Delta_M} = \frac{\Delta_M}{(h_{n_g}/h_1) - 1} \tag{2.22}$$

where Δ_M is the data range, $\Delta_M = max(|S_i - S_j|)$ $1 \leqslant i, j \leqslant n_g$ and h_{ng} represents the step size n_gth grid.

LSR method is also based on GCI but with different way of determining safety factor and error estimation. As explained at derivation of Equation 2.17, it is assumed that iterative uncertainty is negligible; then numerical uncertainty is formulated as :

1. Monotonic convergence:
   (a) $0.95 \leqslant p \leqslant 2.05$: $U_{SN} = 1.25\delta_{RE} + U_{SD}$
   (b) $p \leqslant 0.95$: U_{SN} =min($1.25\delta_{RE} + U_{SD}, 3\delta_{RE}^{12} + U_{SD}^{12}$)
   (c) $p \geqslant 2.05$: U_{SN} =max($1.25\delta_{RE} + U_{SD}, 3\delta_{RE}^{12} + U_{SD}^{02}$)
2. Oscillatory convergence: U_{SN} =$3\epsilon_{\Delta_M}$
3. Anomalous behavior: U_{SN} =min($3\epsilon_{\Delta_M}$,$3\delta_{RE}^{12} + U_{SD}^{12}$)

where $U_{SD}, U_{SD}^{02}, U_{SD}^{12}$ are standard deviations of the curve fit for equations (2.18), (2.20), (2.21).

2.5.1.2 Validation Procedure

Validation process is a tool for assessing the errors or uncertainties of a numerical computation in a more fundamental way. A simplified version of the validation procedure of ASME V&V 20-2009 is adopted (Zou & Larsson, 2014). In the simplified procedure, two parameters, validation comparison error and validation uncertainty are introduced. Comparison error is defined as:

$$E = S - D \tag{2.23}$$

where S is the simulated solution and D is experimental data. The validation uncertainty is defined as :

$$U_{val}^2 = U_{SN}^2 + U_{input}^2 + U_D^2 \tag{2.24}$$

where U_{SN} is the data uncertainty , U_{input} is the input parameter uncertainty an U_D represents the data uncertainty in experiment. According to Zou & Larsson (2014), for a strong model concept, U_{input} can be ignored (U_{input} =0) and U_{val} becomes:

$$U_{val}^2 = U_{SN}^2 + U_D^2 \tag{2.25}$$

When two uncertainties, validation comparison error and validation uncertainty are determined, validation result can be approximated as :

- if $|E| >> U_{val}$, the magnitude and sign of E might be used to improve the modelling
- if $|E| \leq U_{val}$, the modelling error is located in the noise level of U_{val}. (Zou & Larsson, 2014)

3

Geometry and Conditions

JAPAN Bulk Carrier (JBC) is a Cape size bulk carrier designed by National Maritime Research Institute (NMRI), Yokohoma University, Ship Building Research Centre of Japan (SRC) and with the support of ClassNK as part of the ClassNK joint R&D for Industry Program. Ship is equipped with a Wake Equalizing Duct as an Energy Saving Device (ESD). Resistance tests, self-propulsion tests and PIV measurements of stern flow fields will be carried out by NMRI, SRC and OU. Also laser Doppler anemometry (LDV) measurements of stern flow fields will be provided by TUHH wind tunnel (NMRI, 2015). JBC is the new test case of the workshop Tokyo 2015 a Workshop on CFD in Ship Hydrodynamics (NMRI, 2015).In this thesis work, results of computations and investigations will be presented for resistance, propulsion, mean flow and turbulence quantities predictions.

3.1 Hull

Hull lines and profile view as can be seen at Figure 3.1 of JAPAN Bulk Carrier (JBC) is prepared from the provided iges drawings from NMRI (2015). Table 3.1 shows the main particulars of JBC in full scale, and also the information regarding to position and rotation direction of propeller.

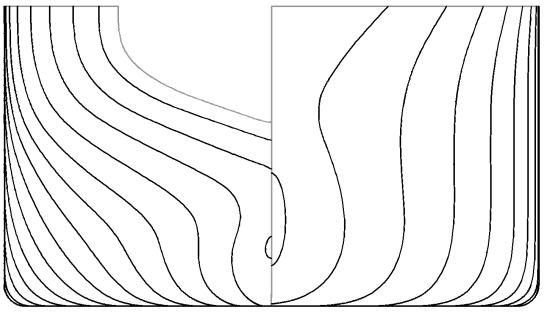

(a) Sections of JBC with spacing of $\frac{L_{PP}}{40}$ metre

(b) Profile view of bare hull of JBC (NMRI, 2015)

Figure 3.1: JBC geometry

Table 3.1: Main Particulars (NMRI, 2015)

Main particulars		Full scale	Units
Length between perpendiculars	L_{PP}	280.0	m
Length of waterline	L_{WL}	285.0	m
Maximum beam of waterline	B_{WL}	45.0	m
Depth	D	25.0	m
Draft	T	16.5	m
Displacement volume	∇	178369.9	m^3
Wetted surface area w/o ESD	S_W	19556.1	m^2
Wetted surface area of ESD	S_E	745.2	m^2
Block coefficient	C_B	0.8580	
Midship section coefficient	C_M	0.9981	
LCB ($\%L_{PP}$), fwd+	LCB	2.5475	
Propeller center, long. location (from FP)	x/L_{PP}	0.985714	
Propeller center, vert. location (below WL)	$-z/L_{PP}$	-0.040414	
Propeller rotation direction (view from stern)		clockwise	

3.2 Appendages

Appendages are obtained from (NMRI, 2015) in igs file format. In order to introduce the appendages, a cross section at center line is shown in Figure 3.2.

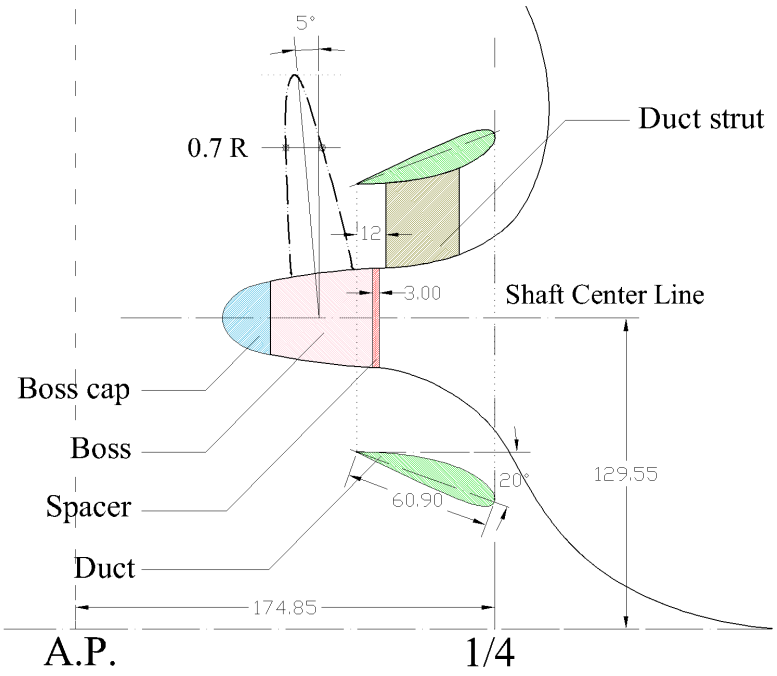

Figure 3.2: Appendages of JBC

Energy Saving Device (ESD) consists of duct and duct strut. Therefore spacer, boss and boss cap is always mounted to the hull. Figure 3.3 and Figure 3.4 show the bare hull and hull with Energy Saving Device conditions where spacer and boss is coloured as white, boss cap is dark grey, duct strut brown, duct is green and hull is light blue.

(a) Bare Hull **(b)** Hull with ESD

Figure 3.3: Perspective view of JBC appendage arrangement for resistance

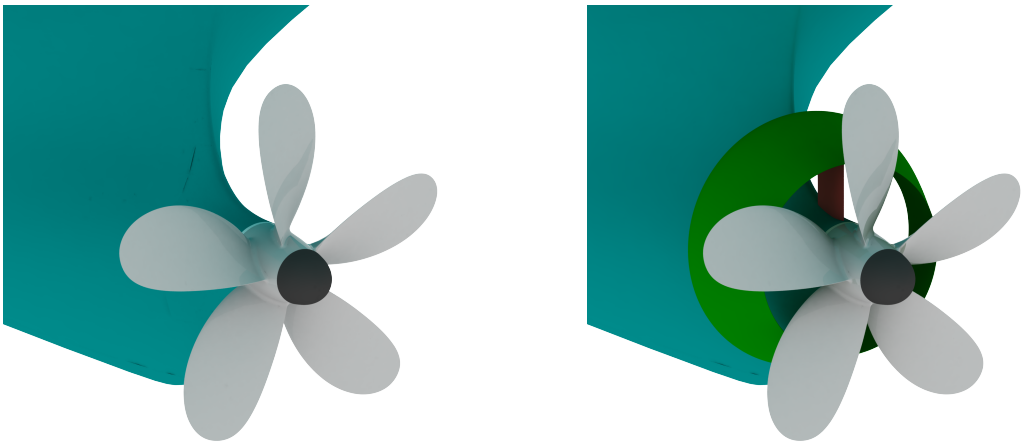

(a) Hull without ESD with propeller **(b)** Hull with ESD and propeller

Figure 3.4: Perspective view of JBC appendage arrangement for self propulsion

As shown in Figure 3.5 Foil section of the duct is NACA4420 with and opening/-contraction angle of 20 degrees. Diameter of the duct outlet is $0.55D_R$ and chord length of the foil is $0.30D_R$. Foil section of duct strut can be seen at Figure 3.6.

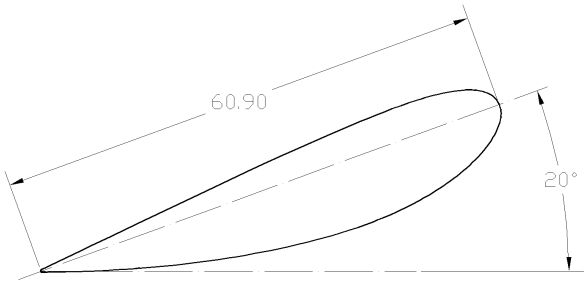

Figure 3.5: Foil section of the duct, NACA4420

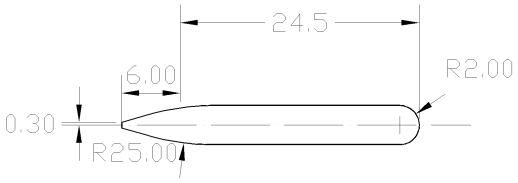

Figure 3.6: Foil section of the duct strut

3.3 Propeller

Propeller data is obtained from (NMRI, 2015) as an igs file together with offset data of propeller. Table 3.2 contains the details while Figure 3.4, Figure 3.7 shows the propeller at the stern.

Table 3.2: Propeller Data for JBC

Propeller No.	MP. 687
Type	Fixed Pitch
No. of propeller	1
No. of blades	5
Diameter, D_R (m)	0.203
Boss ratio	0.18
Pitch Ratio P_R/D_R	0.75
Pitch (constant) (m)	0.15225
Expanded Area Ratio A_E/A_0	0.50
Rotation	clockwise
Max. blade width ratio	0.2262
Blade thickness ratio	0.050

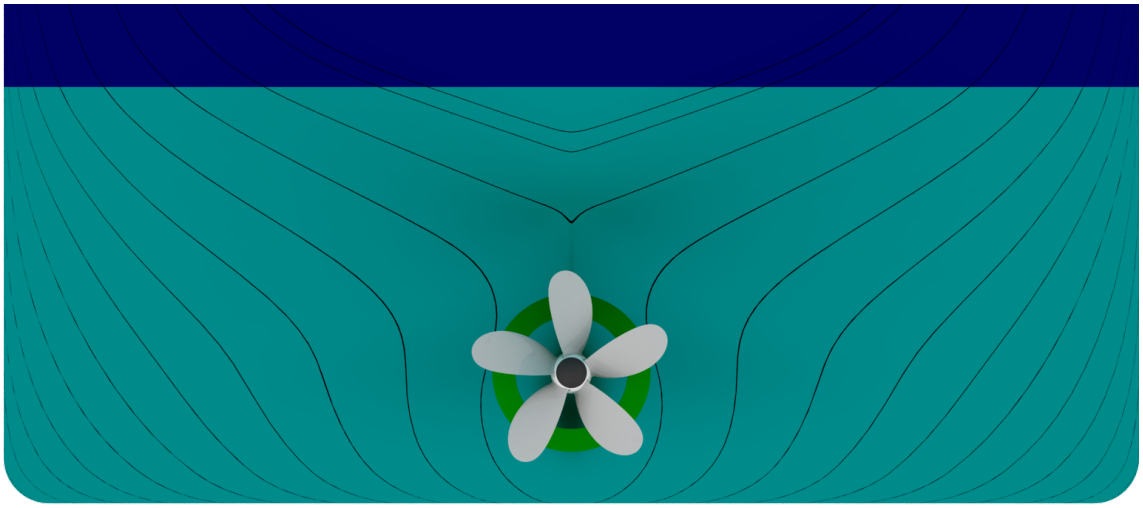

Figure 3.7: Stern view of JBC with ESD and propeller

3.4 Conditions

Conditions of simulations are determined by the workshop organising committee (NMRI, 2015). All participants will have to fulfill these conditions for each case. For the validation of results, each case is linked to the EFD data provider. All EFD test are conducted without a rudder, therefore same conditions must be satisfied at the CFD simulations. Conditions for resistance tests are shown at Table 3.3 where case notations were adopted from the workshop (NMRI, 2015). Requested parameters for Case 1.1a(NMRI) and Case 1.2a(NMRI) are C_T, C_F, C_P , sinkage and trim together with Verification and Validation (V&V) parameters.

Table 3.3: Conditions of Resistance sinkage & trim tests

Case #	1.1a	1.2a
Wave	Calm	Calm
Condition	Towing	Towing
L_{PP} (m)	7	7
Fr	0.142	0.142
Re	7.46×10^6	7.46×10^6
ESD	without	with
Propeller	without	without
Attitude	$FR_{z\theta}$	$FR_{z\theta}$
Validation Variables	Resistance, sink & trim	Resistance, sink & trim
EFD provider	NMRI	NMRI

Conditions for mean flow and turbulence tests are shown at Table 3.4. Requested figures for Case 1.3a(NMRI) and Case 1.4a(NMRI) will be proveded for u, v, w and k at certain cross sections as can be seen in Table 3.5.

Table 3.4: Conditions of mean velocity and turbulence tests

Case #	1.3a	1.4a
Wave	Calm	Calm
Condition	Towing	Towing
L_{PP}	7	7
U (m/s)	1.179	1.179
Fr	0	0
Re	7.46×10^6	7.46×10^6
ESD	without	with
Propeller	without	without
Attitude	$FR_{z\theta}$, FX_0	$FR_{z\theta}$, FX_0
Validation Variables	Mean velocity, turbulence	Mean velocity, turbulence
EFD provider	NMRI	NMRI

Table 3.5: Longitudional positions of cross sections for measurements

cross sections at x/Lpp	description of cross section
1	AP (7)
0.98428	gap between propeller and duct (4)
0.96250	SS 3/8 (2)

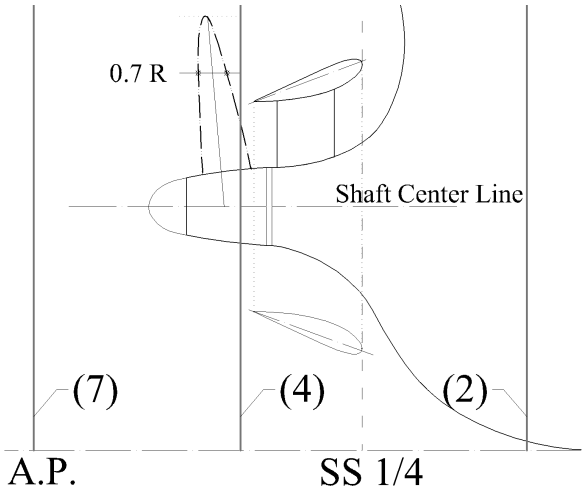

Figure 3.8: Measurement Planes (2),(4) and (7) at the stern of JBC

Conditions for self propulsion tests are shown at Table 3.6. Requested parameters for Case 1.5a(NMRI) and Case 1.6a(NMRI) are C_T, K_T, K_Q and n with Verification and Validation (V&V) parameters. Note that self propulsion tests are carried out at the ship point meaning that an additional towing force which is named as Skin Friction Correction (SFC) applied (NMRI, 2015).

Table 3.6: Conditions of self propulsion tests

Case #	1.5a	1.6a
Wave	Calm	Calm
Condition	Self Propelled (ship point)	Self Propelled (ship point)
SFC (N)	18.2	18.1
L_{PP} (m)	7	7
Fr	0.142	0.142
Re	7.46×10^6	7.46×10^6
ESD	without	with
Propeller	with	with
Attitude	$FR_{z\theta}$	$FR_{z\theta}$
Validation Variables	thrust, torque, propulsive factors	thrust, torque, propulsive factors
EFD provider	NMRI	NMRI

All experiments are carried out with $\rho = 998.2\ [kg/m^3]$, $\nu = 1.107 \times 10^6\ [m^2/s]$ and $g = 9.80\ [m/s^2]$. Non-dimensional coefficients for bare hull in resistance and hull without ESD in self propulsion simulations are based on the wetted surface $S_O/L_{PP} = 0.2494$ while non-dimensional coefficients in hull with ESD cases are based on $S_O/L_{PP} = 0.2504$ (NMRI, 2015).

4
Results and Discussion

Series of systematic investigations on resistance, sinkage & trim, propulsive factors, local flow and turbulence quantities will be presented in the following sections. All computations are performed with SHIPFLOW code and conducted on Beda cluster of Chalmers Center for Computational Science and Engineering (C3SE).

4.1 Resistance, Sinkage & Trim

The numerical predictions of two test cases (Case 1.1a(NMRI) and Case 1.2a(NMRI)) of 2015 Tokyo Workshop on CFD in Ship Hydrodynamics (NMRI, 2015) is presented together with Verification and Validation results. Conditions for the test cases are described in Section 3.4, Table 3.3. Appendages for the Case 1.1a(NMRI) and Case 1.2a(NMRI) are shown in Figure 3.3. Theory of the potential flow computations is described in Chapter 2.

4.1.1 Computational Domain and Boundary Conditions

Coordinate system is defined as right-hand side Cartesian system and body fixed as shown in Figure 4.1a. According to offset file format of SHIPFLOW, origin is the intersection of the flat free surface, the fore perpendicular (FP) and the ship centre-plane (Broberg et al., 2014). Axis of the coordinate system x,y,z points at the stern , starboard and upwards, respectively. Since the flow is symmetric for both viscous flow and potential flow, half of the hull is used for computations as shown in Figure 4.1.

Panelling is conducted with XMESH module. In order to have a greater control over panelling; hull is divided into four panelling groups such as bulb, main, aft and boss while the panels of the free surface are divided into three groups. As an option of XMESH module, panelling of each group can be determined seperately and connections between panel groups can be smoothened by using streching functions. Figure 4.1 presents an example of coarse panelling of the hull and the free surface. Wave pattern, wave making resistance coefficient (C_W), sinkage and trim is calculated with the XPAN module out of 20091 panels in total.

The viscous flow computations are carried out with the computational domain that consists of six boundaries is shown in Figure 4.1a. The distance between inlet and fore-perpendicular (FP) is $0.5L_{PP}$. Outlet plane however located at $0.8L_{PP}$ behind the aft-perpendicular in order to prevent the wake to reach the outflow. Radius of

the cylindrical outer boundary is $3L_{PP}$ in order to eliminate the blockage effect as much as possible.

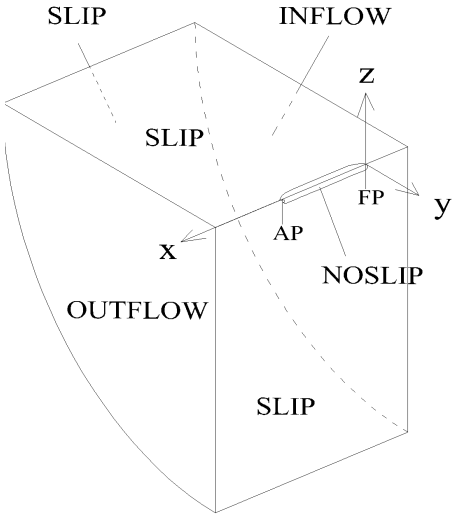

(a) Computational domain and boundary conditions for viscous flow

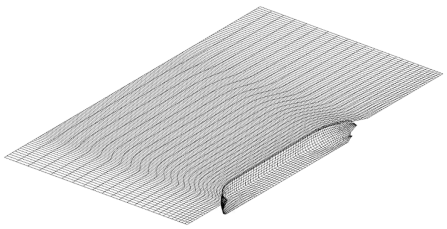

(b) Computational domain and panel distribution for potential flow

Figure 4.1: Computational domain,boundary conditions and panel distribution

Grids of viscous flow computations are generated by the XGRID module and XCHAP module. After the body fitted grids are developed for the hull, a refinement is applied at the stern region for the bare hull and the hull with ESD cases. For the Case 1.2a (hull with ESD), duct and duct strut grids are generated. Overlap of all grids is calculated by the XCHAP module. In order to apply Least Squares Root (LSR) for verification, five systematically varied grids (overlapping grids) are generated for each test case. The grid distribution of the coarsest body-fitted and structured grid among the systematically similar grids is shown in Figure 4.1a. No wall functions are used,therefore y^+ values are determined and varied with uniformly refined grids. Explicit Algebraic Stress Model (EASM) is applied for all viscous flow computations.

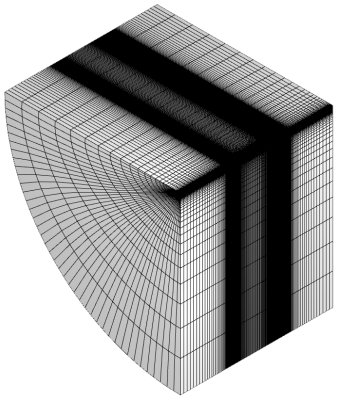

Figure 4.2: Grid distribution of the coarsest grid

4.1.2 Wave Resistance, Sinkage & Trim

4.1.2.1 Potential Flow Predictions

After panelling the hull and free surface; for the conditions shown in Table 3.3, potential flow is computed for the non-linear free surface boundary condition at $Fr = 0.142$ using XPAN. Non-dimensional hull data calculated out of panelling is shown in Table 4.1. A comparison between the main particulars of the actual ship shown in Table 3.1 and modelled hull shows that agreement is satisfactory.

Table 4.1: Hull data for potential flow computations

Main particulars		Model	Units
Length between perpendiculars	L_{PP}	1	m
Maximum beam of waterline	B_{WL}	0.1607	m
Draft	T	0.0604	m
Displacement volume	∇	0.82x10^{-2}	m^3
Wetted surface area w/o ESD	S_W	0.2547	m^2
Block coefficient	C_B	0.8486	-
LCB (%L_{PP}), fwd+	LCB	2.6783	-

Due to non-linear terms, an iterative process is applied and solution is converged after four iterations. Wave making resistance, sinkage and trim predictions are presented at Table 4.1. Note that panelling is done for the bare hull and the free surface only. ESD was not included to the panelling, therefore only one case was computed. However the effect of the ESD is thought to be small since it is far away from free surface. The reason of small difference in wave resistance coefficients between bare hull and hull with ESD is due to the difference in the wetted surface areas.

Table 4.2: Results of potential flow computation

Sinkage & trim calculation	Results
Wave resistance coefficient, C_W for bare hull	0.1528 x10^{-3}
Wave resistance coefficient, C_W for hull with ESD	0.1522 x10^{-3}
Center of flotation, (%L_{PP}), fwd+	-0.84
Draft change at center of flotation,(%L_{PP})	-0.0847
Draft change at $L_{PP}/2$, (%L_{PP})	-0.0859
Draft change at bow, (%L_{PP})	-0.158
Draft change at stern, (%L_{PP})	-0.0137
Trim (positive : bow up), (%L_{PP})	-0.144
Trim angle (degree)	-0.0827

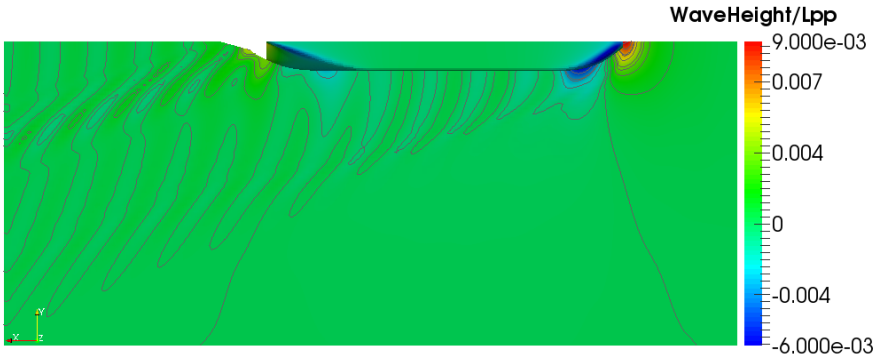

Figure 4.3: Wave pattern

Figure 4.3 shows the calculated wave pattern. Since the Froude number is very low (Fr=0.142), the wave amplitudes are small but there are four wave systems: diverging waves generated at the bow, fore and aft shoulders and transverse waves generated at the stern. A supplement to the wave pattern contour plot, Figure 4.4a shows the wave height along the hull. As expected and shown in Figure 4.4b; at the bow and the stern, high pressure due to stagnation points result in a wave crest. On the other hand, shoulders of the ship create low pressure which bring out a wave trough. Note that origin of the coordinate system is the intersection of the flat free surface, the fore perpendicular (FP) and the ship centre-plane; x axis points to the stern.

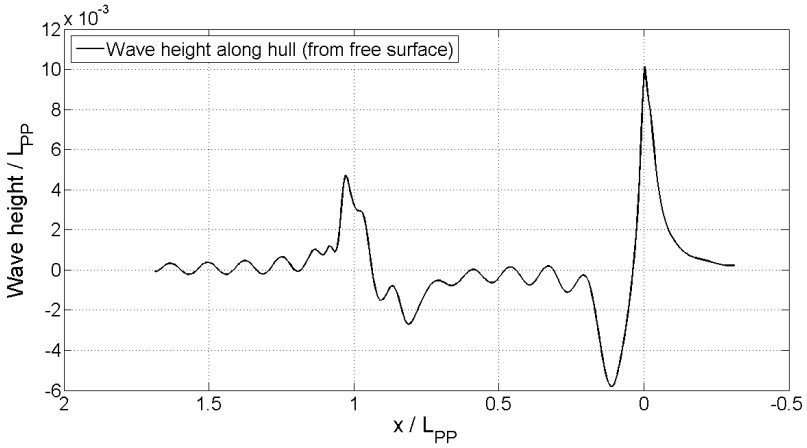

(a) Wave height along the hull

(b) Pressure coefficient (C_P) on the hull

Figure 4.4: Wave height and pressure coefficient along the hull

4.1.3 Viscous Resistance of Bare Hull

Viscous flow around the hull is solved by applying RANS method. Computational domain and boundary conditions are shown in Figure 4.1a, computational conditions are shown Table 3.3. Explicit Algebraic Stress Model (EASM) is used for all viscous resistance computations. As described before, wave pattern, sinkage & trim are calculated by the XPAN module and Froude number is rather small. Therefore it is assumed that the free surface effects are negligible. After the hull is replaced to the draft and trim, grid is calculated by XGRID and flow is calculated with the double model with XCHAP.

4.1.3.1 Verification : Grid Dependence Study

Due to the nature of finite volume method which is used for solving the differential equations for RANS method, discretization errors emerge. In theory, increasing the number of discrete cells should result in a decrease of the discretization error. However it is not always the case. In order to assess this uncertainty, a grid dependence study is done.

A set of systematically similar grids are created by the XGRID module. Figure 4.2 shows that the grid is concentrated at the bow and the stern regions where gradients are expected to be the biggest. There is an additional refinement region, which is highlighted with red curves at the stern, can be seen at Figure 4.5.

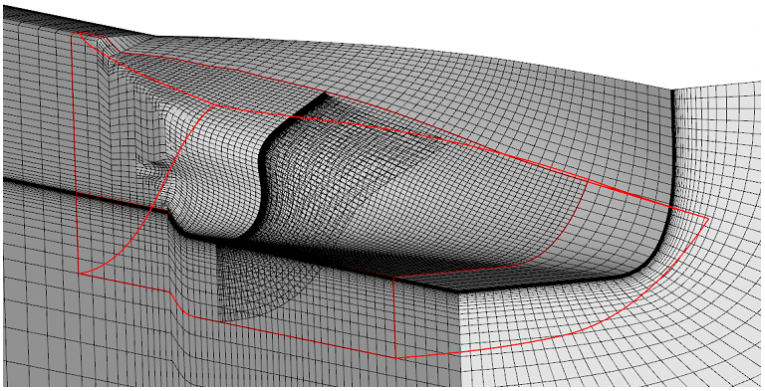

Figure 4.5: Grid refinement at the stern for the coarsest grid

Table 4.3: Grid Properties for Case 1.1a(NMRI) , bare hull resistance

No.	Grid Cells	h_i/h_1	y^+
Grid1	8009744	1.000	0.59
Grid2	4790496	1.187	0.70
Grid3	2922870	1.399	0.83
Grid4	1763984	1.656	0.99
Grid5	1070182	1.956	1.18

In total, five body-fitted structured grids are generated systematically. A uniform refinement ratio $r = h_{i+1}/h_i = \sqrt[4]{2}$ is applied in the three directions of the domain. The additional refinement region is kept the same for all grids and overlapping grids are calculated with XCHAP. No wall functions are introduced and employed y^+ values are refined with the same ratio. Attained grid cell numbers are presented in Table 4.3.

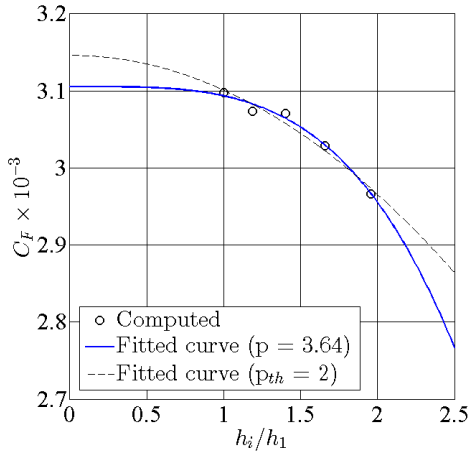

(a) Frictional resistance coefficient

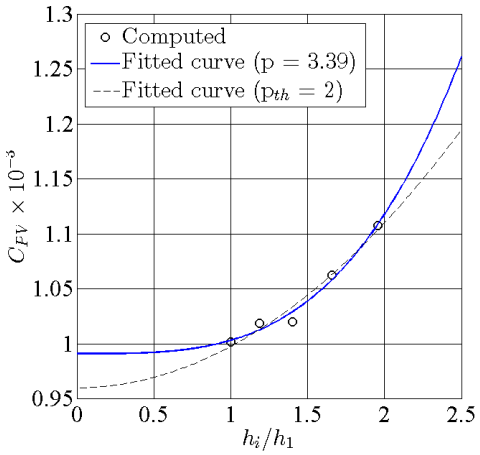

(b) Viscous pressure resistance coefficient

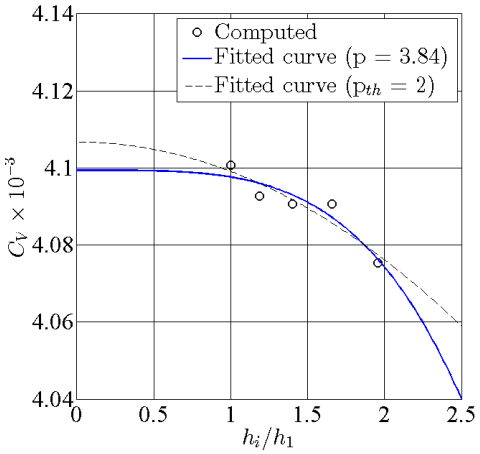

(c) Viscous resistance coefficient

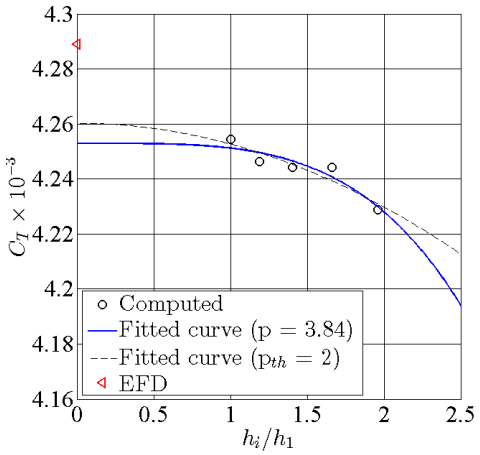

(d) Total resistance coefficient

Figure 4.6: Grid Convergence of C_F, C_{PV}, C_V and C_T for bare hull resistance case

Convergence trends of the Least Squares Root (LSR) method for the resistance components C_F, C_{PV}, C_V and C_T are presented in Figure 4.6. From the fitted curve according to LSR method, observed and theoretical order of accuracies for each component are indicated in the figures as p and p_{th} respectively. Looking at the results and attained order of accuracies for all resistance components it can be concluded that grid convergence tendencies are satisfactory.

As described in the Section 2.5.1.1, numerical uncertainties are calculated for the

resistance components C_F, C_{PV}, C_V and C_T with Least Squares Root curve fits. Iterative uncertainty U_I was predicted from the standard deviation of the force in percent of the average force over last 2000 iterations. U_I for the C_F was kept below 0.01% and for C_{PV} iterative uncertainty was kept below 1%. These uncertainties are used for calculating the iterative uncertainties of C_V and C_T by weighting the U_I of C_F and C_{PV}. U_I was assumed to be small enough to be neglected (Zou & Larsson, 2014). Predicted uncertainties and attained order of accuracies are presented in Table 4.4 for the bare hull Case1.1(NMRI). Uncertainty of each grid is denoted with the same numbering system used for grids that presented at Table 4.3. Calculated uncertainties indicates that for all resistance components, there is a grid dependent behaviour. Attained order of accuracies are higher than the theoretical order of accuracy of the prediction method(p_{th} =2).

Table 4.4: Numerical uncertainties of C_F, C_{PV}, C_V and C_T for Case 1.1a(NMRI)

	Case 1.1a(NMRI)			
	C_F	C_{PV}	C_V	C_T
p	3.64	3.39	3.84	3.84
$\|U_{SN}\%S\|_1$	4.79	12.35	0.67	0.65
$\|U_{SN}\%S\|_2$	6.63	16.65	0.90	0.87
$\|U_{SN}\%S\|_3$	9.06	22.69	1.21	1.17
$\|U_{SN}\%S\|_4$	12.68	30.07	1.65	1.59
$\|U_{SN}\%S\|_5$	17.90	39.87	2.27	2.19

where $|U_{SN}\%S|_1$ represents the numerical uncertainty U_{SN} in percent of the numerical solution S for the Grid 1. Uncertainties of other grids are shown with the similar notation in the Table 4.4.

4.1.3.2 Validation and Modelling Errors

From verification study, numerical uncertainties were predicted. In this section numerical solutions will be evaluated against experimental data in order to reveal modelling deficiencies. As described in Section 2.5.1.2, a simplified version of ASME V&V 20 Committee standard is applied. EFD result and data uncertainty are provided only for C_T and $U_D\%D$ is reported as 1% (NMRI, 2015). Comparison error is defined as $E\%D = (D - S)/D \times 100$ where D is measured values and S denotes numerical solution.

Table 4.5: Bare hull validation results for C_T

C_T	Grid 1	Grid 2	Grid 3	Grid 4	Grid 5
$E\%D$	0.81	1.00	1.05	1.05	1.40
$U_{val}\%D$	1.19	1.32	1.53	1.87	2.38
$\|E\|\%D$	0.81	1.00	1.05	1.05	1.40

In Table 4.5, validation results are presented. The condition $|E| \leq U_{val}$, where E denotes error and U_{val} denotes validation uncertainty, is observed for all grids. According to Zou & Larsson (2014), this condition means that modelling error falls within a 'noise' level which consists of numerical errors and experimental uncertainties. Therefore modelling error cannot be determined without further investigations.

Computed C_T values and experimental data are presented in Figure 4.7 together with numerical and data uncertainties. Red and horizontal bars represent the data uncertainties (U_G), while blue and horizontal bars denote the numerical uncertainties. It is observed that from coarse grid to finer grids, CFD predictions predictions gets closer to EFD measurement and U_{SN} values decreases gradually.

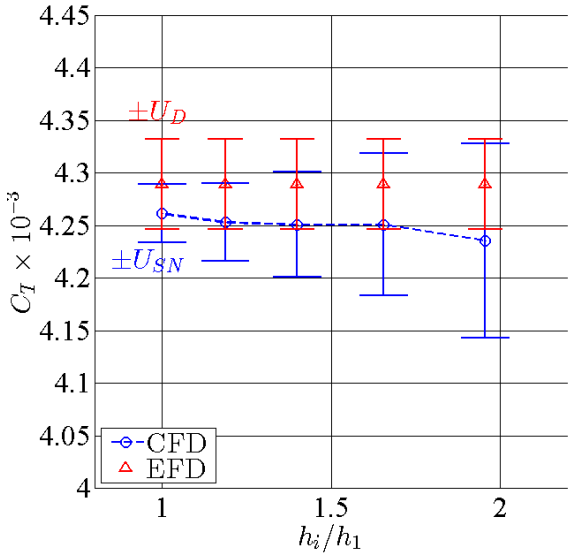

Figure 4.7: Total resistance coefficient results of bare hull

4.1.4 Viscous Resistance of Hull with ESD

Viscous flow around the hull and the appendages is solved by applying RANS method. Computational domain and boundary conditions are the same as those of the bare hull and shown in Figure 4.1a. Conditions for the computations are shown under Case 1.2a(NMRI) in Table 3.3. Explicit Algebraic Stress Model (EASM) is used for all viscous resistance computations for hull with ESD. The same assumptions for the free surface is applied as in Section 4.1.3. Therefore after potential flow calculations the ship is repositioned and then the grid is calculated by XGRID. Computations are done as double model with XCHAP.

4.1.4.1 Verification : Grid Dependence Study

In total, five body-fitted structured grids for hull, five grids for the duct and five grids for the duct strut are generated by refining all grids at the same time. Figure 4.8a and Figure 4.8b shows an example of the grids generated by the XCHAP module. A uniform refinement ratio $r = h_{i+1}/h_i = \sqrt[4]{2}$ is applied for all grids in three directions. The refinement region is the same as in the Section 4.1.3.1 and Figure 4.5. As shown in the Figure 4.8c, overlapping grids are calculated. Employed y^+ values are refined with the same ratio for three different grid as can be seen from Table 4.6, Table 4.7 and Table 4.8. In Table 4.6, Grid 1 means the overlap of finest grids of the fluid domain, duct and duct strut while Grid 5 is the overlap of coarsest ones .

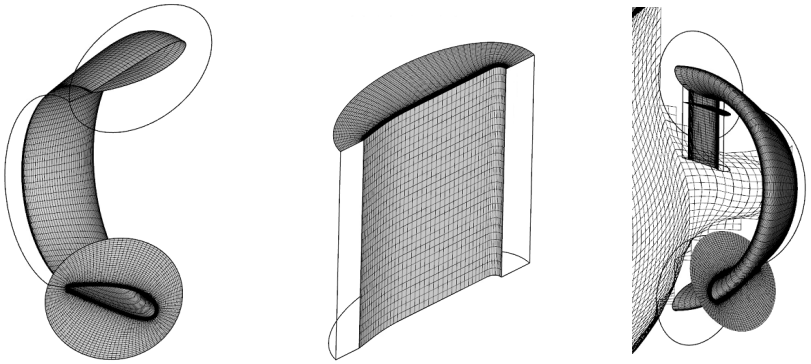

(a) Grid of duct **(b)** Grid of duct strut **(c)** Overlapping grids

Figure 4.8: Grids of hull with ESD

Table 4.6: Grid properties for Case 1.2a(NMRI) , hull with ESD resistance

No.	Grid Cells	h_i/h_1	y^+
Grid1	12034908	1.000	0.59
Grid2	7272378	1.187	0.70
Grid3	4496729	1.399	0.83
Grid4	2753581	1.656	0.99
Grid5	1691110	1.956	1.18

Table 4.7: Number of grid nodes and y^+ for duct strut

	Number of Grid Nodes			
No.	Circumferential	Radial	Axial	y^+
Grid1	283	57	85	0.1061
Grid2	238	48	71	0.1261
Grid3	200	40	60	0.1500
Grid4	168	34	50	0.1784
Grid5	141	28	42	0.2121

Table 4.8: Number of grid nodes and y^+ for duct

	Number of Grid Nodes			
No.	Circumferential	Radial	Axial	y^+
Grid1	283	57	85	0.0707
Grid2	238	48	71	0.0841
Grid3	200	40	60	0.1000
Grid4	168	34	50	0.1189
Grid5	141	28	42	0.1414

A grid dependence study is carried out for hull with ESD with five systematically refined grids. Grid convergence tendencies of C_F, C_{PV}, C_V and C_T are shown in Figure 4.9(a) $\sim$ (d) respectively. Using the LSR curve fitting method, observed order of accuracies are calculated. As can be seen from Figure 4.9, convergence rate of C_F and C_{PV} are higher than theoretical rate while C_V and C_T shows smaller rate. It can be concluded that monotonic convergence is obtained with satisfactory order of accuracies for all resistance components.

The estimated numerical uncertainties are calculated for the resistance components C_F, C_{PV}, C_V and C_T from Least Squares Root method. Iterative uncertainty U_I was predicted from the standard deviation of the force in percent of the average force over last 2000 iterations. U_I for the C_F was kept below 0.01% and for C_{PV} standard deviation was managed to kept below 1%. This uncertainties are used for calculating the iterative uncertainties of C_V and C_T by weighting the U_I of C_F and C_{PV}. U_I was negligible compared to U_G (Zou & Larsson, 2014). Predicted uncertainties and order of accuracies are presented in Table 4.9 for the Case1.2(NMRI). As described before, uncertainty of each grid is denoted with the same numbering system used for grids that presented at Table 4.6. Calculated uncertainties indicate a grid dependent behaviour for all components. Attained order of accuracies are higher than the theoretical order of accuracy of the prediction method (p_{th} =2) however convergence rate of C_V and C_T is close to theoretical order.

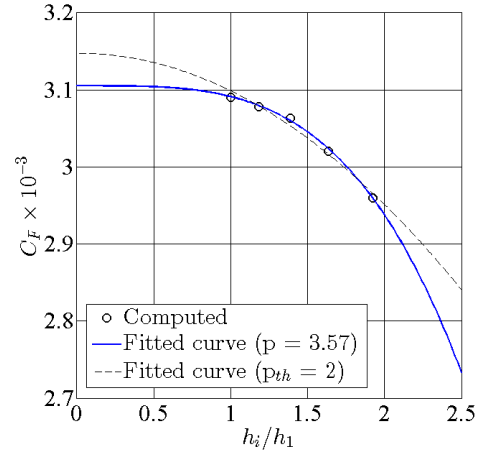

(a) Frictional resistance coefficient

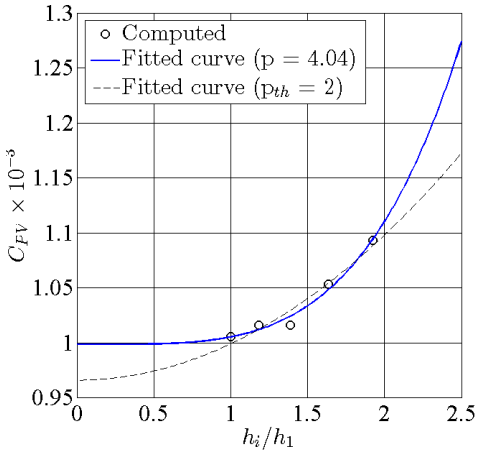

(b) Viscous pressure resistance coefficient

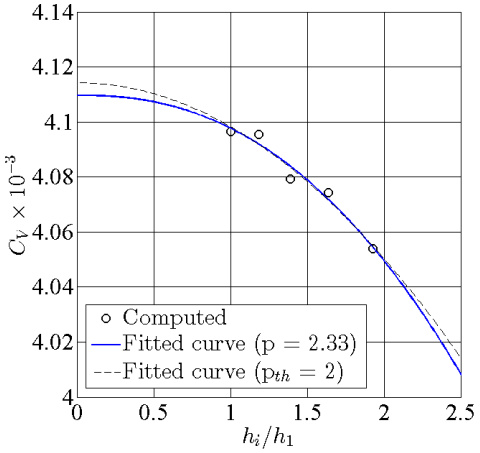

(c) Viscous resistance coefficient

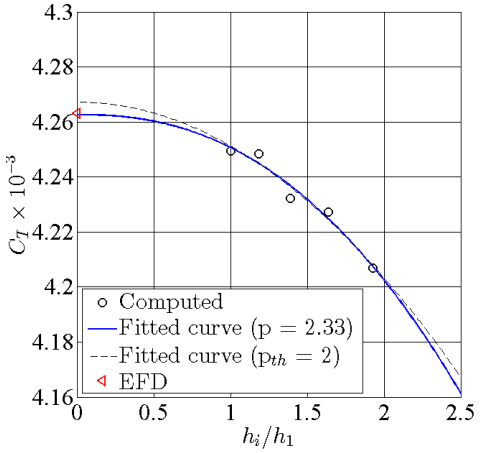

(d) Total resistance coefficient

Figure 4.9: Grid Convergence of C_F, C_{PV}, C_V and C_T for Case 1.2a(NMRI)

Table 4.9: Numerical uncertainties of C_F, C_{PV}, C_V and C_T for Case 1.2a(NMRI)

	Case 1.2a(NMRI)			
	C_F	C_{PV}	C_V	C_T
p	3.57	4.04	2.33	2.33
$\lvert U_{SN}\%S\rvert_1$	5.11	10.99	1.29	1.24
$\lvert U_{SN}\%S\rvert_2$	7.04	14.77	1.75	1.69
$\lvert U_{SN}\%S\rvert_3$	7.04	14.77	1.75	1.69
$\lvert U_{SN}\%S\rvert_4$	13.39	26.21	3.27	3.15
$\lvert U_{SN}\%S\rvert_5$	18.78	34.56	4.50	4.34

4.1.4.2 Validation and Modelling Errors

Numerical uncertainties were predicted from the grid dependence study for hull with ESD. In this section numerical solutions will be evaluated against experimental data for determining modelling errors. A simplified version of ASME V&V 20 Committee standard is applied as before. EFD result and data uncertainty are provided only for C_T and $U_D\%D$ is reported as 1% (NMRI, 2015).

Table 4.10: Hull with ESD validation results for C_T

C_T	Grid 1	Grid 2	Grid 3	Grid 4	Grid 5
$E\%D$	0.32	0.34	0.72	0.84	1.32
$U_{val}\%D$	1.59	1.96	2.49	3.28	4.40
$\|E\|\%D$	0.32	0.34	0.72	0.84	1.32

Validation results are presented in Table 4.10. As it was the case for the bare hull, validation uncertainties U_{val} are higher than comparison errors E for all grids. According to Zou & Larsson (2014), the condition $|E| \leq U_{val}$ implies that modelling error falls within a 'noise' level which consists of numerical errors and experimental uncertainties.

Computed C_T values and experimental data are presented in Figure 4.10 together with numerical and data uncertainties. Red and horizontal bars represent the data uncertainties (U_G), while blue and horizontal bars denote the numerical uncertainties. As observed for the bare hull case, from coarse grid to finer grids, CFD predictions predictions gets closer to EFD measurement and U_{SN} values decreases gradually. However hull with ESD has almost two times bigger numerical uncertainties.

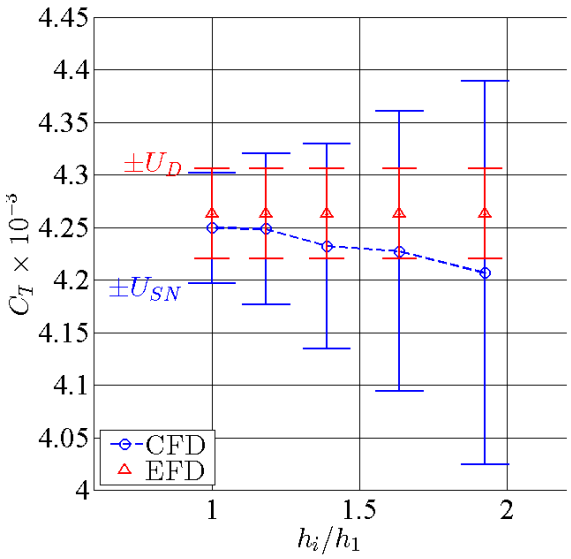

Figure 4.10: Total resistance coefficient results of hull with ESD

4.2 POW Tests

Propeller Open Water (POW) simulations are performed as described in Section 2.4.5. Forces and moments are calculated in the propeller grid with Lifting Line (LL) method and then applied to the RANS method as body forces. Explicit Algebraic Stress Model (EASM) is used for all POW computations. Grids are generated by XGRID and XCHAP modules of SHIPFLOW.

Reynolds number is the same as the self propulsion test, $Re = 7.45 \times 10^6$, and EFD provider for POW tests is National Maritime Research Institute (NMRI)(NMRI, 2015).Propeller characteristics in open water are investigated by applying POW simulations for advance ratios of $J = 0.3, 0.4, 0.5, 0.6, 0.7, 0.75, 0.8$. Since propeller simulation method is just an approximation of the real propeller, it is very important to validate the propeller characteristics before moving into the self propulsion computations. In order to find out the closest match to the actual POW results, an investigation has been carried out by varying both propeller and computational domain grids. Table 4.11 presents the variation of propeller grid

Table 4.11: POW Propeller Grid Variations

POW Case #	wplane	xupst	xdownst
Prop 1	6	0.3	0.3
Prop 2	5	0.3	0.3
Prop 3	5	0.2	0.2
Prop 4	5	0.1	0.2

where *xupst* and *xdownst* are the positions of the propeller grid inlet and outlet planes expressed as the nondimensionalized distance (by the propeller radius) from the origin of the propeller grid (Broberg et al., 2014) and *wplane* determines the plane where lifting line actuator disc is situated. Table 4.11 shows the propeller settings and an illustration of Prop 2 propeller grid is shown in Figure 4.11 where propeller grid is plotted as wireframe and the lifting line actuator disc as a red coloured surface.

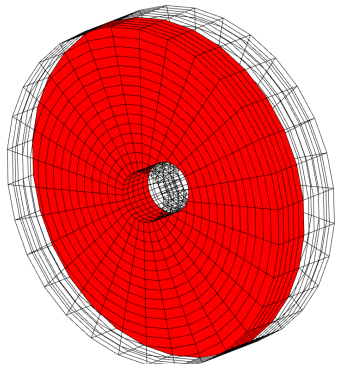

Figure 4.11: Propeller grid illustration of *xupst* = *xdownst* =0.3 and *wplane* =5

4.2.1 Computational Domain and Boundary Conditions

Coordinate system is defined as right-hand side Cartesian system and body fixed as shown in Figure 4.12a. Origin is the intersection of the propeller axis, half length of the cylindrical propeller grid and the centre-plane. Axis of the coordinate system x,y,z points at the downstream direction, starboard and upwards, respectively.

The viscous flow computations are carried out with the computational domain that consist of six boundaries is shown in Figure 4.12b. The distance between the origin and inflow plane is $8D_R$. Outflow plane however located at $10D_R$ behind the origin. All distances between slip boundaries and origin are $10D_R$ for eliminating the blockage effect as much as possible. Since the flow is unsymmetrical, no symmetry boundary condition is used for computations as shown in Figure 4.12a.

Grids for the viscous flow computations are generated by the XGRID module and XCHAP module. Default values for number of nodes in the axial, radial and tangential directions are used for generating the cylindrical propeller grid. As can be seen from Figure 4.12b and 4.13, for the grid of the fluid domain stretching functions are used in order to reach denser grid resolution where propeller grid is situated.

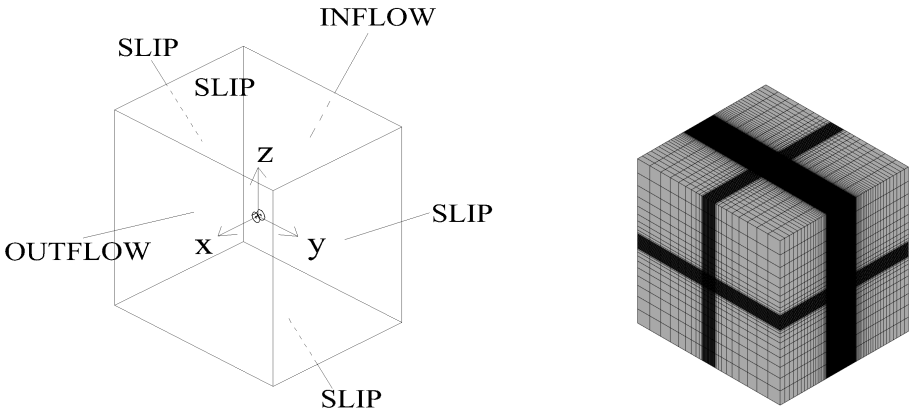

(a) Computational domain and boundary conditions for POW tests

(b) Grid distribution of the coarsest grid

Figure 4.12: Computational domain and grid distribution for POW tests

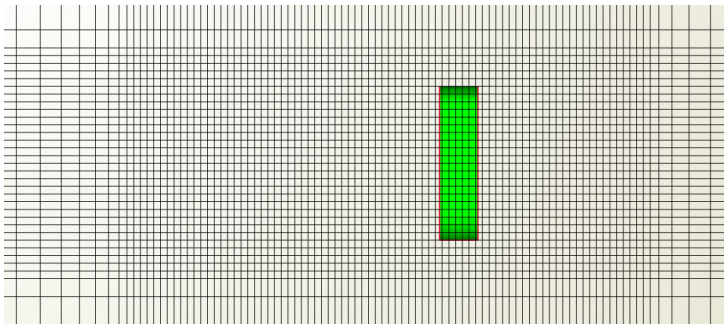

Figure 4.13: Stretched grid around the propeller grid

4.2.2 POW Prop 1

Viscous flow around around the operating propeller for different advance ratios is solved for two systematically refined grids and the Prop 1 (see Table 4.11) propeller grid settings. A grid convergence study is performed for $J = 0.6$ for five systematically refined grids. Computational domain and boundary conditions are shown in Figure 4.12a. Thrust and torque coefficients, K_T and K_Q, are calculated by the XCHAP module for corresponding advance ratios.

4.2.2.1 Verification : Grid Dependence Study ($J = 0.6$)

In order to assess the uncertainties for the POW simulations, a grid convergence study is performed for $J = 0.6$. In total, five single block structured grids are generated systematically by the XGRID module and it's overlap with the propeller grid is calculated with XCHAP module. Figure 4.12b shows that the grid is concentrated around the propeller grid where gradients are thought to be biggest. A uniform refinement ratio $r = h_{i+1}/h_i = \sqrt[4]{2}$ is applied in the three directions of the domain. Number of grid cells and number of points in x, y, z directions are are presented in Table 4.12.

Table 4.12: Grid Properties of POW Prop 1

No.	Grid Cells	x-dir.	y-dir.	z-dir.	h_i/h_1
Grid 1	2648794	242	102	102	1
Grid 2	1641416	203	86	86	1.173
Grid 3	988440	171	72	72	1.389
Grid 4	611802	144	61	61	1.630
Grid 5	371274	121	51	51	1.925

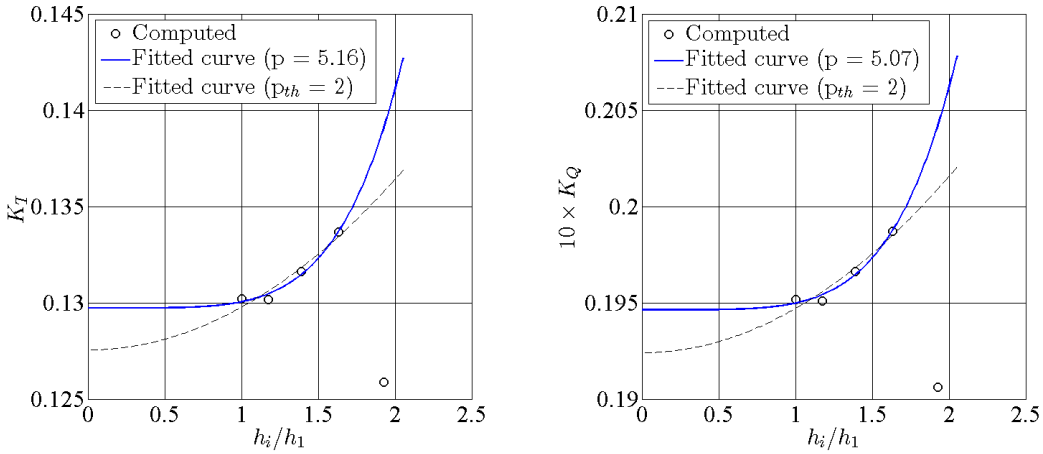

(a) Thrust coefficient **(b)** Torque coefficient

Figure 4.14: Grid Convergence of K_T and K_Q for POW Prop 1 ($J = 0.6$)

Excluding the results of the coarsest grid (Grid 5), estimated grid convergence tendencies of thrust coefficients K_T and torque coefficients K_Q are presented in Figure 4.14a and 4.14b. Convergence tendencies of both K_T and K_Q are calculated from the fitted curve according to LSR method described. Both K_T and K_Q have rather high observed order of accuracies which is indicated as p in the figures. Figure 4.14 shows the converge trend by presenting fitted curves for both attained and theoretical order of accuracies.

Numerical uncertainties are calculated for thrust coefficient K_T and torque coefficient K_Q according to Section 2.5.1.1. Predicted uncertainties and observed order of accuracies are presented in Table 4.13 for the POW Prop 1 propeller settings and advance ratio of $J = 0.6$. Uncertainty of each grid is denoted with the same numbering system used for grids that presented at Table 4.12. Calculated uncertainties indicates that there is a grid dependent behaviour. Attained order of accuracies are higher than the theoretical order of accuracy of the LSR method(p_{th} =2). Even though monotonic convergence is obtained, the reasons for high p values should be investigated further. Especially the behaviour of coarsest grid should be revealed because this grid setting is the default setup for the SHIPFLOW code POW simulations.

Table 4.13: Numerical uncertainties of K_T and K_Q for POW Prop 1 ($J = 0.6$)

	POW Prop 1	
	K_T	K_Q
p	5.16	5.07
$\|U_{SN}\%S\|_1$	5.65	3.89
$\|U_{SN}\%S\|_2$	7.58	5.22
$\|U_{SN}\%S\|_3$	10.30	7.12
$\|U_{SN}\%S\|_4$	13.77	9.57

As discussed in Section 2.5.1.1, discretization/grid uncertainty is not the only source of numerical uncertainty. Therefore the other source, iterative uncertainty U_I should be investigated. Five hundred iterations are recommended for the default grid settings for POW tests (Broberg et al., 2014). This grid properties can be seen as Grid 5 in Table 4.12. However the finest grid has almost eight times more grid cells. Therefore the number of iterations needed is a question since there is no convergence criterion for POW simulations.

In order to check iterative uncertainty U_I, finest grid (Grid 1 in Table 4.12), is computed with number of iterations ranging from five hundred to two thousand with an interval of five hundred. Figure 4.15 clearly shows that thrust coefficient K_T and torque coefficient K_Q are almost independent from the number of iterations. Since the differences were too small, K_T and K_Q values are plotted for their differences in percentage with respect to the K_T and K_Q solutions at

five hundred iterations. For example difference between the computations at five hundred iterations and i amount of iterations in percentage for thrust coefficient, $K_T(500)\%K_T(i) = (K_T(500) - K_T(i))/K_T(500) \times 100$. As Figure 4.15 shows that biggest difference does not even exceed 0.05% between the solutions from different number of iterations. Therefore it can be concluded that iterative uncertainty U_I can be neglected. Since this investigation is done for the fines grid, it is thought that similar results will be obtained with the coarser grids.

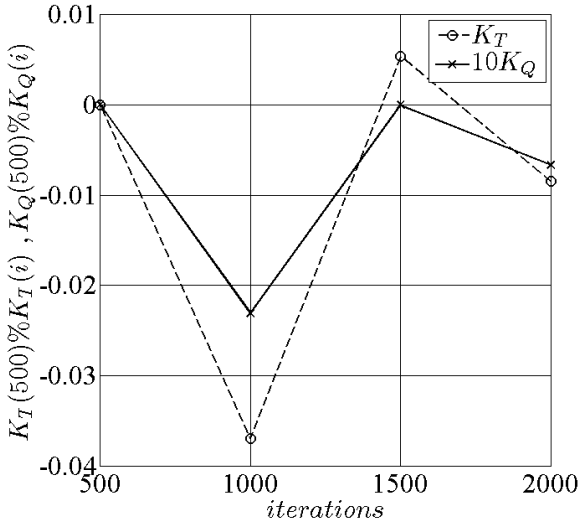

Figure 4.15: Iterative convergence of K_T and K_Q for POW Prop 1 ($J = 0.6$)

It is shown that iterative uncertainty is negligible. Therefore more thorough investigation should be done for grid uncertainty U_G. As explained in Section 2.4.5, propeller grid and background grid communicate through overlapping grids. User must be aware of the quality of interaction between two grids.
Turning the *verbose* option from one to two in SHIPFLOW code, makes full progress of the computation to be printed (Broberg et al., 2014). Forces generated in the propeller grid and exerted to the fluid domain as body forces will be plotted with this option. In an ideal case, the generated and exerted forces would be identical. However due to interpolation between two grids, there is an inevitable error. Figure 4.16 presents the error of the forces in x-direction due to overlapping grids $A\%P$, error between EFD measurement and CFD simulations $E\%D, K_T$ and $E\%D, K_Q$ for thrust and torque coefficients for $J = 0.6$. $A\%P$ is calculated

$$A\%P = \frac{F_A - F_P}{F_A} \times 100 \tag{4.1}$$

where F_P represents the passive forces which is the forces generated by propeller grid, F_A is the active forces that is applied to the fluid domain (as body forces) in x-direction.

Figure 4.16 shows that the error source in the computations is mostly caused by the interpolation between grids. Because the there is an obvious consistency between the computed K_T,K_Q and error of the interpolation $A\%P$. As pointed out in the

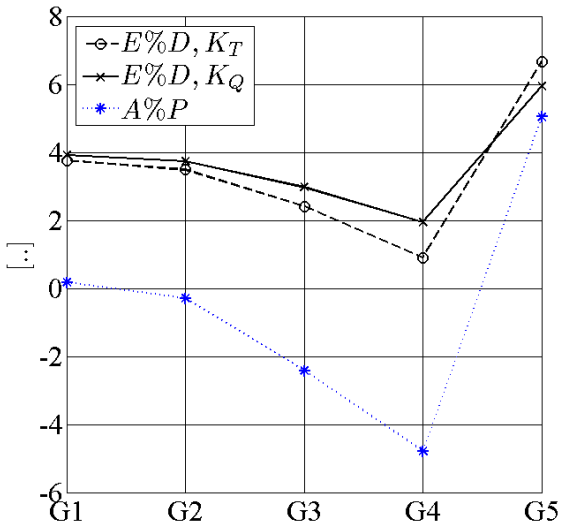

Figure 4.16: Error of the overlapping grids $A\%P$, $E\%D$ of K_T and K_Q

grid convergence study, Figure 4.14, solution of the coarsest grid was excluded. If the $A\%P$ values of coarsest grid (Grid 5) and one step finer grid Grid 4 are compared, difference in $A\%P$ is almost 10%. Therefore it can be said that Grid 5 gives a very poor overlapping grid quality. Figure 4.17 shows the coarsest and finest grids together with the propeller grid interior cells from the side view. In background grid, cells are situated at the center of the every quadrilateral. Hence Grid 5 shown in Figure 4.17a can only interact with five columns of background grid while Grid 1 interact with twelve columns of background grid. It can be said that more consistent simulations of POW can be achieved if number of columns of background grid increased.

(a) Grid 5 **(b)** Grid 1

Figure 4.17: Propeller grid interior cells for $xupst = xdownst$ =0.3 and corresponding background grids

4.2.2.2 Validation

Under the conditions described the in the Section 4.2, POW simulations were carried out for advance ratios of $J = 0.3, 0.4, 0.5, 0.6, 0.7, 0.75, 0.8$ with propeller grid Prop 1. For the fluid domain,only Grid 5 and Grid 1 (Table 4.12); coarsest and finest grids respectively were used for the computations.

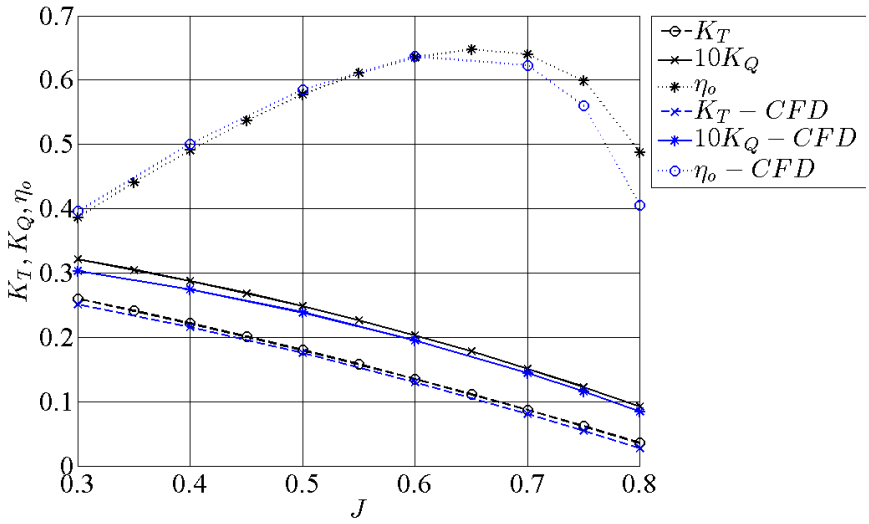

(a) Comparison of POW results of EFD and CFD POW Prop 1

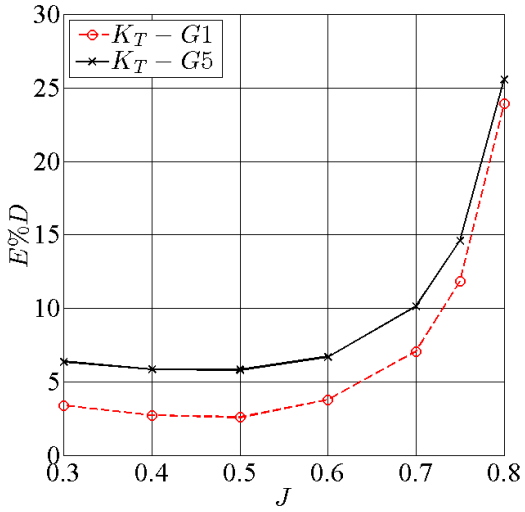

(b) $E\%D$ of Grid 1 and Grid 5 for K_Q

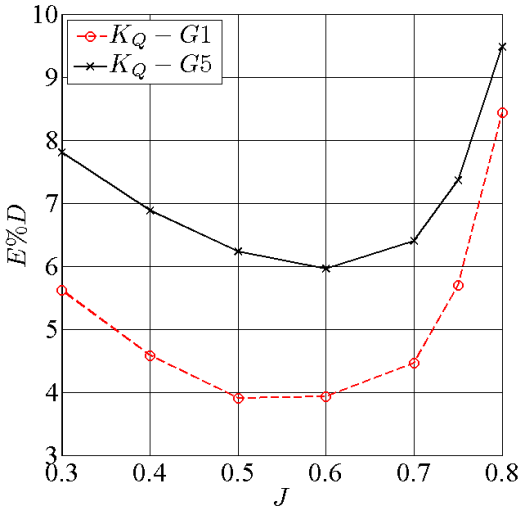

(c) $E\%D$ of Grid 1 and Grid 5 for K_Q

Figure 4.18: POW Prop 1 results for K_T, K_Q, η_o and comparison errors $E\%D$

Figure 4.18a shows the comparison between EFD measurement and CFD computation for finest grid. Except the high advance ratios such as $J = 0.7, 0.75, 0.8$, it can be said that there is a good agreement between the measured and computed values. The comparison error $E\%D = (D - S)/D \times 100$ where D is measured values and S is computed values for Grid 1 and Grid 5 are plotted in Figure 4.18b and Figure 4.18c. It is observed that with the refinement of the grid, $E\%D$ values for the thrust and torque coefficient get considerably smaller compared to the coarser grid.

4.2.3 POW Prop 2

Under the same conditions described the in the Section 4.2, POW simulations were performed for advance ratios of $J = 0.3, 0.4, 0.5, 0.6, 0.7, 0.75, 0.8$ with propeller grid Prop 2. For the fluid domain, Grid 5 and Grid 1 (Table 4.12) were used for computations.

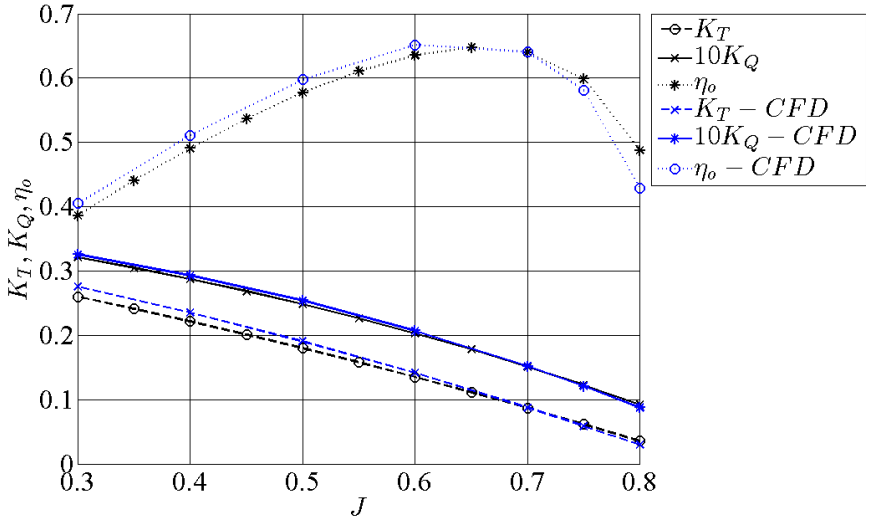

(a) Comparison of POW results of EFD and CFD POW Prop 2

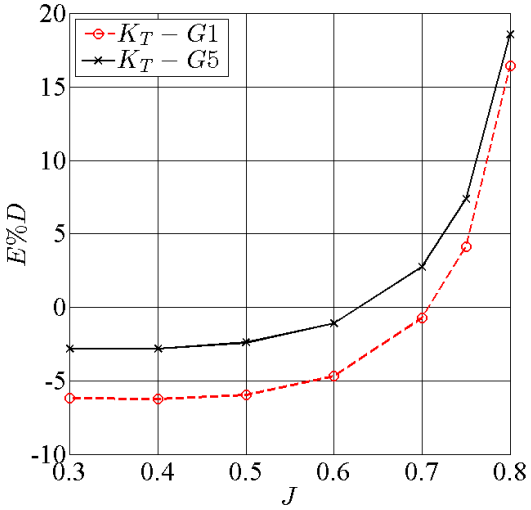

(b) $E\%D$ of Grid 1 and Grid 5 for K_Q

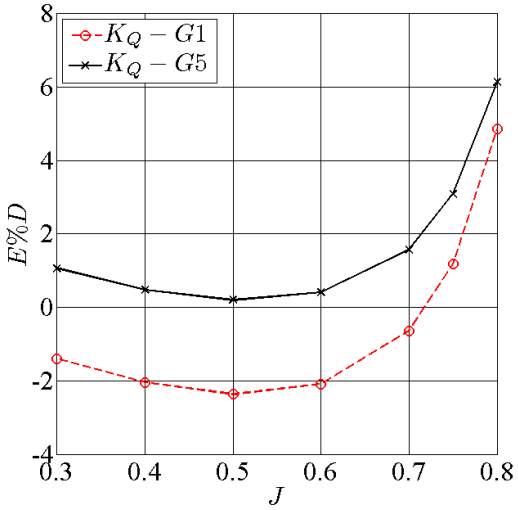

(c) $E\%D$ of Grid 1 and Grid 5 for K_Q

Figure 4.19: POW Prop 2 results for K_T, K_Q, η_o and comparison errors $E\%D$

The comparison between EFD measurement and CFD computations for finest grid is shown in Figure 4.19a. Obviously this propeller grid (Prop 2) performs worse than the Prop 1 for the fine grid. However Figure 4.18b and Figure 4.18c shows that it is the opposite for the coarse grids when Prop 2 and Prop 1 propeller grids are compared. Computations with Prop 1 propeller grid showed that finer grids, tend to move negative values of $E\%D$ relative to coarse grid solutions. This condition is cancelling some of the error for the Prop 1, while the error is increased for the Prop 2. However both computations with Prop 1 and Prop 2 when the flow field

grids are refined tend to have similar response which was expected since the only difference between two settings is the place of the actuator disc (*wplane* option) although interpolation between the grids are identical, since propeller grid lengths (default values for *xupst* and *xdownst* options) are the same.

4.2.4 POW Prop 3

POW simulations are performed for advance ratios of $J = 0.3, 0.4, 0.5, 0.6, 0.7, 0.75, 0.8$ with propeller grid Prop 3. For the fluid domain, Grid 5 and Grid 1 (Table 4.12) were used.

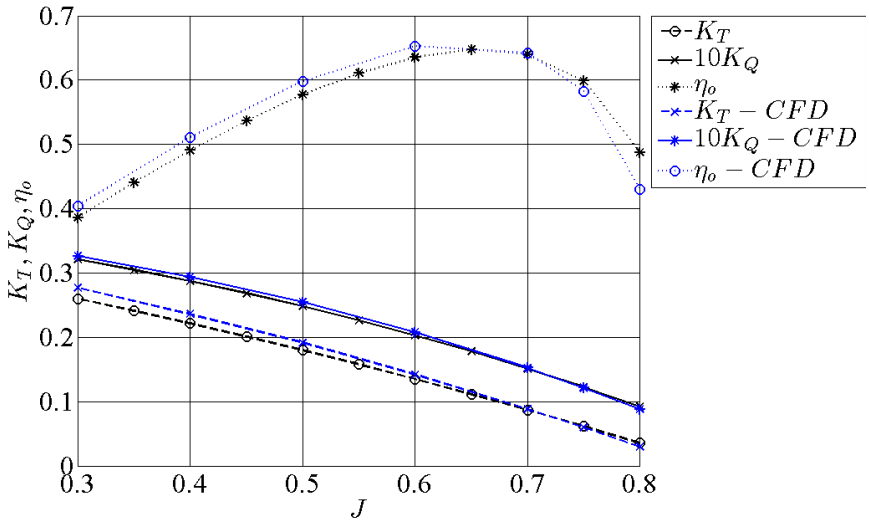

(a) Comparison of POW results of EFD and CFD POW Prop 3

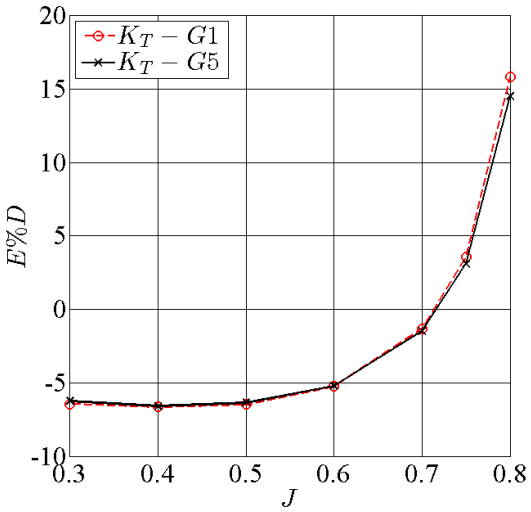

(b) $E\%D$ of Grid 1 and Grid 5 for K_Q

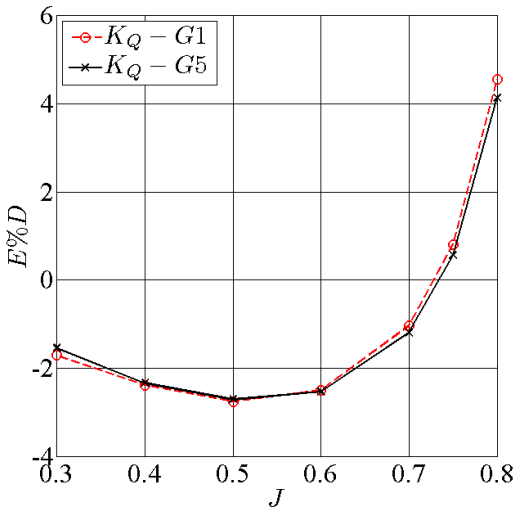

(c) $E\%D$ of Grid 1 and Grid 5 for K_Q

Figure 4.20: POW Prop 3 results for K_T, K_Q, η_o and comparison errors $E\%D$

Figure 4.20a shows the comparison between the EFD measurement and CFD computations for finest grid. Computed K_Q values shows a good agreement with the EFD results however K_T results are not close. The comparison error ($E\%D$) computed for Grid 1 and Grid 5 are plotted in Figure 4.18b and Figure 4.18c. It is

observed that there are almost no difference between coarse and fine grid. Note that propeller grid length (*xupst* and *xdownst* values) has become smaller compared to Prop 1 and Prop 2. It means that the interpolation between flow domain grid and propeller grid is more vulnerable since number of points in background grid are reduced. It is thought that ratio of active and passive forces $A\%P$ as shown in Figure 4.16 for Grid 1, is causing this condition. As suspected even for the finest grid, difference between forces is $A\%P = -5.48$. Therefore it can be concluded that even the finest grid is not fine enough with Prop 2 propeller grid settings due to poor interpolation.

4.2.5 POW Prop 4

POW simulations are carried out for advance ratios of $J = 0.3, 0.4, 0.5, 0.6, 0.7, 0.75, 0.8$ with propeller grid Prop 4. For the fluid domain,only Grid 5 and Grid 1 (Table 4.12) were used for computations.

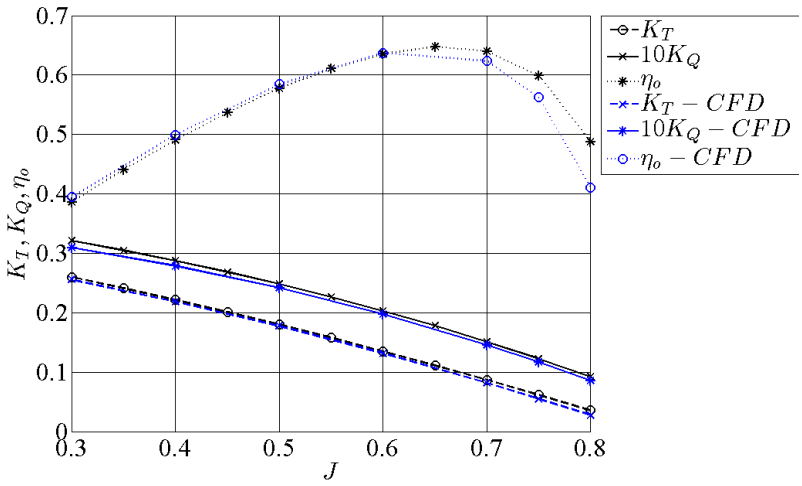

(a) Comparison of POW results of EFD and CFD POW Prop 1

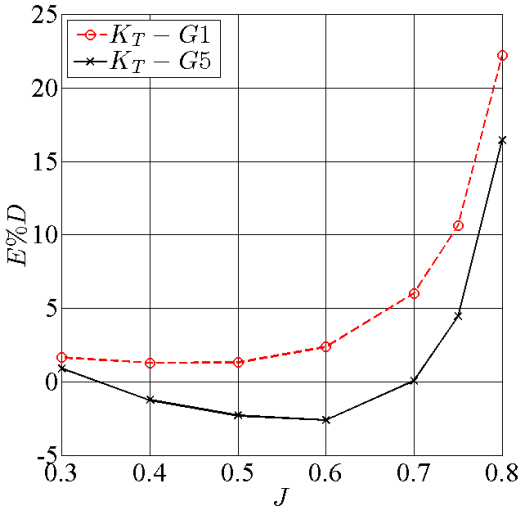

(b) $E\%D$ of Grid 1 and Grid 5 for K_Q

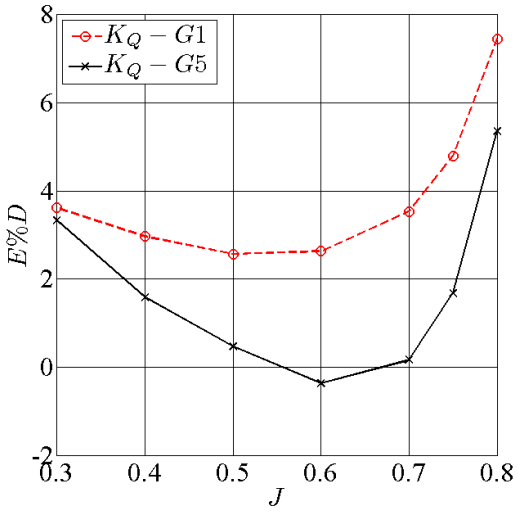

(c) $E\%D$ of Grid 1 and Grid 5 for K_Q

Figure 4.21: POW Prop 4 results for K_T, K_Q, η_o and comparison errors $E\%D$

Figure 4.21a shows the comparison between the EFD measurement and CFD computations for finest grid. So far Prop 4 propeller settings computes the closest values to the measured ones especially around the actual operating range of propeller where $J = 0.3, 0.4, 0.5$. The comparison error ($E\%D$) computed for Grid 1 and Grid 5 are plotted in Figure 4.21b and Figure 4.21c. There is a considerable change with the refinement of grid. Note that propeller grid length has become one third of the Prop1 or Prop 2 propeller grid length. It means that interpolation between flow domain grid and propeller grid is very fragile. As shown, Prop 2 propeller grid had a poor interaction with background grid, therefore there is a good chance that Prop 4 propeller grid may have the same problem. As suspected, even for the finest grid, difference between the active and passive forces is $A\%P = -6.75$. Hence it can be said that even if Prop 4 propeller grid provides the best results so far, it is due to the problem with unbalanced active and passive forces among the grids.

Results of all POW simulations presented via graphs in Section 4.2 are compiled in tables and can be found at Appendix B.

4.3 Self Propulsion

Numerical predictions for two test cases; Case 1.5a(NMRI) and Case 1.6a(NMRI) of 2015 Tokyo Workshop on CFD in Ship Hydrodynamics (NMRI, 2015) and comprehensive investigations for self propulsion test will be presented under this section. Conditions for the test cases are described in Section 3.4 and Table 3.6. Appendages for the Case 1.5a(NMRI) and Case 1.6a(NMRI) are shown in Figure 3.4. Theory and methods of viscous flow (RANS) and potential flow computations are described in Chapter 2.

4.3.1 Computational Domain and Boundary Conditions

Coordinate system is defined as right-hand side Cartesian system and body fixed as shown in Figure 4.22. The origin is the intersection of the flat free surface, the fore perpendicular (FP) and the ship centre-plane (Broberg et al., 2014). Axis of the coordinate system x,y,z point at the stern , starboard and upwards, respectively. Since the flow is unsymmetrical due to an operating propeller, for viscous flow both sides of ship are used for computations as shown in Figure 4.22. Since potential flow is not capable of calculating the hull with ESD; the same computational domain, grid and boundary conditions are used as in the Section 4.1.1 for sinkage and trim predictions. Due to low Froude number, effect of the free surface is assumed negligible. Therefore viscous simulations are performed as double model simulations.

The viscous flow computations are carried out with the computational domain that consists of five boundaries as shown in Figure 4.22. The distance between inlet and fore-perpendicular (FP) is $0.5L_{PP}$. Outlet plane however located at $0.8L_{PP}$ behind the aft-perpendicular in order to prevent wake to reach the outflow. Radius of the cylindrical outer boundary is $3L_{PP}$.

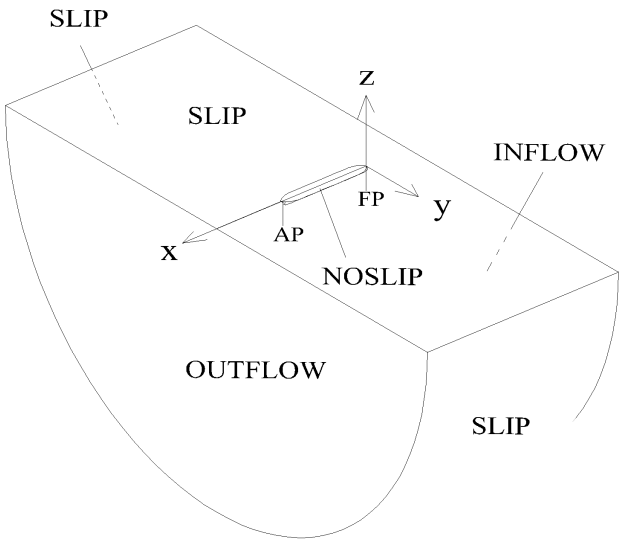

Figure 4.22: Computational domain and boundary conditions for self propulsion computations

As explained in Section 4.1.1, grids of viscous flow computations are generated similarly to the resistance computations. After the body fitted grids are developed for the hull, a refinement is applied at the stern region for the bare hull and hull with ESD cases. For the hull with ESD case, duct and duct strut grids are generated and then their overlap with other grids components are calculated by the XCHAP module. Except the symmetry condition at the center-line, body fitted grids and grids of appendages are exactly the same with the ones generated for resistance simulations described in Section 4.1. For a grid dependency study, five systematically varied grids (overlapping grids) are generated for two different refinements each. For the investigations performed on self propulsion settings, refinements and propeller grids are varied.

4.3.2 Hull without ESD

Viscous flow around the hull is solved by applying RANS method together with potential flow for propeller simulation as described in Section 2.4.5. Wave pattern, sinkage & trim are calculated by the XPAN module in the same way with Section 4.1.2. After new draft and trim is computed by potential flow, the hull is replaced to its new position. Grid, refinements and overlap are calculated by XGRID and XCHAP modules. Flow is calculated with the double model using XCHAP module. Explicit Algebraic Stress Model (EASM) turbulence model is used for computations.

4.3.2.1 Variation of Propeller Axial Positions and Grids

In this section, first part of the investigation for self propulsion simulation settings in SHIPFLOW will be presented. Under the conditions stated in Table 3.6 for Case 1.5a(NMRI), variations of propeller axial position, propeller grid and flow domain grids are simulated. As can be seen at Figure 3.2, propeller has 5° of rake. However propeller simulation is done with a cylindrical propeller grid. In this context, question of which propeller grid size should be situated at which axial position for a well representation of actual propeller is to be answered.

Propeller grid features were introduced for the investigations of POW simulations in Section 4.2. The same settings for propellers (Table 4.11) as Prop 2, Prop 3 and Prop 4 are used in this section. Hence for all propeller grids, lifting line actuator disc is situated at half the length of the cylindrical propeller grid, $wplane = 5$ (Broberg et al., 2014). On the other hand cylindrical propeller grid length is varied. Propeller grid is placed on different axial positions for an investigation of the propeller grid and the background grid interaction also examining the effect of the rake of the propeller. Table 4.14 shows the positions of the propeller grid according to the coordinate system which is described in Section 4.3.1. As can be seen from Figure 4.23; x_1 indicates the axial position at the the root of the blade or starting point of the generator line, x_2 denotes the axial position at the intersection point of generator line and 0.7× the radius of the propeller, x_3 indicates the axial position of the tip of the propeller blade and x_4 indicates the most extreme point of the propeller trailing edge.

Table 4.14: Propeller grid axial position

Position name	Propeller grid axial position at x/L$_{PP}$
x_1	0.98550
x_2	0.98639
x_3	0.98696
x_4	0.98755

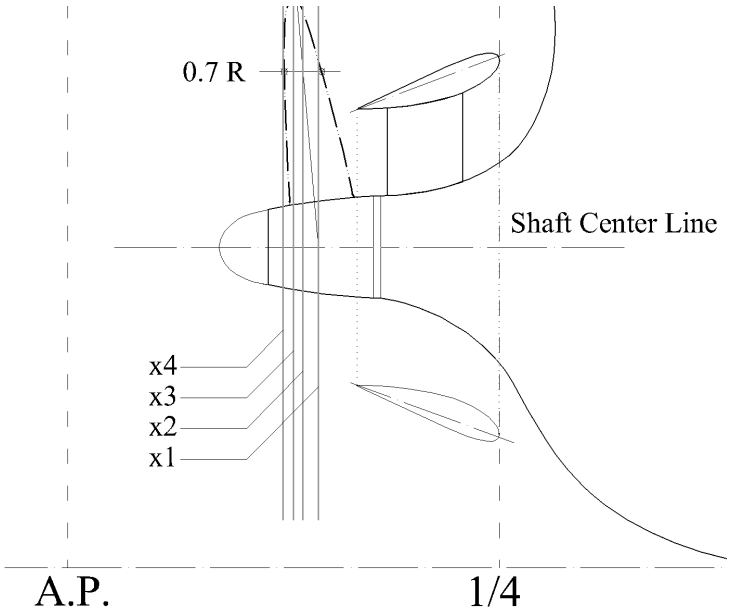

Figure 4.23: Stern view of JBC for propeller grid axial positioning

Four body-fitted structured grids are created systematically for the fluid domain. These grids are generated in the same way, but without the symmetry condition at center line, as the grids which were used for grid dependence study of viscous resistance of bare hull (Section 4.1.3.1). Table 4.15 shows the grid properties for hull without ESD together with the y^+ values. Note that in Table 4.15, Grid1 is skipped because grids are named in this section with their corresponding grids in the viscous resistance of bare hull simulations (Section 4.1.3.1). Figure 4.24 shows the coarsest grid (Grid 5) with the refinement region and cylindrical propeller grid.

Table 4.15: Grid Properties for bare hull Self Propulsion

No.	Grid Cells	y^+
Grid2	9356346	0.70
Grid3	5688114	0.83
Grid4	3417130	0.99
Grid5	2065438	1.18

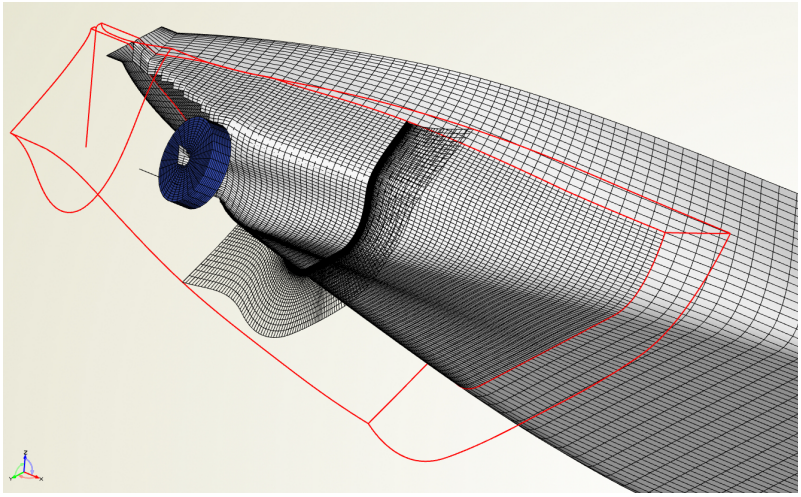

Figure 4.24: Stern view of JBC for self propulsion investigations

As explained before, four variations of fluid domain grids, four variations of axial positions of propeller and three variations of propeller grids; in total forty-eight self propulsion simulations were performed. Total resistance in self propulsion C_T, thrust coefficient K_T, torque coefficient K_Q and attained rate of revolutions n are calculated for each test case. All results of the computations can be found in the Appendix C. For convenience, computations will be presented in this section as comparison errors $E\%D$

$$E\%D = (D - S)(D) \times 100 \tag{4.2}$$

where D represents EFD measurement and S is the computed value.

Figure 4.25 and Figure 4.26 shows the results for C_T. Plots are prepared separately for each fluid domain grid with the same y-axis range for better understating.

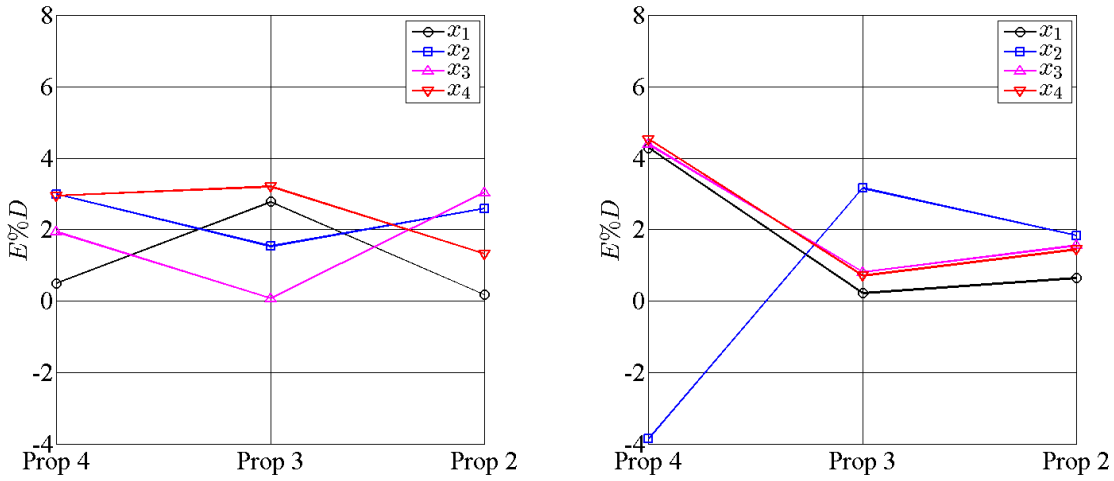

(a) $E\%D$ of C_T for Grid 5 **(b)** $E\%D$ of C_T for Grid 4

Figure 4.25: $E\%D$ of C_T for for Grid 5 and Grid 4

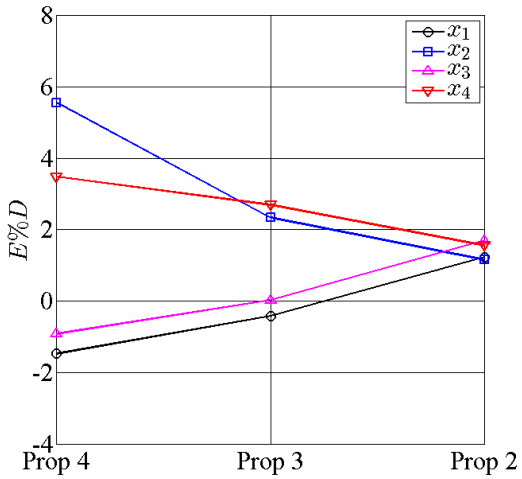

(a) $E\%D$ of C_T for Grid 3

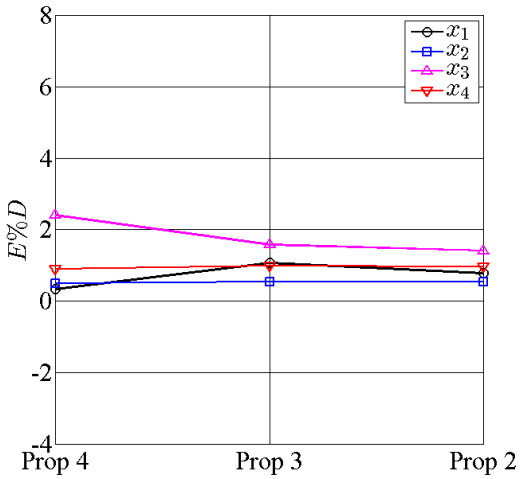

(b) $E\%D$ of C_T for Grid 2

Figure 4.26: $E\%D$ of C_T for Grid 3 and Grid 2

Comparison error $E\%D$ is placed on the y-axis while propeller grid variations are placed on the x-axis. In the legend propeller axial positions x_1, x_2, etc. are stated. From the Section 4.2 POW Tests, it is known that Prop 3 and Prop 4 propellers were not very stable because of the poor interaction with the background grid. However it can be seen in Figure 4.25a that Grid 5 (Table 4.15) cannot provide sufficient cells for a reasonable interpolation with any propeller grid. Each time propeller axial position is varied, computed C_T values changed almost randomly. As shown in Figure 4.25b and Figure 4.26a, Grid 4 and Grid 3 shows a similar trend except the Prop 2 propeller grid. Grid 2 which is the default fine grid setting in the SHIPFLOW code (Broberg et al., 2014), finally shows more consistent results with Prop 3 and Prop 2 propeller grid settings. However Prop 4 ,which is the slimmest propeller gird, still shows some variation.

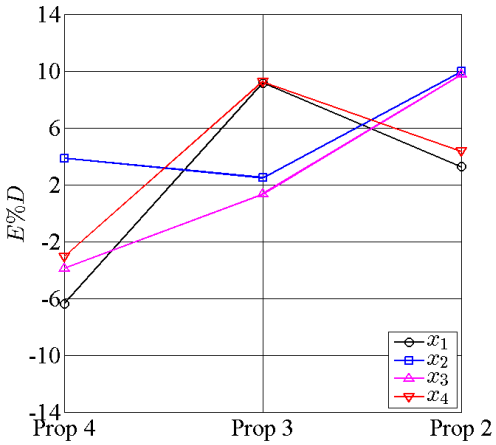

(a) $E\%D$ of n for Grid 5

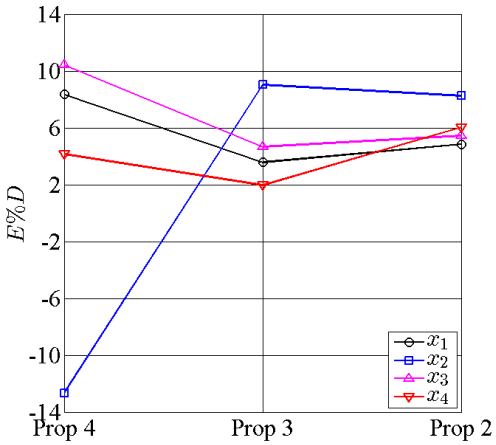

(b) $E\%D$ of n for Grid 4

Figure 4.27: $E\%D$ of n for Grid 5 and Grid 4

Computational results of the rate of revolution n are shown in Figure 4.27 and Figure 4.28. Comparison error $E\%D$ is placed on the y-axis and propeller grid variations are placed on the x-axis. Similarly coarsest grid, Grid 5, seems to provide a very poor interpolation with all propeller grid variations as can be seen in Figure 4.27a. Extensive amount of variation for Prop 4 is observed in all other grid variations. Therefore it can be concluded that Prop 4 propeller grid is too slim to have a satisfactory interpolation with fluid domain grid. As observed for C_T, Grid 2, Grid 3 and Grid 4 can provide sufficient amount of cells for a reasonable interpolation with Prop 2 propeller grid.

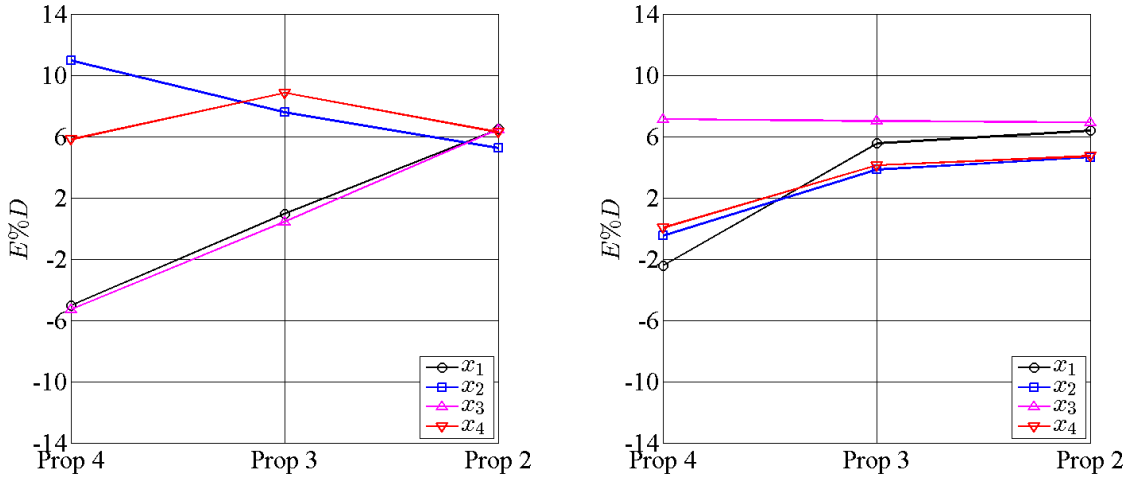

(a) $E\%D$ of n for Grid 3 **(b)** $E\%D$ of n for Grid 2

Figure 4.28: $E\%D$ of n for Grid 3 and Grid 2

Computed thrust coefficients are shown in Figure 4.29 and Figure 4.30 as comparison errors $E\%D$.

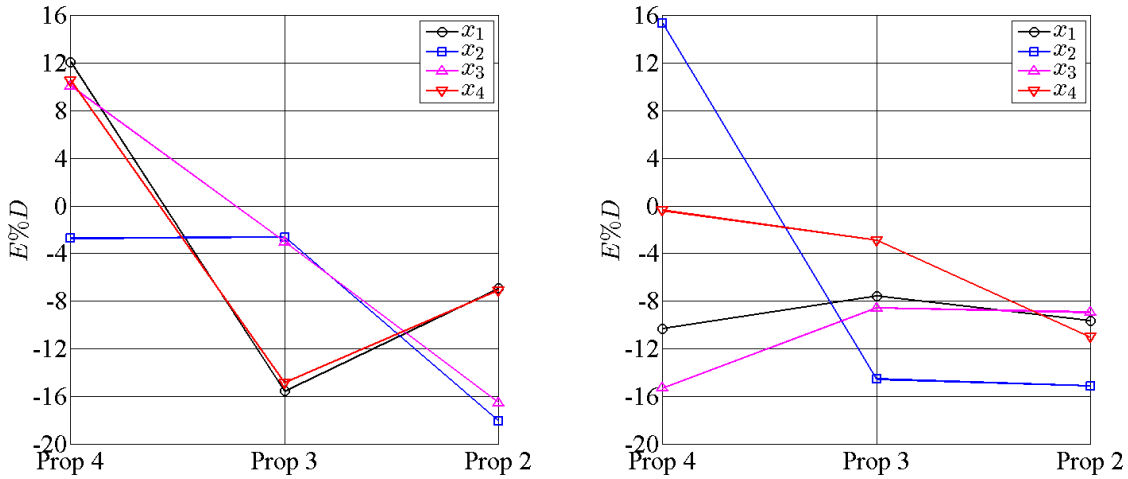

(a) $E\%D$ of K_T for Grid 5 **(b)** $E\%D$ of K_T for Grid 4

Figure 4.29: $E\%D$ of K_T for Grid 5 and Grid 4

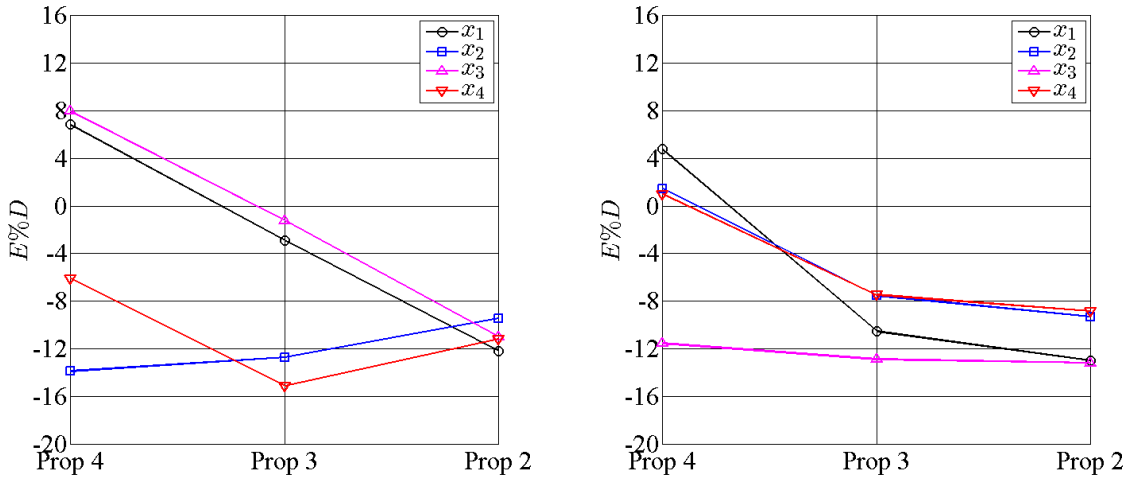

(a) $E\%D$ of K_T for Grid 3 **(b)** $E\%D$ of K_T for Grid 2

Figure 4.30: $E\%D$ of K_T for Grid 3 and Grid 2

All computations for torque coefficient will not be presented in this section but included in the Appendix C. Because there was a noticeable resemblance with the thrust coefficient K_T. This finding pointed out the computed rate of revolution, since both K_Q and K_T are nondimensionalized by n. Figure 4.31a and Figure 4.31b shows that K_T and K_Q are computed with high comparison error because of n. Since when K_T and K_Q are nondimensionalized, n^2 is in the denominator, K_Q and n are expected to be inversely proportional. Figure 4.31 clearly shows this trends. Therefore it is thought that due to poor interpolation between coarse flow domain grids and propeller grids rate of revolution varies noticeably but not C_T. Due to the variations in n, thrust and torque coefficients are computed with a very high error.

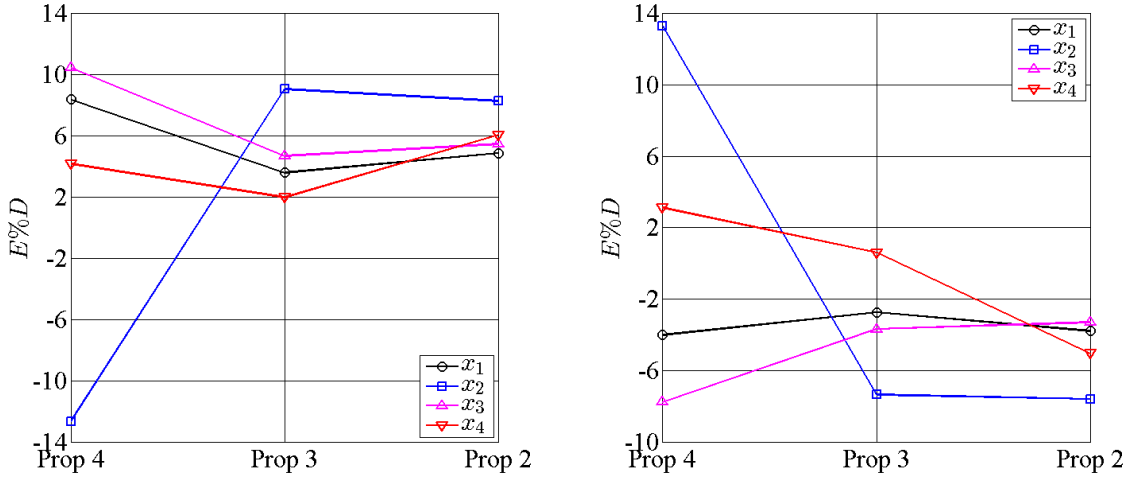

(a) $E\%D$ of n for Grid 3 **(b)** $E\%D$ of K_Q for Grid 3

Figure 4.31: $E\%D$ of n and K_Q for Grid 3

4.3.2.2 Variation of Refinement Around the Propeller Grid

In previous section, first part of the investigation has been presented. Second part of the investigations for self propulsion simulation in SHIPFLOW will be explained in this section by showing the effect of the grid density at the stern region. Conditions for the simulations are stated in Table 3.6 for Case 1.5a(NMRI). Previous section showed that coarse grids for flow domains fail to provide sufficient number of cells in order to have an accurate interpolation between propeller grid and the background grid. Therefore, grids at the stern region are refined systematically in order to figure out which grid density around the propeller grid should be obtained.

Propeller grid features were introduced for investigation for POW simulations in Section 4.2. As presented in Table 4.11; Prop 2, Prop 3 and Prop 4 are used in this section. Lifting line actuator disc is situated at half the length of the cylindrical propeller grid. As it was done in the previous section, cylindrical propeller grid length is varied and propeller grid is placed on different axial positions. Table 4.14 and Figure 4.23 shows the axial positions of the propeller grid.

Refinements in SHIPFLOW are intended to be used for resolving flow features better in the refined region. It does not improve the resolution of the geometry but only divides the existing cells into desired number of pieces in desired directions (Broberg et al., 2014). Figure 4.32 shows the refinement action in 2D. Integer values in hard brackets represents x and y directions respectively. Value of 0 means no refinement while $[1, 0]$ meaning that cells will be divided into 2^1 pieces. Similarly $[3, 0]$ means cell will be divided into $2^3 = 8$ pieces in $x-$direction.

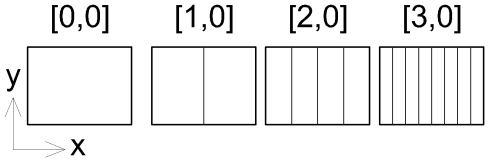

Figure 4.32: Refinement of grids in 2D

Refinements can be applied for several times for separate or overlapping regions (Broberg et al., 2014). As can be seen from Figure 4.33, two regions are determined. Region 1 is highlighted with the red boundaries while Region 2 is marked with light green boundaries. Refinements are applied to the Grid 3 flow domain grid. Because as seen in Section 4.3.2.1, fluctuations in computed results get smaller. However it still not fine enough to provide satisfactory interaction with propeller grids.

Table 4.16: Self Propulsion Refinement Descriptions

	Refinement 1	Refinement 2	Refinement 3	Refinement 4
Region 1	[1,1,1]	[1,1,2]	[1,1,1]	[1,1,1]
Region 2	-	-	[1,1,2]	[1,1,3]

Table 4.16 shows the refinement cases generated. Refinement 1 case is simply the the same configuration as Grid 3 which was computed for the previous section. First two refinement cases, Refinement 1 and Refinement 2 have only one refinement region which is Region 1, shown with the red borders in Figure 4.33. Last two cases have both regions refined with indicated levels in Table 4.16. As discussed before in the POW simulations, most important aspect for a reasonable interpolation was the number of background grid cells intersecting with propeller grid in x-direction. Refinement 2 and 3 provides two times more while Refinement 4 provides four times more cells in x-direction around the propeller compared to Refinement 1.

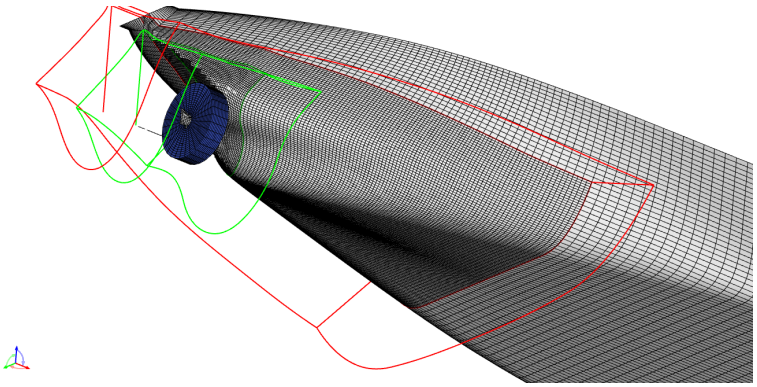

(a) Refinement 3 grid in perspective view

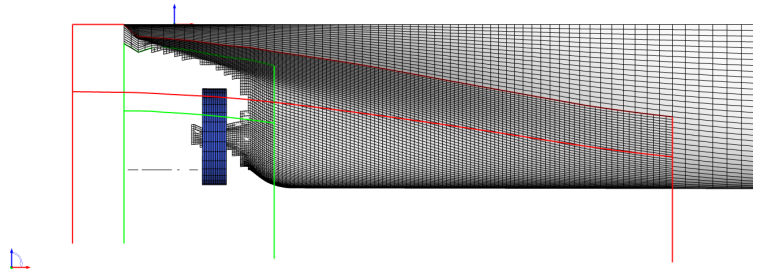

(b) Refinement 3 grid in side view

Figure 4.33: Refinement regions at stern

One body-fitted structured grid is created for the fluid domain. As presented on Table 4.16, different refinements are applied to the grid. For the reasons explained before, Grid 3 from previous section is selected. Table 4.17 shows the grid properties for different refinements. Average y^+ values are 0.7 for all refinement cases.

Table 4.17: Grid Properties for refinement cases

No.	Grid Cells
Refinement 1	5688114
Refinement 2	7889586
Refinement 3	6706482
Refinement 4	7664946

Four variations of axial positions of propeller, three variations of propeller grids and four variations of grids; in total forty-eight self propulsion simulations will be investigated. One variation of grid (Refinement 1) was already computed in the previous section, therefore thirty-six new simulations were performed and total resistance in self propulsion C_T, thrust coefficient K_T, torque coefficient K_Q and attained rate of revolutions n are calculated for each test case. All results of the computations can be found in the Appendix D. However computations will be presented in this section as comparison errors $E\%D$.

Figure 4.34 shows the results for C_T. Plots are prepared as the previous section for each fluid domain grid with the same y-axis range for better understanding. Note that plots for the Refinement 1 grid were already presented. For example, Figure 4.26a and Figure 4.34a are the same.

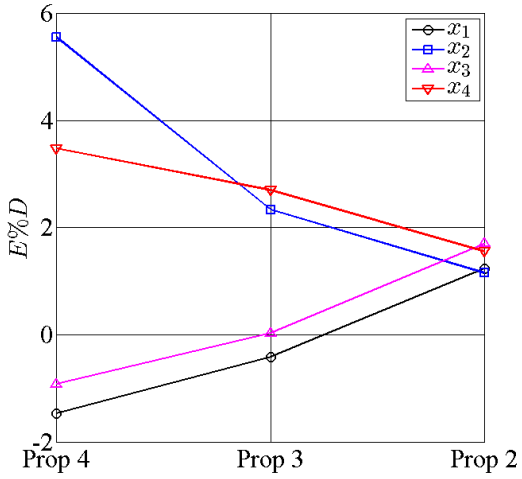

(a) $E\%D$ of C_T for Refinement 1

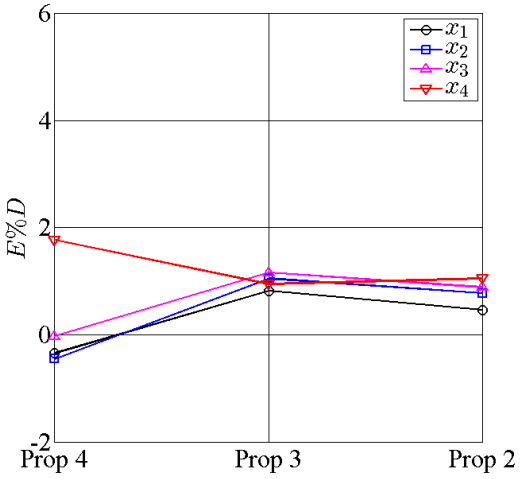

(b) $E\%D$ of C_T for Refinement 2

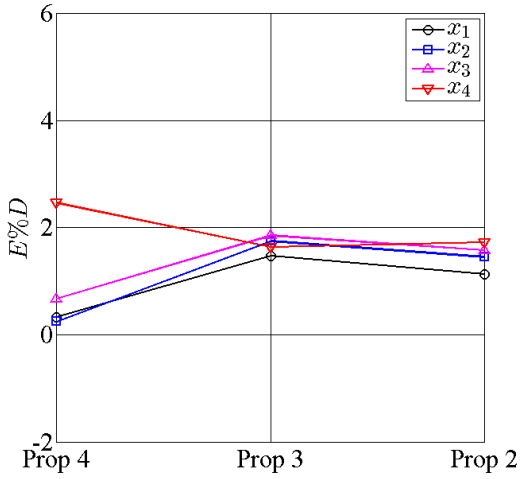

(c) $E\%D$ of C_T for Refinement 3

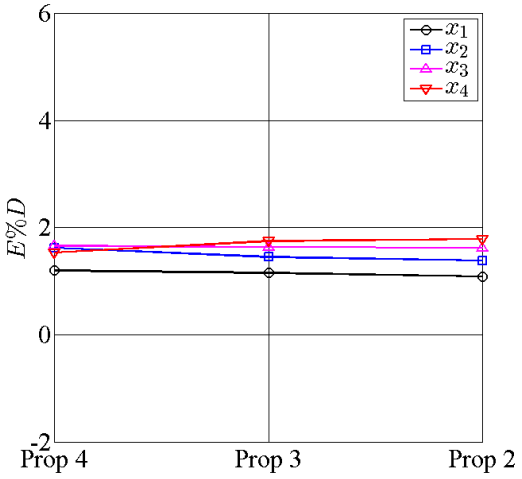

(d) $E\%D$ of C_T for Refinement 4

Figure 4.34: $E\%D$ of C_T for all refinement variations

As shown in Figure 4.34b and Figure 4.34c, computed C_T of Refinement 2 and 3 are

extremely similar even though total number of cells are considerably different. On the other hand both refinements have exactly the same grid density around the propeller grid. Another similarity is observed between Figure 4.26b and Figure 4.34c, Grid 2 from previous section(4.3.2.1) and Refinement 3 respectively. Even though Refinement 3 has almost 2.5 million less cells, computed results are similar. Figure 4.34d shows that C_T values are no more varying irregularly but with a certain trend for each propeller grid setting. It can be concluded that this background grid density around the propeller grid can provide sufficient amount of cells in x-direction for a reasonable interpolation.

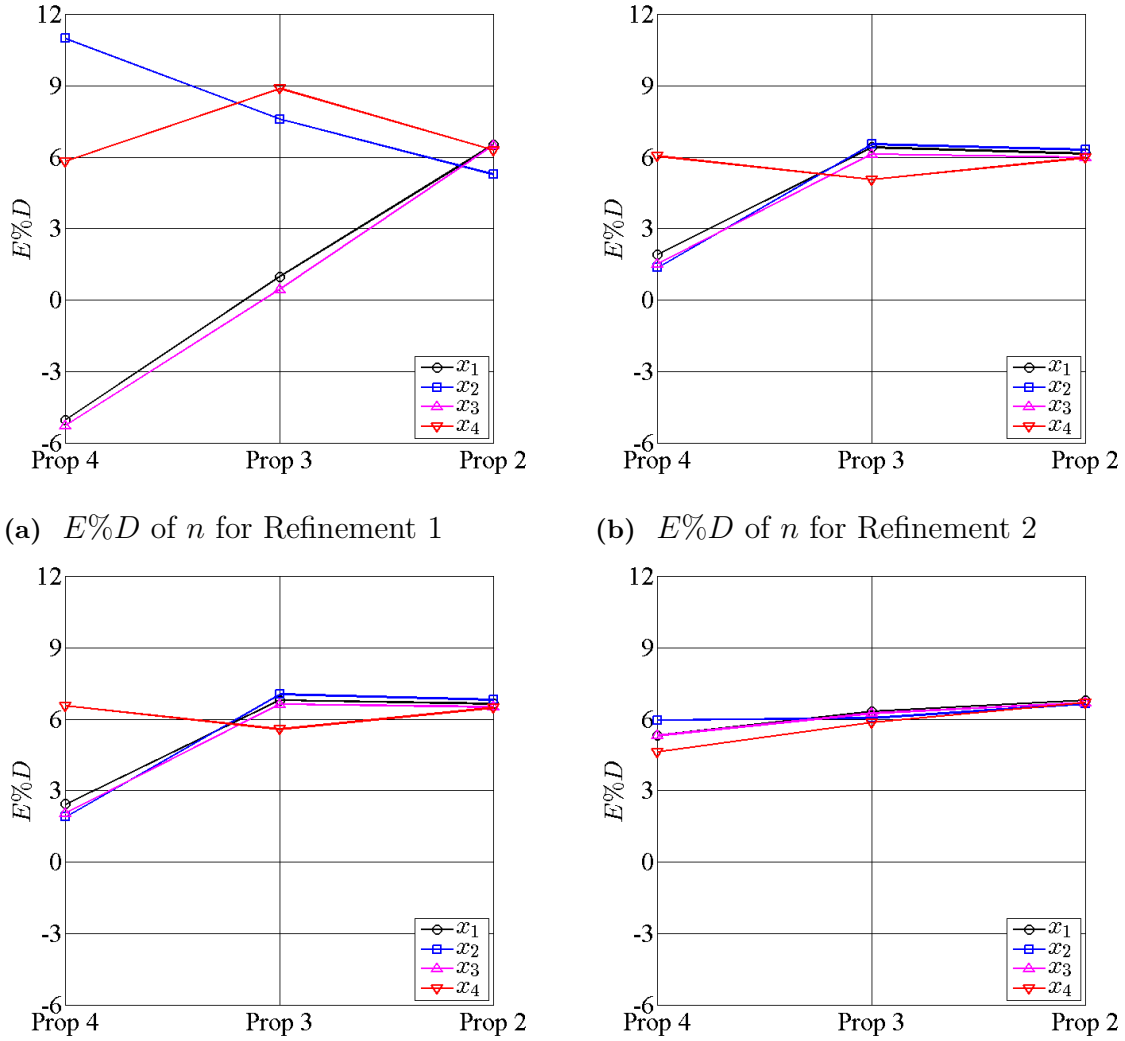

(a) $E\%D$ of n for Refinement 1

(b) $E\%D$ of n for Refinement 2

(c) $E\%D$ of n for Refinement 3

(d) $E\%D$ of n for Refinement 4

Figure 4.35: $E\%D$ of n for varying refinements

Rate of revolution n is calculated for each refinement case and shown in Figure 4.35. Similar to C_T, comparison error $E\%D$ is placed on the y-axis and propeller grid variations are placed on the x-axis. From Refinement 1 to Refinement 4, there is a clear improvement with the computations as observed for the C_T results. Also Figure 4.35b and Figure 4.35c shows that computations are almost identical with two

different refinement cases. It is thought that the flow upstream is well captured even with with the standard refinement which is Refinement 1 and if the same grid density around the propeller grid is provided, results will be very similar. Figure 4.35d shows that if grid density in Region 2 is further increased without increase of refinement in Region 1, fluctuations in the computed n almost vanish for all propeller grids variations and axial positions.

All computations for thrust and torque coefficient will not be presented in this section but included in the Appendix C. Because there was a noticeable resemblance in the K_T and K_Q computations. Briefly Refinement 4 seems to provide stable results while results of Refinement 2 and 3 are almost identical as observed for C_T and n.

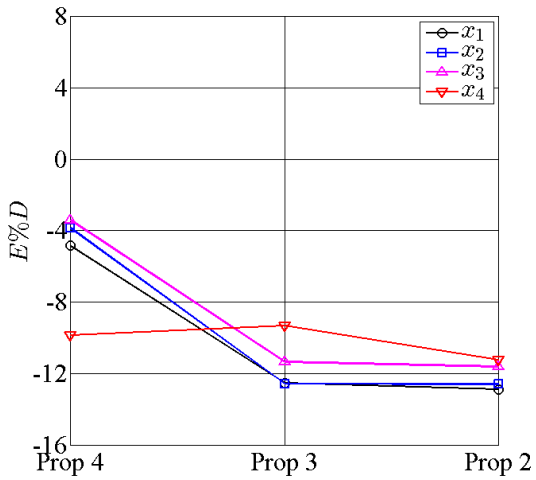

(a) $E\%D$ of K_T for Refinement 3

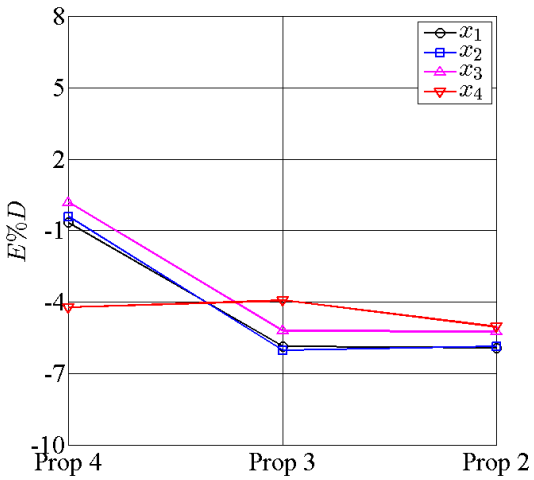

(b) $E\%D$ of K_Q for Refinement 3

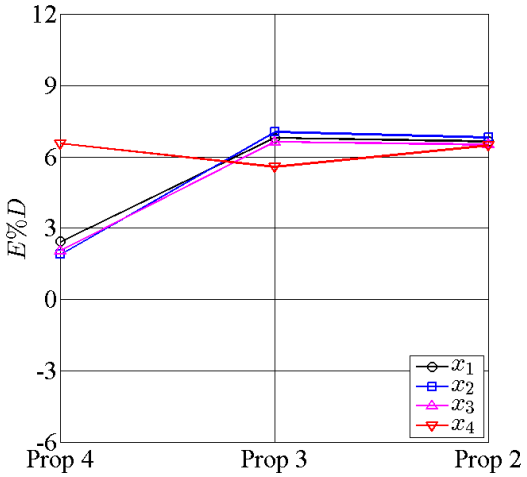

(c) $E\%D$ of n for Refinement 3

Figure 4.36: $E\%D$ of K_T, K_Q and n for Refinement 3

As emphasised in previous section, trends of K_T and K_Q are similar to each other while this similarity is inverse for n. Figure 4.36 shows this finding for the Refinement 3 grid. Since both K_Q and K_T are nondimensionalized by the n, it is thought

that K_T and K_Q are computed with considerably high $E\%D$ because of n. When K_T and K_Q are nondimensionalized, n^2 is in the denominator, hence K_Q and n are expected to be inversely proportional. Therefore it is thought that due to poor interpolation between background grid and propeller grid, rate of revolution varies noticeably but not C_T. From this finding, it could be concluded that error source of K_T is mainly not the computed thrust but n. That is because, computed thrust $T = R_T - SFC$ and error for total resistance in self propulsion is usually not even 2%. Therefore n is to be blamed for considerably high thrust and torque coefficient errors.

In SHIPFLOW code, *verbose* command determines how much information will be printed. By turning *verbose* = 2, it is possible to observe full progress of the computation including the generated forces in the propeller grid and exerted forces as body forces in the background grid. As mentioned in Section 4.2.2.1, generated and exerted forces should be identical for an ideal case. However due to interpolation between two grids, there is always a room for errors. This error $A\%P$ will be calculated as Equation 4.1.

Figure 4.36 presents the error of the forces in x-direction due to overlapping grids for Refinement 2 and 3. As mentioned many times in this section and shown in Figure 4.34b, Figure 4.34c, Figure 4.35b, and Figure 4.35c; computed results were almost identical. As expected this is the case for the $A\%P$ values too. Since the grid densities around the propeller are identical, error due to interpolation was expected to be same as shown in Figure 4.36b.

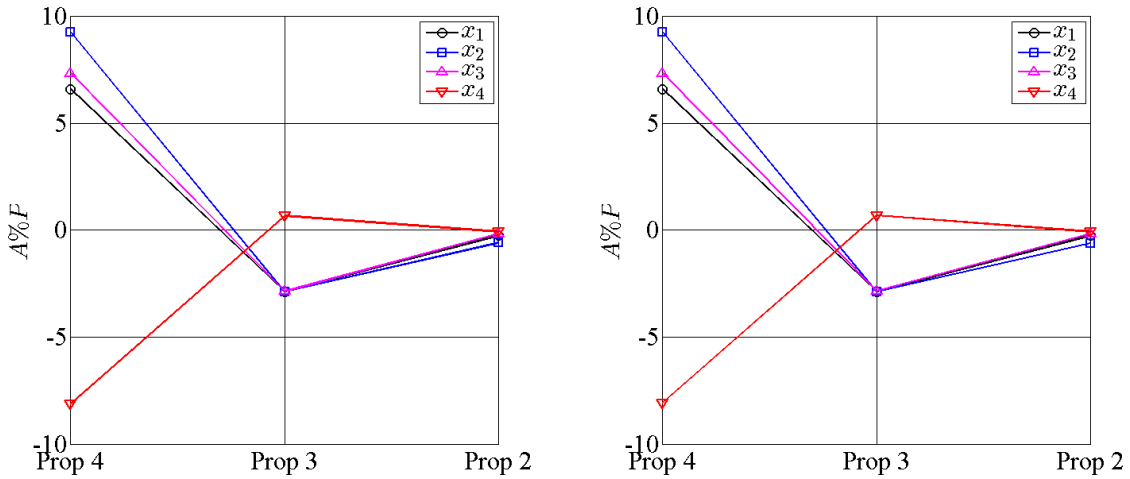

(a) $A\%P$ for Refinement 2 **(b)** $A\%P$ for Refinement 3

Figure 4.37: $A\%P$ of Refinement 2 and 3

Figure 4.38 shows the errors of the forces in x-direction due to overlapping grids and error between EFD measurement and CFD simulations $E\%D$ for n. It is clearly shown that variations for computed n values with Prop 4 propeller grid is due to the poor interpolation or in other words high $A\%P$ values.

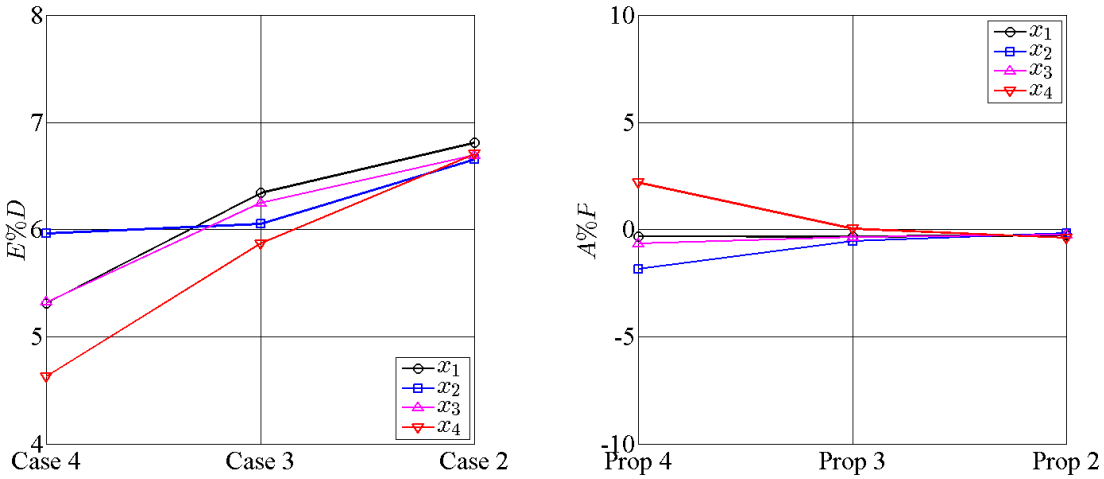

(a) $E\%D$ of n for Refinement 4 **(b)** $A\%P$ for Refinement 4

Figure 4.38: $A\%P$ and $E\%D$ of n for Refinement 4

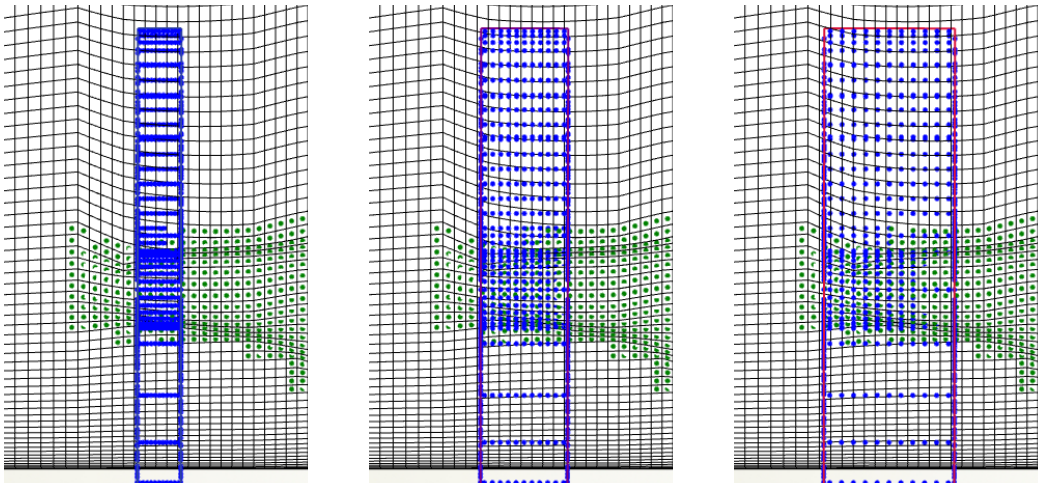

(a) Prop 4 Propeller Grid **(b)** Prop 3 Propeller Grid **(c)** Prop 2 Propeller Grid

Figure 4.39: Varying Propeller Grids at x_4 axial position with Refinement 3

Figure 4.39 shows the Refinement 3 grid together with different propeller grids from the side view. In background grid, cells are situated at the center of the quadrilaterals. Hence Prop 4 shown in Figure 4.17a can only interact with four columns of background grid while Prop 2 interact with twelve columns of background grid. By looking at Figure 4.37b for $A\%P$ values, it can be said that more consistent simulations of self propulsion can be achieved if number of columns of background grid increased with Prop 4 and Prop 3 propeller grids. Table 4.18 presents the number of columns of background grid interacting with propeller grids. From Figure 4.37b, Figure 4.38b and Table 4.18; it can be concluded that eight columns of background grid in $x-$direction is not sufficient for an accurate interpolation. Therefore user of the SHIPFLOW code must always be aware of the grid density around the propeller grid, especially in $x-$direction.

Table 4.18: Number of columns of background grid interacting with propeller grids

	Refinement 2 & 3			Refinement 4		
	Prop 4	Prop 3	Prop 2	Prop 4	Prop 3	Prop 2
x_1	4	8	12	8	16	24
x_2	4	8	12	8	16	24
x_3	4	8	12	8	16	24
x_4	4	8	12	8	16	24

4.3.2.3 Verification : Grid Dependence Study

Two grid convergence studies were performed under the conditions stated in Table 3.6 for simulation Case 1.5a(NMRI). Settings of the propeller were presented in Table 4.11. Prop 1 propeller grid is used for the grid convergence computations. Different from the investigations presented in Section 4.3.2.1 and Section 4.3.2.2, lifting line actuator disc in the propeller grid is not situated at half the length of the cylindrical propeller grid but shifted slightly, $wplane = 6$. Cylindrical propeller grid length is constant and placed on x_2 axial position where the intersection point of generator line and 0.7× the radius of the propeller intersect as seen from Figure 4.23. Coordinate system and the computational domains for both viscous and potential flow are as described in Section 4.3.1 and Section 4.1.1 respectively.

Table 4.19: Grid Properties for Case 1.5a(NMRI), hull without ESD, with Refinement 1

No.	Grid Cells	h_i/h_1	y^+
Grid 1 & Refinement 1	15697050	1.000	0.59
Grid 2 & Refinement 1	9356346	1.188	0.70
Grid 3 & Refinement 1	5688114	1.402	0.83
Grid 4 & Refinement 1	3417130	1.662	0.99
Grid 5 & Refinement 1	2065438	1.966	1.18

Two groups of body-fitted structured grids, each group consisting five grids were created systematically for the fluid domain. A uniform refinement ratio $r = h_{i+1}/h_i = \sqrt[4]{2}$ is applied in three directions of the grid. First group of grids were generated in the same way, but without the symmetry condition at center line, as the grids used for grid convergence study of viscous resistance of bare hull. As described in Section 4.3.2.2, Refinement 1 is applied to the first group of grids and they are also identical with the ones used for the first part of self propulsion test investigation which was presented in Section 4.3.2.1. Table 4.19 shows the grid properties for hull without ESD together with the y^+ values. As an example, the coarsest grid (Grid 5) with the refinement region and cylindrical propeller grid is shown in Figure 4.24.

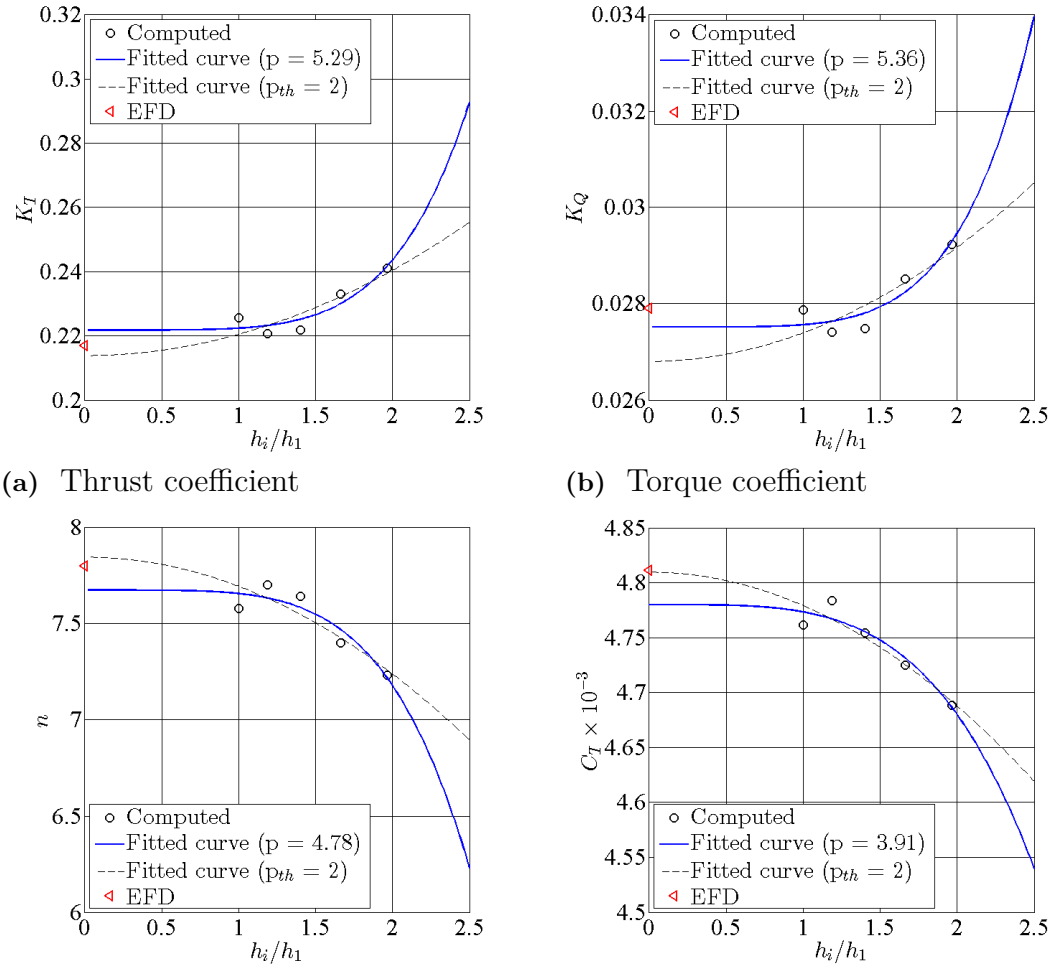

(a) Thrust coefficient

(b) Torque coefficient

(c) Rate of revolution

(d) Total resistance coefficient

Figure 4.40: Grid Convergence of K_T, K_Q, n and C_T for Case 1.5a(NMRI), hull without ESD, with Refinement 1

Figure 4.40 shows the grid convergence tendencies of the grids with Refinement 1 for K_T, K_Q, n and C_T. Observed and theoretical order of accuracies p and $p_{th} = 2$ are presented in Figure 4.40(a) $\sim$ (d). Predicted order of accuracies of all variables are considerably higher than theoretical order. In principle such high p values could mean that some of the solutions are too far away from the asymptotic range or the scatter in the computed values. Second option seems more likely since there is a noticeable oscillation in solutions.

As described in the Section 2.5.1.1, numerical uncertainties are calculated for the propulsive factors K_T, K_Q, n and C_T with Least Squares Root method. Iterative uncertainty U_I was predicted from the standard deviation of the force in percent of the average force over last 2000 iterations. U_I for the C_F was kept below 0.01%. Standard deviation of C_{PV} was managed to kept below 1% only for Grid 5 and Grid 4, on the other hand Grid 3, Grid 2 and Grid 1 varies around 1.2-1.75%. This uncertainties are used for calculating the iterative uncertainties of C_V and C_T by weighting the U_I of C_F and C_{PV}. U_I was assumed to be negligible compared to U_G,

however there is a chance that U_I may effect U_G (Zou & Larsson, 2014). Predicted numerical uncertainties and attained order of accuracies are presented in Table 4.20 for the hull without ESD, Refinement 1. Attained order of accuracies are higher than the theoretical order of accuracy of the prediction method(p_{th} =2) and all variables present grid-dependent behaviour. From coarsest grid to the finest grid numerical uncertainties are reduced noticeably. Numerical uncertainty of each grid is denoted with the same numbering system used for the grids that presented at Table 4.19.

Table 4.20: Numerical uncertainties of K_T, K_Q, n and C_T for Case 1.5a(NMRI), hull without ESD, with Refinement 1

	Case 1.5a			
	K_T	K_Q	n	C_T
p	5.28	5.36	4.78	3.91
$\|U_{SN}\%S\|_1$	11.33	8.24	7.61	2.30
$\|U_{SN}\%S\|_2$	15.30	11.05	9.93	3.07
$\|U_{SN}\%S\|_3$	20.22	14.61	13.32	4.16
$\|U_{SN}\%S\|_4$	26.04	19.05	18.67	5.73
$\|U_{SN}\%S\|_5$	34.28	25.29	26.06	7.92

Results of the first group of grids were presented above. Likewise, five grids were created systematically for the second group of grids. A uniform refinement ratio $r = h_{i+1}/h_i = \sqrt[4]{2}$ is applied in the three directions of the grid. As described in Section 4.3.2.2, Refinement 3 is applied the body-fitted structured grids. Table 4.21 shows the grid properties together with the y^+ values. As an example of the grid, refinement regions and cylindrical propeller grid is shown in Figure 4.33. Prop 1 propeller grid is used for the grid convergence computations and positioned at x_2 as seen from Figure 4.23.

Table 4.21: Grid properties of Case 1.5a(NMRI), hull without ESD, with Refinement 3

No.	Grid Cells	h_i/h_1	y^+
Grid 1 & Refinement 3	18441850	1.000	0.59
Grid 2 & Refinement 3	10996026	1.188	0.70
Grid 3 & Refinement 3	6706482	1.400	0.83
Grid 4 & Refinement 3	4029610	1.660	0.99
Grid 5 & Refinement 3	2450238	1.959	1.18

Grid convergence tendencies of second group grids for K_T, K_Q, n and C_T are shown in Figure 4.41. From the predicted order of accuracies, it is can be said that all variables converge very slowly compared to the first group of grids. Another observation is that there is a significant scatter in the computed points.

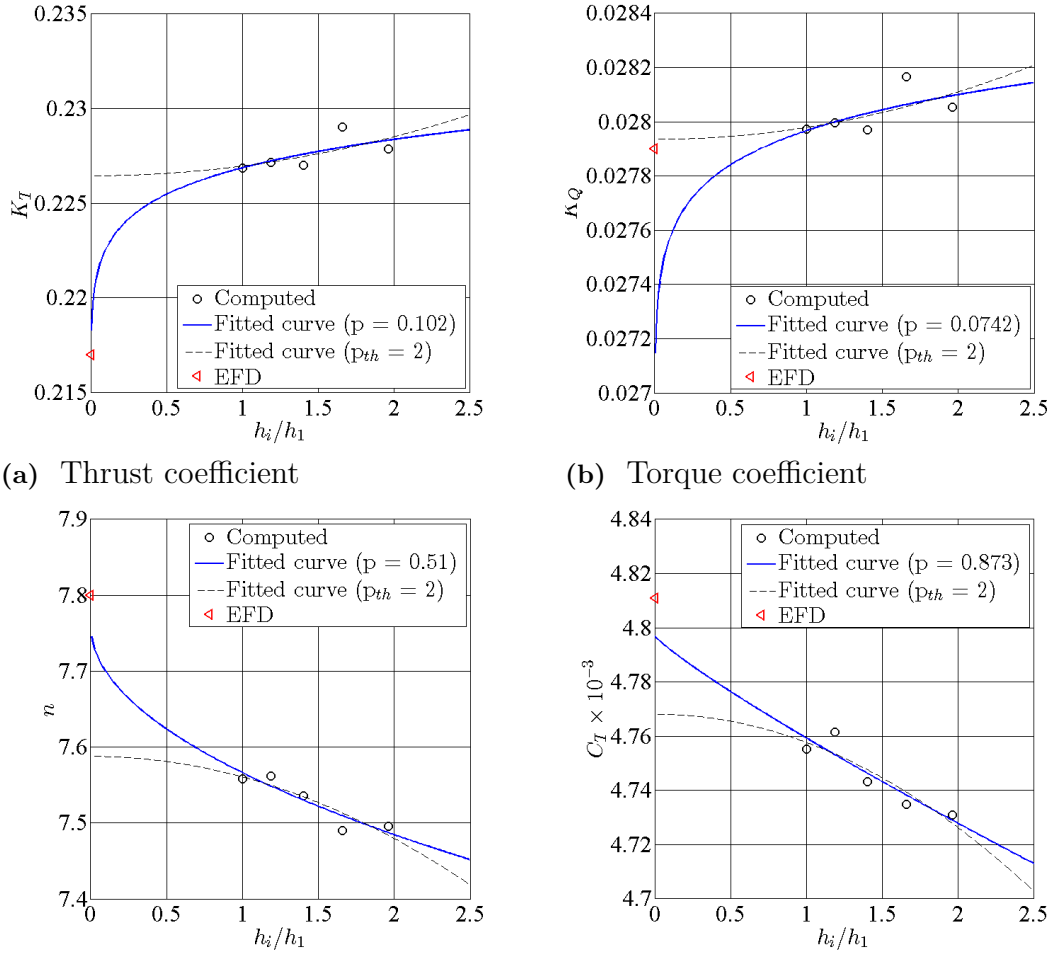

(a) Thrust coefficient

(b) Torque coefficient

(c) Rate of revolution

(d) Total resistance coefficient

Figure 4.41: Grid Convergence of K_T, K_Q, n and C_T for Case 1.5a(NMRI), hull without ESD, with Refinement 3

Numerical uncertainties U_{SN} are calculated as described in the Section 2.5.1.1 for the propulsive factors K_T, K_Q, n and C_T. Iterative uncertainty U_I was predicted from the standard deviation of the forces in percent of the average forces over last 2000 iterations. U_I of the C_F was kept below 0.01% and for C_{PV} standard deviation was managed to kept below 1%. This uncertainties are used for calculating the iterative uncertainties of C_V and C_T by weighting the U_I of C_F and C_{PV}. U_I was assumed to be negligible compared to U_G. Table 4.22 presents the the predicted order of accuracies and uncertainties for five-systematically refined grids with Refinement 3. All variables have lower p values than the theoretical order $p_{th} = 2$ especially K_T, K_Q shows a very poor convergence. In addition, the convergence of propulsive factors is not much grid dependent as the grids with Refinement 1. It is thought that by introducing the Refinement 3 uncertainties are reduced significantly as discussed in Section 4.3.2.2.

Table 4.22: Numerical uncertainties of K_T, K_Q, n and C_T for Case 1.5a(NMRI), hull without ESD, with Refinement 3

	Case 1.5a			
	K_T	K_Q	n	C_T
p	0.10	0.07	0.51	0.87
$\|U_{SN}\%S\|_1$	8.09	5.47	3.44	1.15
$\|U_{SN}\%S\|_2$	8.89	6.01	3.73	1.31
$\|U_{SN}\%S\|_3$	9.57	6.48	4.04	1.49
$\|U_{SN}\%S\|_4$	9.96	6.76	4.41	1.71
$\|U_{SN}\%S\|_5$	10.09	6.85	4.78	1.95

By turning the *verbose* option from one to two in SHIPFLOW code, forces generated in the propeller grid and exerted to the fluid domain as body forces will be plotted with this option. An ideal case will be that generated and exerted forces are identical but it is not the case due to interpolation between propeller grid and background grid. Error between these forces calculated as Equation 4.1.

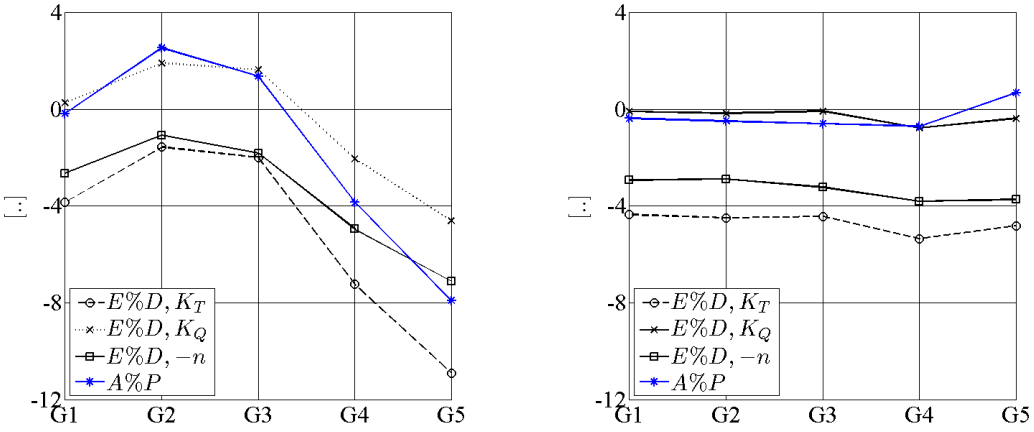

(a) $E\%D$ of K_T, K_Q, n and $A\%P$ for varying grids with Refinement 1

(b) $E\%D$ of K_T, K_Q, n and $A\%P$ for varying grids with Refinement 3

Figure 4.42: $E\%D$ of K_T, K_Q, n and $A\%P$ for Case1.5(NMRI) hull without ESD, with Refinement 1 and 2

Figure 4.42 shows the error between the active and passive forces in x-direction due to overlapping grids $A\%P$ together with comparison error between EFD measurements and CFD simulations $E\%D$ for K_T, K_Q and n. Note that rate of revolution n has negative sign for a better understanding of the plots. Figure 4.42a shows that there is an obvious similarly between the trends of $A\%P$ and propulsive factors with the Refinement 1. As discussed before in Section 4.3.2.2, it is the sign for poor interpolation. However with the Refinement 3 which means two times more background grid cells in x-direction seems to alleviating this problem as seen in Figure 4.42b. If total number of cells for Refinement 1 and 3 is compared, it could be concluded

that error between the active and passive forces $A\%P$ is almost cancelled with no significant expense. Also note that K_T and K_Q are almost parallel to the $-n$. However change in the C_T which will be presented later is quite small. This can mean that when K_T and K_Q are nondimensionalized by n, under-predicted n makes K_T and K_Q over-predicted.

4.3.2.4 Validation and Modelling Errors

Numerical uncertainties were predicted from grid dependence studies. In order to complete the V&V study, validation process should take place and computations should be evaluated against experimental data. As described in Section 2.5.1.2, a simplified version of ASME V&V 20 Committee standard is applied. EFD measurement and data uncertainty are provided only for C_T and $U_D\%D$ is reported as 1% (NMRI, 2015). Comparison error is defined as $E\%D = (D - S)/D \times 100$ where D is measured values and S denotes numerical solution.

Table 4.23: Hull without ESD & Refinement 1 validation results for C_T

C_T	Hull without ESD & Refinement 1				
	Grid 1	Grid 2	Grid 3	Grid 4	Grid 5
$U_{val}\%D$	2.48	3.22	4.23	5.71	7.78
$\|E\|\%D$	1.03	0.56	1.18	1.79	2.55

Table 4.24: Hull without ESD & Refinement 3 validation results for C_T

C_T	Hull without ESD & Refinement 3				
	Grid 1	Grid 2	Grid 3	Grid 4	Grid 5
$U_{val}\%D$	1.513	1.636	1.779	1.957	2.165
$\|E\|\%D$	1.157	1.030	1.411	1.580	1.665

In Table 4.23 and Table 4.24, validation results are presented for hull without ESD & Refinement 1 and 3 respectively. $|E| \leq U_{val}$ condition, where E denotes error and U_{val} denotes validation uncertainty, is observed for all solutions. According to Zou & Larsson (2014), this condition means that modelling error falls within a 'noise' level which consists of numerical errors and experimental uncertainties. However hull without ESD & Refinement 3 decreased the validation uncertainty significantly just by eliminating $A\%P$. Refinement 3 is not only alleviating the validation uncertainty but also improves the comparison error in coarser grids.

Computed C_T values and experimental data is presented in Figure 4.43 together with numerical and data uncertainties. Red and horizontal bars represent the data uncertainties (U_G), while blue and horizontal bars denote the numerical uncertainties (U_{SN}). Numerical uncertainties were extensive in coarse grids for hull without ESD & Refinement 1 as shown in Figure 4.43a. For convenience and better visibility

y-axis range was limited. Therefore, U_{SN} of Grid 4 and 5 with Refinement 1 could not displayed. On the other hand, Figure 4.43b shows that there is a significant improvement for numerical uncertainties.

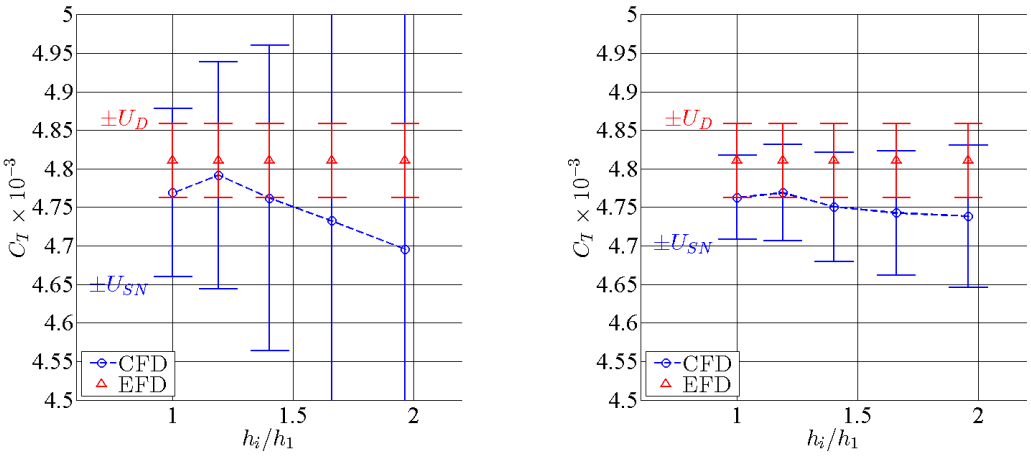

(a) Hull without ESD & Refinement 1

(b) Hull without ESD & Refinement 3

Figure 4.43: Total resistance coefficient for self propulsion results of hull without ESD

Comparison errors of C_T, K_T, K_Q and n for hull without ESD is presented in Table 4.25. As discussed earlier, hull with Refinement 1 suffers from interaction of active and passive forces between fluid domain grid and propeller grid. Numerical predictions of Grid 5 and Grid 4 differs compared to Grid 3 in hull with Refinement 1 due to error in $A\%P$. On the other hand hull with Refinement 3 seems much less grid dependent and consistent. In general, numerical predictions with fine grids are considered as satisfactory.

Table 4.25: Comparison errors of C_T, K_T, K_Q and n for hull without ESD

	Hull without ESD & Refinement 1				Hull without ESD & Refinement 3			
	C_T	K_T	K_Q	n	C_T	K_T	K_Q	n
Grid 1	1.03	-3.84	0.27	2.64	1.16	-4.34	-0.08	2.93
Grid 2	0.56	-1.55	1.92	1.06	1.03	-4.49	-0.16	2.88
Grid 3	1.18	-1.99	1.64	1.81	1.41	-4.42	-0.07	3.21
Grid 4	1.79	-7.24	-2.05	4.94	1.58	-5.35	-0.77	3.80
Grid 5	2.55	-10.90	-4.61	7.11	1.66	-4.82	-0.37	3.73

4.3.3 Hull with ESD

Viscous flow around the hull is solved by applying RANS method together with potential flow for propeller simulation as described in Section 2.4.5. Wave pattern, sinkage & trim are calculated by the XPAN module as discussed in Section 4.1.2. Therefore the effect of the duct for sinkage and trim is disregarded. New draft and trim is computed by XPAN module then the hull is replaced to its new position. Grid, refinements and their overlap is calculated by XGRID and XCHAP modules. Explicit Algebraic Stress Model (EASM) turbulence model is used for computations.

4.3.3.1 Verification : Grid Dependence Study

Under the conditions stated in Table 3.6 for simulation Case 1.6a(NMRI), two grid convergence studies were performed. As presented in Table 4.11, Prop 1 propeller grid settings were used for computations. Coordinate system and the computational domains for both viscous and potential flow is as described in Section 4.3.1 and Section 4.1.1 respectively.

Table 4.26: Grid properties for Case 1.6a(NMRI), grids with Refinement 1

No.	Grid Cells	h_i/h_1	y^+
Grid 1 & Refinement 1	19671878	1.000	0.59
Grid 2 & Refinement 1	11802412	1.186	0.70
Grid 3 & Refinement 1	7251900	1.395	0.83
Grid 4 & Refinement 1	4399952	1.647	0.99
Grid 5 & Refinement 1	2673406	1.945	1.18

Similar to the convergence study for hull without ESD, self propulsion, two groups of body-fitted structured grids each group consisting five grids were created with a uniform refinement ratio $r = h_{i+1}/h_i = \sqrt[4]{2}$. First group of grids were generated in the same way, but without the symmetry condition at center line, as the grids used for grid convergence study of viscous resistance of hull with ESD. Refinements were introduced in Section 4.3.2.2. Refinement 1 is applied to the first group of grids. Table 4.26 shows the grid properties for hull without ESD together with the y^+ values of the whole fluid domain. y^+ values for the duct and the duct strut were the same as employed before in resistance test of hull with ESD and presented in Table 4.7, Table 4.8.

Grid convergence tendencies of K_T, K_Q, n and C_T are shown in Figure 4.44(a) $\sim$ (d) respectively. Using the LSR curve fitting method, attained order of accuracies are calculated. As can be seen from Figure 4.44(a) $\sim$ (c) convergence rate of K_T, K_Q and n and are higher than theoretical rate while C_T is slightly lower. Comparing the Figure 4.40 and Figure 4.44, scatter in the computed points decreased especially for C_T. Therefore favourable reduction in p values are thought be due to reduction in the scatter.

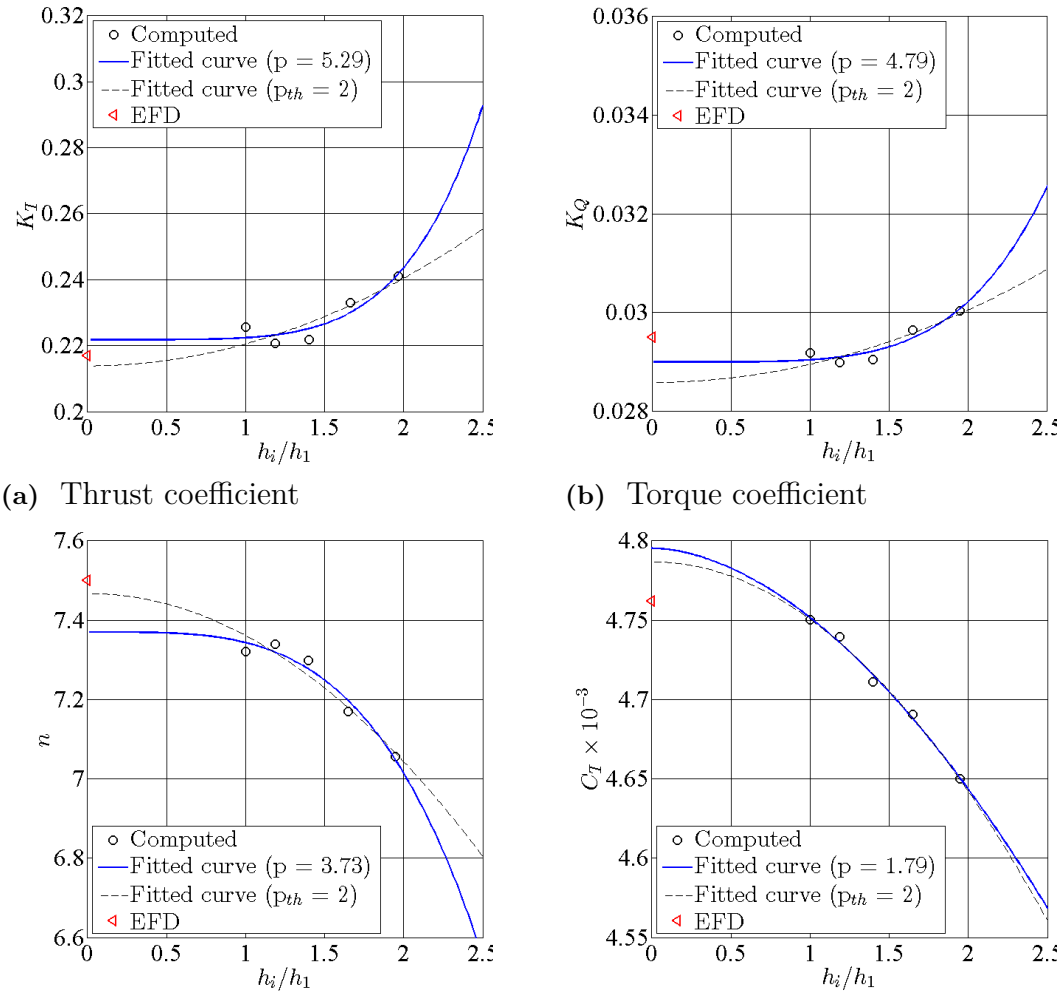

(a) Thrust coefficient

(b) Torque coefficient

(c) Rate of revolution

(d) Total resistance coefficient

Figure 4.44: Grid Convergence of K_T, K_Q, n and C_T for Case 1.6a(NMRI), grids with Refinement 1

Numerical uncertainties are calculated for the propulsive factors K_T, K_Q, n and C_T with Least Squares Root method. Iterative uncertainty U_I was predicted from the standard deviation of the forces in percent of the average forces over last 2000 iterations. U_I of C_F was kept below 0.01% and standard deviation of C_{PV} was managed to kept below 1%. This uncertainties are used for calculating the iterative uncertainties of C_V and C_T by weighting the U_I of C_F and C_{PV}. U_I was assumed to be negligible compared to U_G. Predicted uncertainties and observed order of accuracies are presented in Table 4.27 for the hull with ESD with Refinement 1. Except the C_T, observed order of accuracies are higher than the theoretical order of accuracy p_{th} =2. Monotonic convergence is gathered for all variables and highly grid-dependent behaviour is observed. Numerical uncertainty of each grid is denoted with the same numbering system used for the grids that presented at Table 4.26.

Grid convergence results of the first group of grids for Case 1.6a(NMRI) were presented above. Likewise, five grids were created with an uniform refinement ratio $r = h_{i+1}/h_i = \sqrt[4]{2}$ in the three directions of the grid. As described in Section 4.3.2.2,

Table 4.27: Numerical uncertainties of K_T, K_Q, n and C_T for Case 1.6a(NMRI), grids with Refinement 1

	Case 1.6a			
	K_T	K_Q	n	C_T
p	5.00	4.79	3.73	1.79
$\|U_{SN}\%S\|_1$	6.02	6.02	4.93	1.25
$\|U_{SN}\%S\|_2$	8.02	8.02	6.67	1.67
$\|U_{SN}\%S\|_3$	10.58	10.58	9.06	2.21
$\|U_{SN}\%S\|_4$	13.84	13.84	12.64	2.96
$\|U_{SN}\%S\|_5$	18.50	18.50	17.66	3.99

Refinement 3 is applied the body-fitted structured grids. Table 4.28 shows the grid properties together with the y^+ values. Likewise, y^+ values for the duct and the duct strut were the same as the resistance simulation of hull with ESD and presented in Table 4.7, Table 4.8. Prop 1 propeller grid is used for the grid convergence computations and positioned at x_2 axial position which can be seen in Figure 4.23.

Table 4.28: Grid Properties for Case 1.6a(NMRI), grids with Refinement 3

No.	Grid Cells	h_i/h_1	y^+
Grid 1 & Refinement 3	22416678	1.000	0.59
Grid 2 & Refinement 3	13442092	1.186	0.70
Grid 3 & Refinement 3	8270268	1.394	0.83
Grid 4 & Refinement 3	5012432	1.648	0.99
Grid 5 & Refinement 3	3058206	1.943	1.18

Figure 4.45 shows the grid convergence tendencies of second group of systematically refined grids. Curve fits for observed and theoretical order of accuracies p and $p_{th} = 2$ are presented in Figure 4.45(a) $\sim$ (d) for K_T, K_Q, n and C_T respectively. Although monotonic convergence is obtained, all variables converge very slowly compared to the the first group of grids which had the Refinement 1. Another observation is that there is a significant scatter in the computed points. Broberg et al. (2014, p.200) states that "the refinement is done by cubic interpolation in the original grid, so oscillations may occur in regions where it is not smooth", such as the aft tip of an aft bulb.

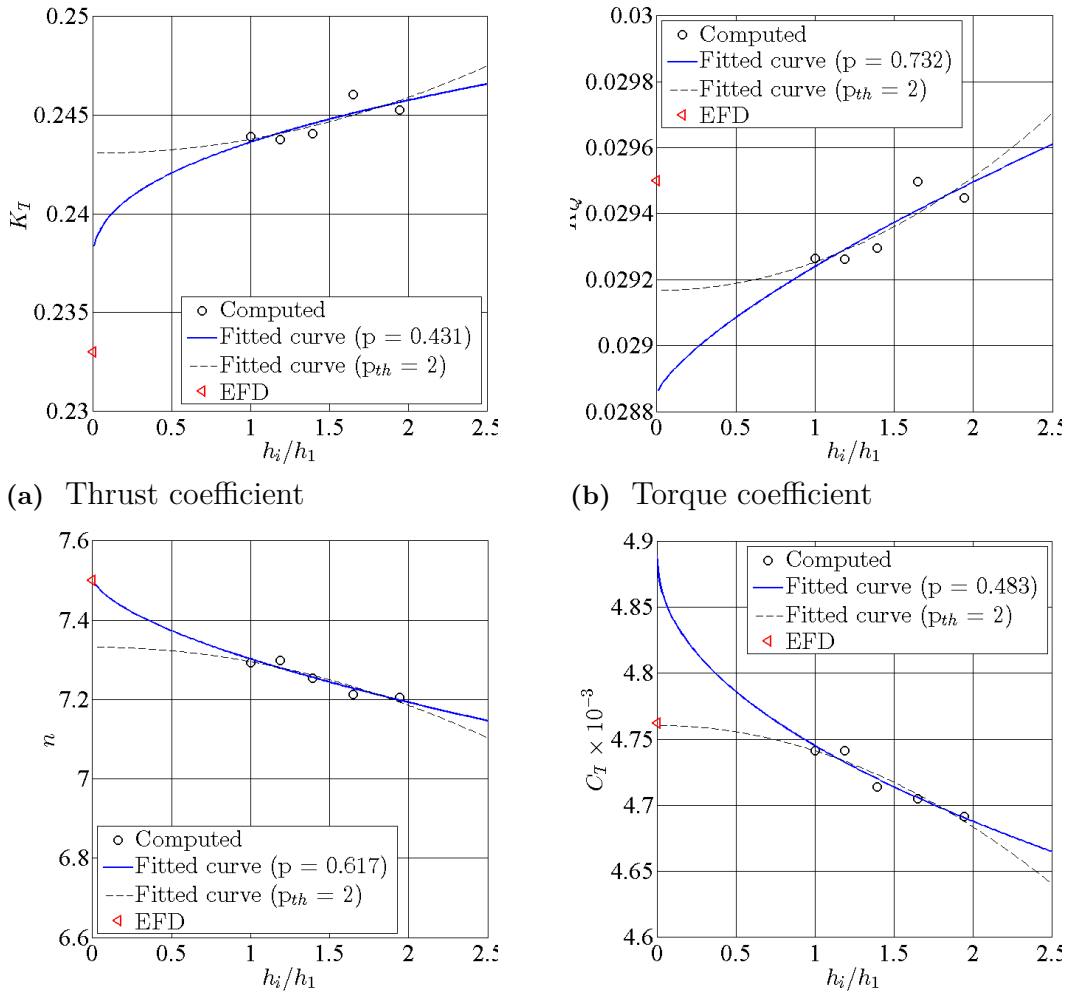

(a) Thrust coefficient

(b) Torque coefficient

(c) Rate of revolution

(d) Total resistance coefficient

Figure 4.45: Grid Convergence of K_T, K_Q, n and C_T for Case 1.6a(NMRI), grids with Refinement 3

For the second group of grids, numerical uncertainties are calculated for the propulsive factors K_T, K_Q, n and C_T with Least Squares Root curve fits. Iterative uncertainty U_I was predicted from the standard deviation of the forces in percent of the average forces over last 2000 iterations. U_I of C_F was kept below 0.01% and standard deviation of C_{PV} was managed to kept below 1%. This uncertainties are used for calculating the iterative uncertainties of C_V and C_T by weighting the U_I of C_F and C_{PV}. U_I was assumed to be negligible compared to U_G. Predicted uncertainties and observed order of accuracies are presented in Table 4.29 for the hull with ESD with Refinement 3. All propulsive factors have lower p values than the theoretical order $p_{th} = 2$. Additionally, much less grid dependent behaviour is observed compared to first group which had the Refinement 1. It is thought that by introducing the Refinement 3 uncertainties are reduced significantly as discussed for the hull without ESD self propulsion simulations.

Table 4.29: Numerical uncertainties of K_T, K_Q, n and C_T for Case 1.6a(NMRI), grids with Refinement 3

	Case 1.6a			
	K_T	K_Q	n	C_T
p	0.43	0.73	0.62	0.48
$\|U_{SN}\%S\|_1$	3.47	1.93	3.77	3.96
$\|U_{SN}\%S\|_2$	3.71	2.15	4.16	4.29
$\|U_{SN}\%S\|_3$	3.95	2.39	4.60	4.65
$\|U_{SN}\%S\|_4$	4.18	2.64	5.09	5.04
$\|U_{SN}\%S\|_5$	4.48	2.95	5.62	5.45

Forces generated in the propeller grid and exerted to the fluid domain are investigated for two groups of grids. Error between these forces denoted as $A\%P = (F_A - F_P)/F_A \times 100$ where F_P is the passive forces in other words the forces generated by propeller grid and F_A is the active forces that is applied to the fluid domain (as body forces) in x-direction. Figure 4.46 shows the error between the active and passive forces in x-direction due to overlapping grids $A\%P$ together with comparison error between EFD measurements and CFD simulations $E\%D$ for K_T, K_Q and n. Note that rate of revolution n has negative sign for a better understanding of the plots. Figure 4.42a shows that there is an similarly between the trends $A\%P$ and propulsive factors with the Refinement 1. An ideal case for $A\%P$ is zero, however it is not the case. As discussed before in Section 4.3.2.2, $A\%P$ values that are bigger than $\pm 1\%$ is the sign for a poor interpolation. Increasing the number of background grids cells, where the propeller grid situated, seems to alleviate this problem of fluctuating $A\%P$.

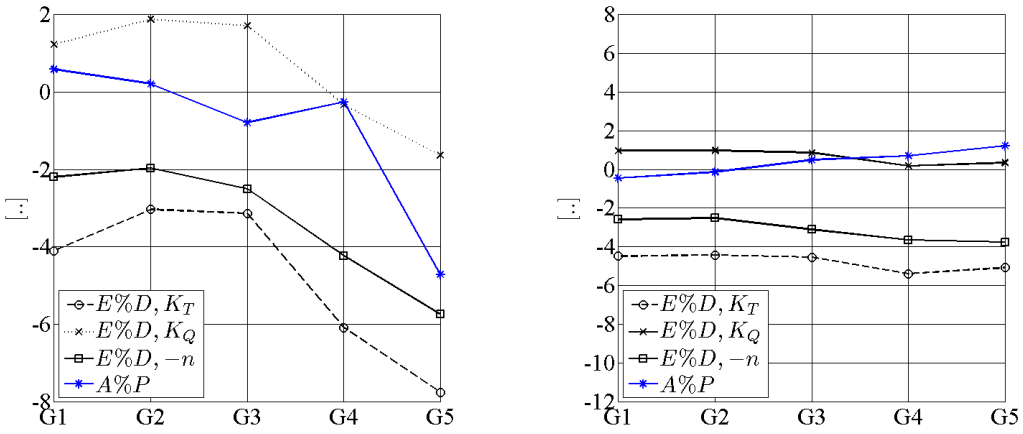

(a) $E\%D$ of K_T, K_Q, n and $A\%P$ for varying grids with Refinement 1

(b) $E\%D$ of K_T, K_Q, n and $A\%P$ for varying grids with Refinement 3

Figure 4.46: $E\%D$ of K_T, K_Q, n and $A\%P$ for Case 1.6a(NMRI), hull with ESD, Refinement 1 and 3

Another observation between hull without ESD and hull with ESD simulations with Refinement 1 is that observed order of accuracies are more reasonable and variation of computed points for hull with ESD is smaller as can be seen in Figure 4.42a and Figure 4.46a. It is thought that hull with ESD simulations become more stable thanks to the contribution of the grids cells of duct and duct strut. Figure 4.47 shows the propeller grid in blue coloured, duct in red coloured and duct strut yellow coloured wireframe. This interaction offers more points for interpolation than hull without ESD simulations therefore $A\%P$ values are getting smaller with hull with ESD self propulsion simulations.

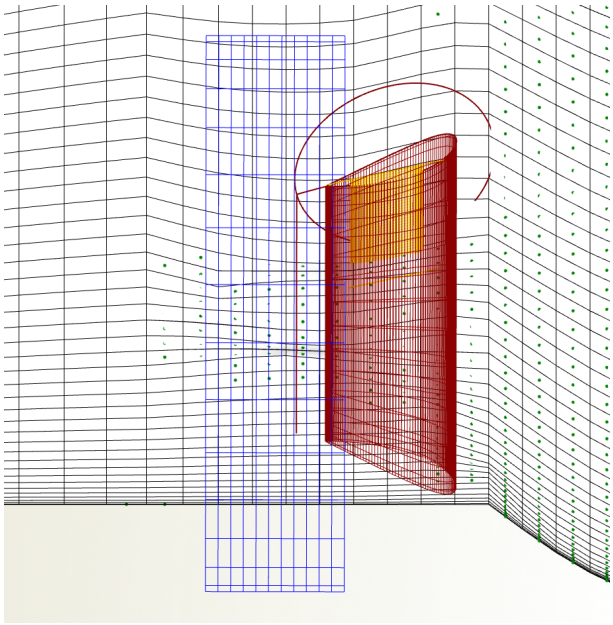

Figure 4.47: Propeller grid interacting with duct and duct strut grids

4.3.3.2 Validation and Modelling Errors

Numerical uncertainties are predicted from grid dependence studies. In this section, validation results will be explained and computations will evaluated against experimental data. As described in Section 2.5.1.2, a simplified version of ASME V&V 20 Committee standard is applied. EFD measurement and data uncertainty are provided only for C_T and $U_D\%D$ is reported as 1% (NMRI, 2015). Comparison error is defined as $E\%D = (D - S)/D \times 100$ where D is measured values and S denotes numerical solution.

Table 4.30: Hull with ESD & Refinement 1 validation results for C_T

C_T	Hull with ESD &Refinement 1				
	Grid 1	Grid 2	Grid 3	Grid 4	Grid 5
U_{val}	1.60	1.94	2.41	3.08	4.02
$\|E\|\%D$	0.24	0.47	1.07	1.50	2.35

Table 4.31: Hull with ESD & Refinement 3 validation results for C_T

C_T	Hull with ESD &Refinement 3				
	Grid 1	Grid 2	Grid 3	Grid 4	Grid 5
U_{val}	2.48	3.22	4.23	5.71	7.78
$\|E\|\%D$	1.03	0.56	1.18	1.79	2.55

In Table 4.30 and Table 4.31, validation results are presented for hull with ESD & Refinement 1 and 3. Similar to hull without ESD results; $|E| \leq U_{val}$ condition, where E denotes error and U_{val} denotes validation uncertainty, is observed for all solutions. According to Zou & Larsson (2014), this condition means that modelling error falls within a 'noise' level which consists of numerical errors and experimental uncertainties. Contrary to hull without ESD results, hull with ESD & Refinement 3 increased the validation uncertainties. Since Refinement 3 has one additional refinement region compared to Refinement 1 and it covers all appendages, two times more overlaps exist among grids. It seems like with the absence of ESD this is not an issue. However is observed that validation error increased significantly. One can question why hull with ESD & Refinement 1 performs better than hull without ESD & Refinement 1. As discussed earlier $A\%P$ was decreased by the interaction between grid of duct strut ,duct and propeller as shown in Figure 4.47.

Computed C_T values and experimental data is presented in Figure 4.48 together with numerical and data uncertainties. Red and horizontal bars represent the data uncertainties (U_G), while blue and horizontal bars denote the numerical uncertainties (U_{SN}). Numerical uncertainties are too high for the hull without ESD & Refinement 3 as shown in Figure 4.48b. On the other hand, Figure 4.48a shows that there is a significant improvement for numerical uncertainties while grid were refined.

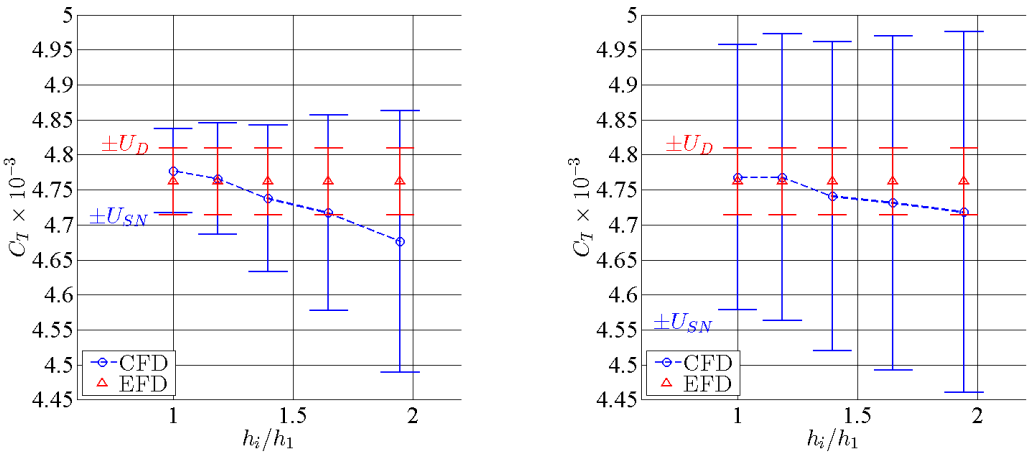

(a) Hull with ESD & Refinement 1 **(b)** Hull with ESD & Refinement 3

Figure 4.48: Total resistance coefficient for self propulsion results of hull without ESD

Comparison errors of C_T, K_T, K_Q and n for hull with ESD are presented in Ta-

ble 4.32. As discussed earlier, hull with Refinement 1 suffers less compared to the case without ESD from the interaction between fluid domain grid and propeller grid. Even though extensive numerical uncertainties were observed with Refinement 3, comparison errors are very similar to the hull with Refinement 1. In general, numerical predictions are satisfying.

Table 4.32: Comparison errors of C_T, K_T, K_Q and n for hull with ESD

	Hull with ESD & Refinement 1				Hull with ESD & Refinement 3			
	C_T	K_T	K_Q	n	C_T	K_T	K_Q	n
Grid 1	0.20	-4.10	1.23	2.20	0.41	-4.48	0.98	2.59
Grid 2	0.43	-3.03	1.88	1.97	0.41	-4.43	0.99	2.52
Grid 3	1.03	-3.13	1.72	2.50	0.99	-4.55	0.87	3.11
Grid 4	1.46	-6.09	-0.32	4.23	1.18	-5.40	0.19	3.64
Grid 5	2.31	-7.76	-1.63	5.75	1.45	-5.07	0.35	3.76

4.4 Local Flow Prediction

Viscous flow around the hull is solved by applying RANS method for the computational conditions presented in Table 3.4. Explicit Algebraic Stress Model (EASM) is used for all viscous resistance computations. Since the ship is fixed at zero sinkage & trim and Froude number is rather small, only viscous flow is computed with the double model. As seen from Table 4.3 and Table 4.6, finest grids,Grid 1, are used for the computations. Appendages for the Case 1.3a(NMRI) and Case 1.4a(NMRI) are shown in Figure 3.3.

4.4.1 Computational Domain and Boundary Conditions

The same coordinate system is defined as described in Section4.1.1. Figure 4.1a shows the body-fixed right-hand side Cartesian system where x, y, z point at the stern, starboard and upwards, respectively. The origin is at the intersection of the flat free surface, the fore perpendicular (FP) and the ship centre-plane (Broberg et al., 2014). The flow is symmetric since there is no operating propeller.Therefore half of the hull is used for computations as shown in Figure 4.1. The viscous flow computations are carried out with the computational domain that consist of six boundaries is shown in Figure 4.1a. Size of the computational domain is the same as the resistance simulations.

4.4.2 Mean Velocities and Turbulent Kinetic Energy

Mean velocities u, v, w and turbulent kinetic energy were computed for the hull with and without ESD. Three cross sections presented in Table 3.5 and Figure 3.8 will be investigated together with particle image velocimetry (PIV) measurements provided by NMRI.

4.4.2.1 Cross Section $x/L_{PP} = 0.96250$

For this cross section only isowake contours together with cross flow vectors will be presented. Plots for v, w and k can be found at the Appendix F. Figure 4.49 shows the EFD-CFD comparison of isowake contours. Even though the EFD measurement plot Figure 4.49a is unclear close to the hull, at the lower part of the gondola a separation is observed. This separation is also captured by CFD computations. EFD measurement at hull with ESD test is even more unclear close to the hull, but it seems very similar to bare hull EFD measurements. On the other hand, as seen in Figure 4.50b, in CFD computations separation region gets thinner but lower velocities propagate through the vortex center. It could be concluded that there are good agreements between EFD measurements and CFD computations in general.

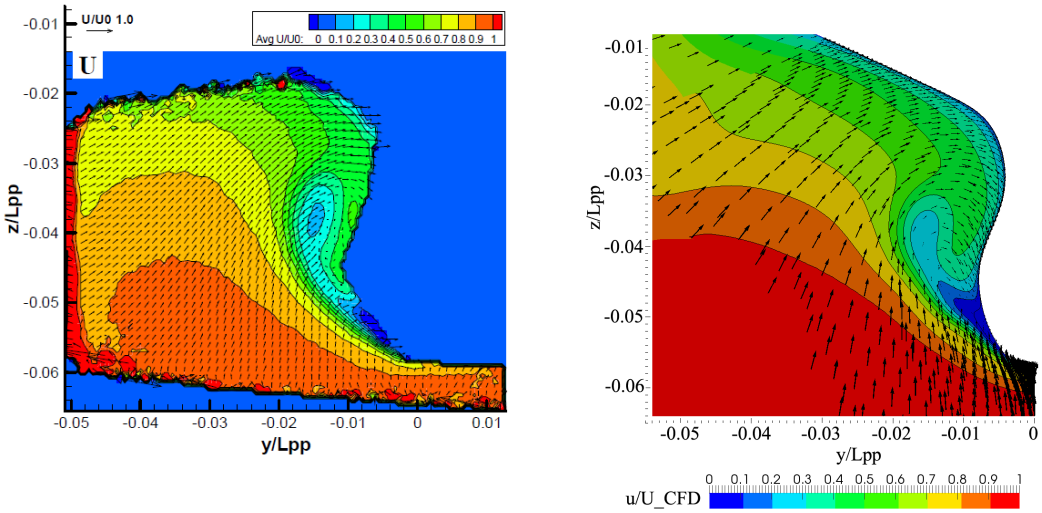

(a) Isowake contours of the JBC without ESD from EFD

(b) Isowake contours of the JBC without ESD from CFD

Figure 4.49: EFD-CFD-Comparison for isowake contours at $x/L_{PP} = 0.96250$ for the JBC bare hull

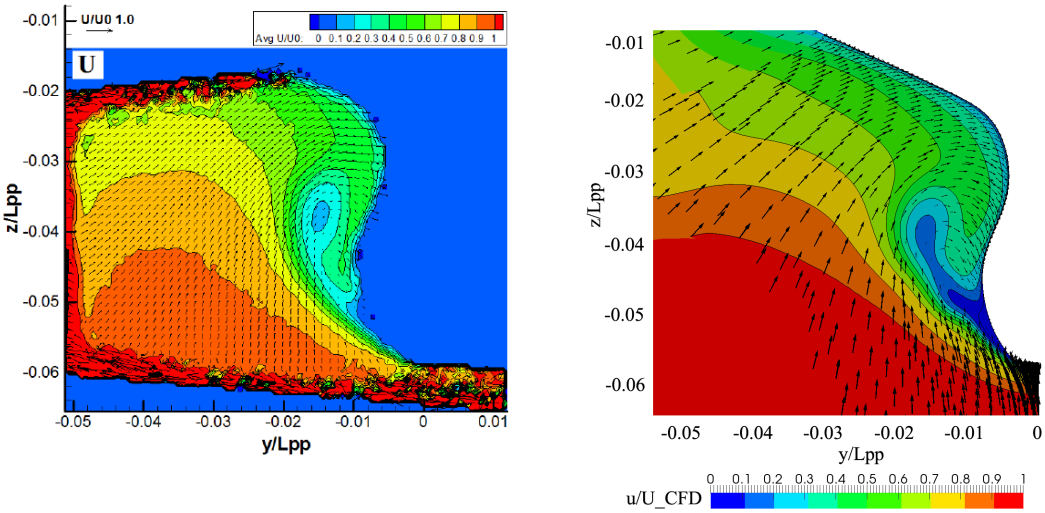

(a) Isowake contours of the JBC with ESD from EFD

(b) Isowake contours of the JBC with ESD from CFD

Figure 4.50: EFD-CFD-Comparison for isowake contours at $x/L_{PP} = 0.96250$ for the JBC hull with ESD

4.4.2.2 Cross Section $x/L_{PP} = 0.98428$

As shown on in Figure 3.8, this cross section is situated at the gap between the propeller and the ESD. Figure 4.51 shows the isowake contours for the bare hull. As seen in Figure 4.51b, the region of the lower side of the boss slightly differs and lower velocities propagates through sideways. There seems like a small scale vortex, which has a counterclockwise rotation, causing such phenomenon. Other

observation is that the computed wake is slightly higher than EFD measurements in general.

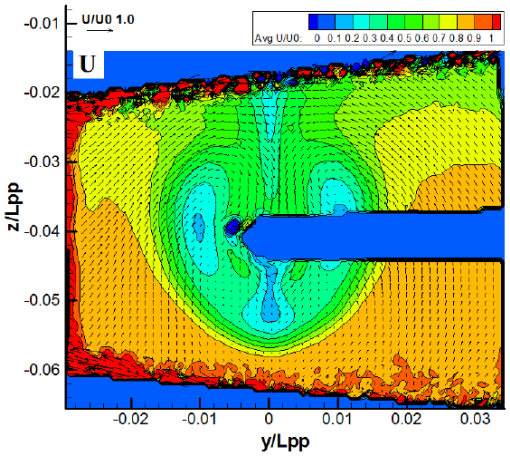

(a) Isowake contours of the JBC without ESD from EFD

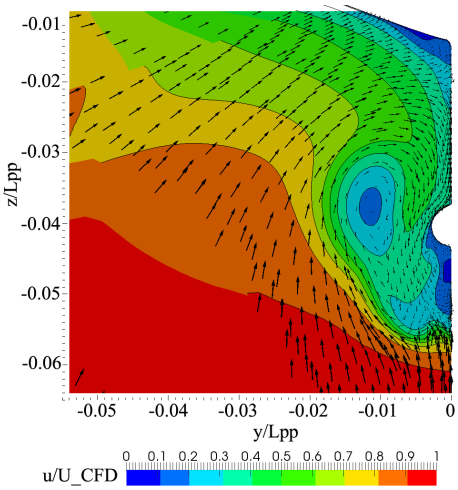

(b) Isowake contours of the JBC without ESD from CFD

Figure 4.51: EFD-CFD-Comparison for isowake contours at $x/L_{PP} = 0.98428$ for the JBC bare hull

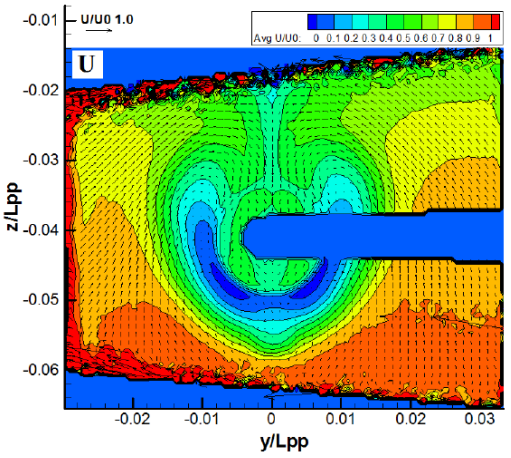

(a) Isowake contours of the JBC with ESD from EFD

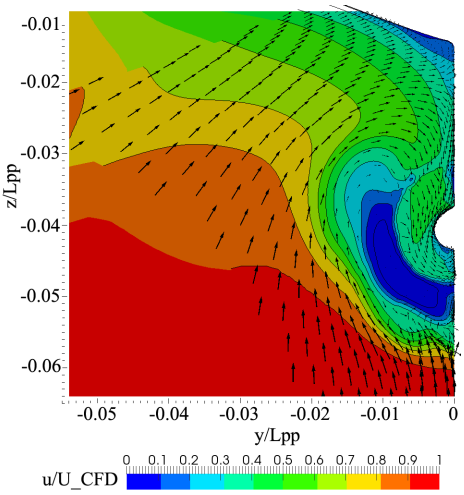

(b) Isowake contours of the JBC with ESD from CFD

Figure 4.52: EFD-CFD-Comparison for isowake contours at $x/L_{PP} = 0.98428$ for the JBC hull with ESD

Contours of velocity component w are presented in Figure 4.53 and Figure 4.54 for bare hull and hull with ESD respectively. Note that the discontinuities of contours in CFD computation plots are due to the refinement. The region that is close the hull has two times denser grid in all directions. It can be concluded that w contours correspond to the EFD measurements and the effect of the ESD is well captured.

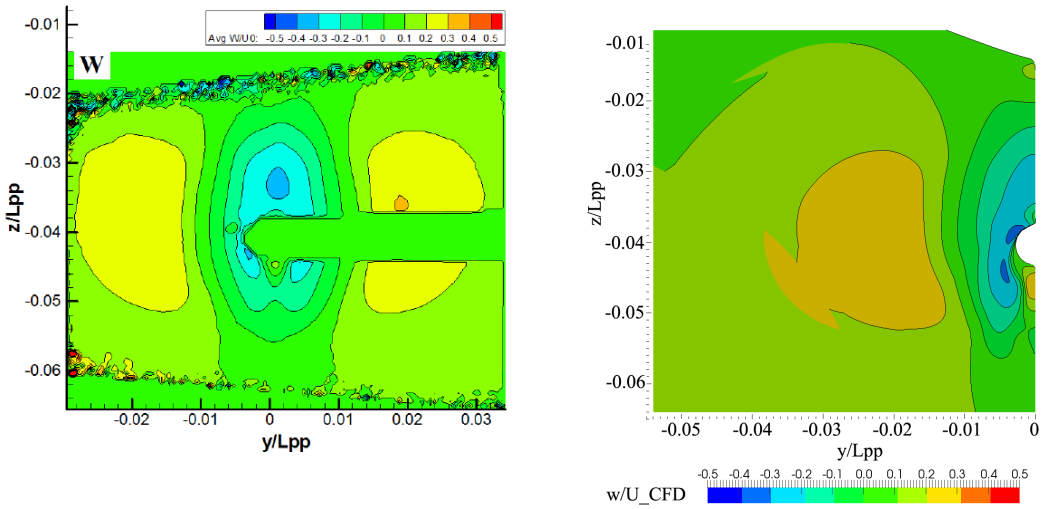

(a) w/U contours of the JBC without ESD from EFD

(b) w/U contours of the JBC without ESD from CFD

Figure 4.53: EFD-CFD-Comparison for w/U contours at $x/L_{PP} = 0.98428$ for the JBC bare hull

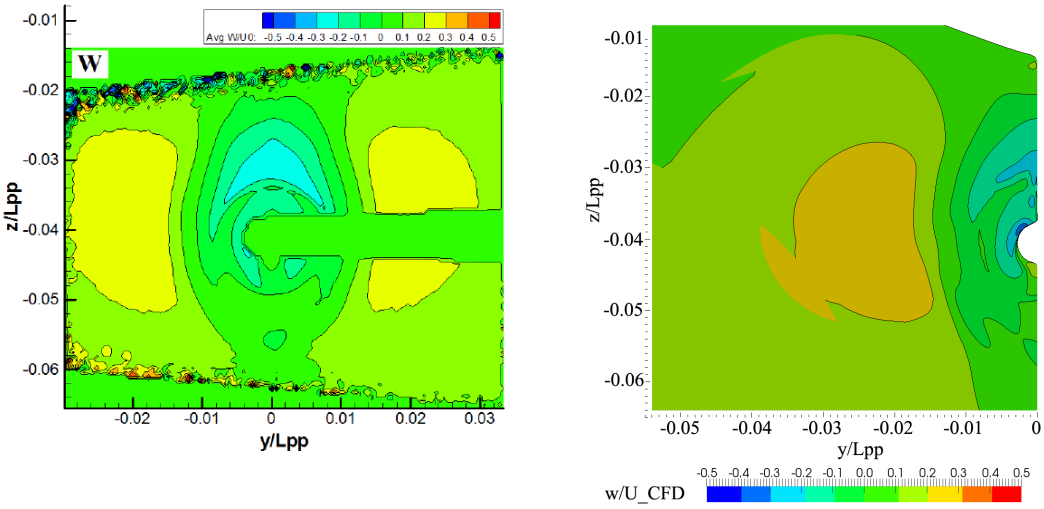

(a) w/U contours of the JBC with ESD from EFD

(b) w/U contours of the JBC with ESD from CFD

Figure 4.54: EFD-CFD-Comparison for w/U contours at $x/L_{PP} = 0.98428$ for the JBC hull with ESD

Due to lack of experimental data for turbulent kinetic energy, only a comparison between hull with and without ESD is possible. Figure 4.55 shows the k contours at the gap between the propeller and the duct. In Figure 4.55b, k values are smaller in general, especially a circular region is having almost zero turbulent kinetic energy. Having checked the isowake contours, this region corresponds to the separation point where the axial component of velocity u is zero.

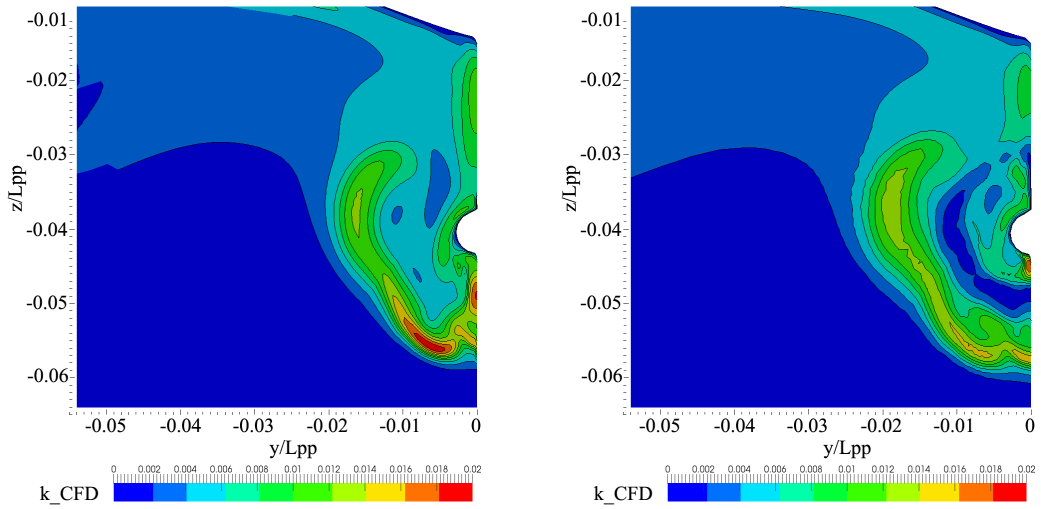

(a) k contours of the JBC without ESD

(b) k contours of the JBC with ESD

Figure 4.55: Comparison for computed turbulent kinetic energy contours at $x/L_{PP} = 0.98428$ for the JBC bare hull with and without ESD

4.4.2.3 Cross Section $x/L_{PP} = 1$

The cross section situated at the A.P is investigated through a comparison between hull with and without ESD due to lack of experimental data. Figure 4.56 shows isowake contours. Even though there are some lower velocity regions in hull with ESD, in general there is not much of a difference. It seems that effect of the duct on the vortex system is very limited since there is a noticeable similarity between cross flow vectors and wake around $y/L_{PP} = -0.01$ and $z/L_{PP} = -0.035$.

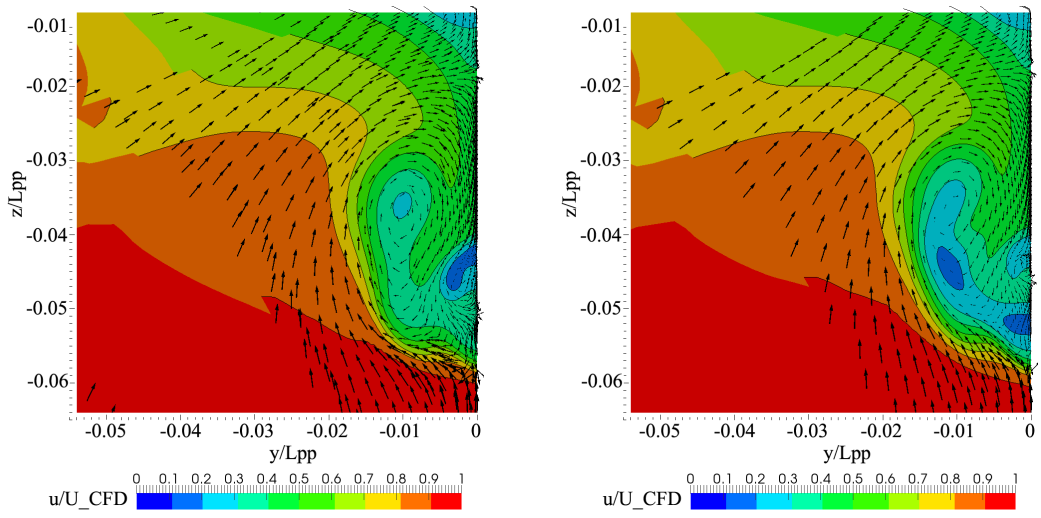

(a) Isowake contours of the JBC without ESD

(b) Isowake contours of the JBC with ESD

Figure 4.56: Comparison for isowake contours at $x/L_{PP} = 1$ for the JBC with and without ESD

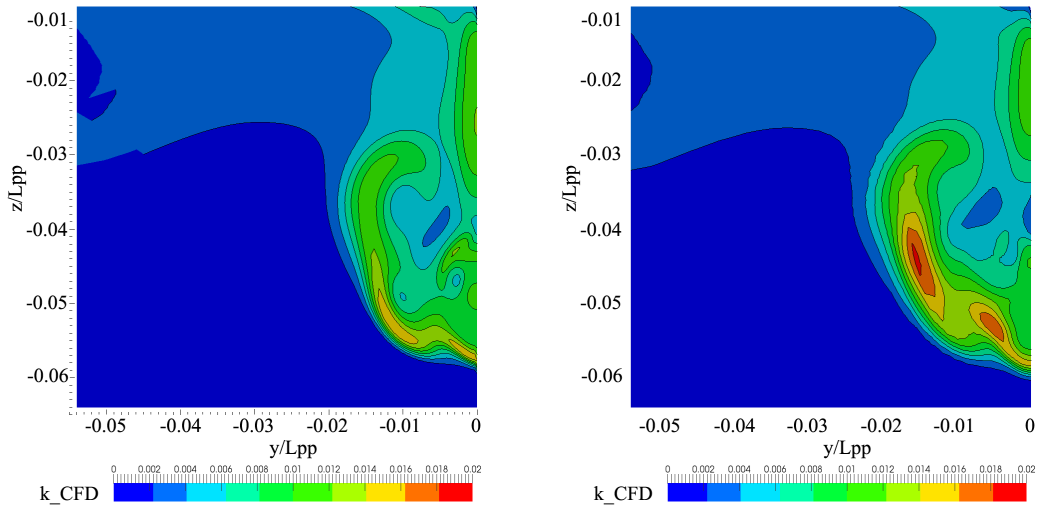

(a) k contours of the JBC without ESD

(b) k contours of the JBC with ESD

Figure 4.57: Comparison for computed turbulent kinetic energy contours at $x/L_{PP} = 1$ for the JBC bare hull with and without ESD

4.4.2.4 Velocity Profiles and Cross-flow Vectors at ($x/L_{PP} = 0.98428$, $z/L_{PP} = -0.03700$)

Due to the lack of experimental data, a comparison of velocity profiles and turbulent kinetic energy between the hull with and without ESD is performed. As presented in Table 3.5, cross section at $x/L_{PP} = 0.98428$ corresponds to the gap between propeller and duct. Except the region from the centre plane to the alignment of the duct, there is not much of a difference in terms of velocity components u, v and w. However velocity components and turbulent kinetic energy differ noticeably up until $y/L_{PP} = 0.02$ due to the effect of the ESD.

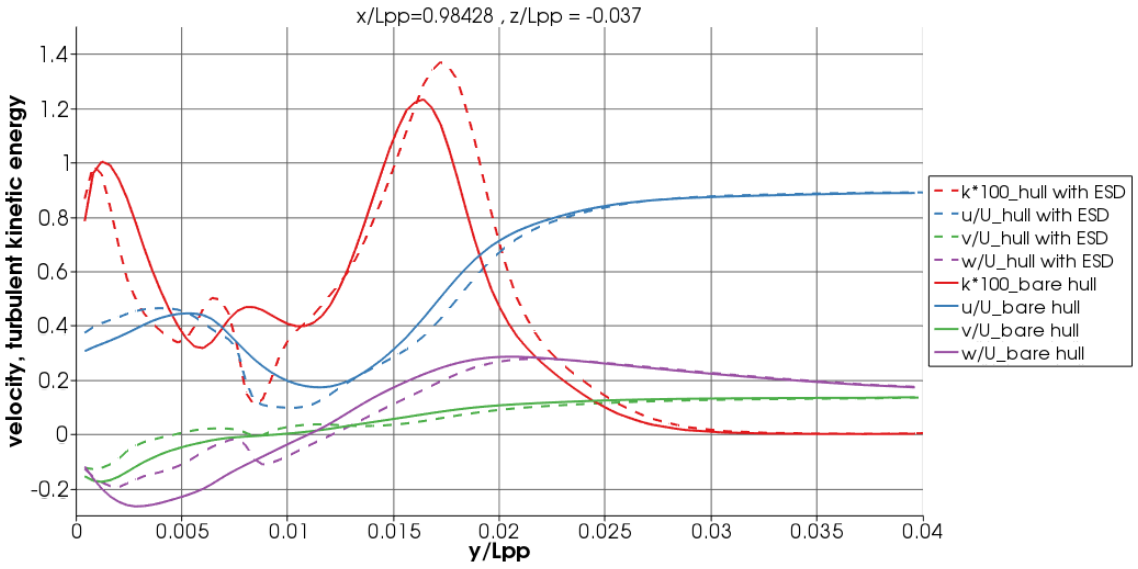

Figure 4.58: Appendages of JBC

4.4.3 Limiting Wall Streamlines

Showing the flow direction on the hull is possible with limiting streamlines. Since at the surface there is no flow on the hull due to the no-slip boundary condition, shear stress on the surface can be related to the limiting value of the flow (Lars Larsson and Hoyte C. Raven, 2010). Figure 4.59 shows the limiting streamlines while hull is coloured with the pressure coefficient C_P. There is no significant difference between the hull with and without ESD at the far upstream of the duct. However at the upper region of the ESD, a slightly higher pressured region is observed. In the region close the the duct, minor changes are observed.

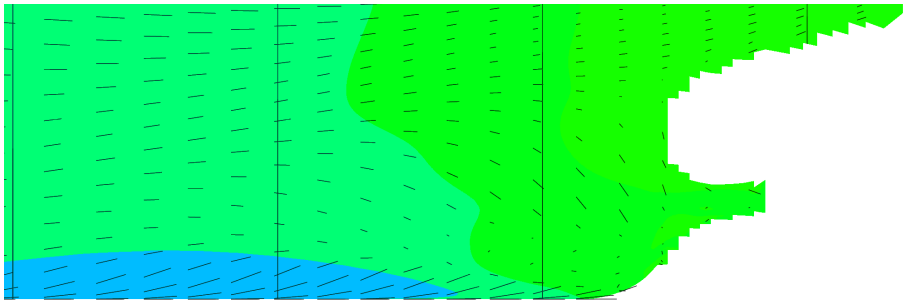

(a) Side view limiting streamlines at the stern region of the JBC bare hull

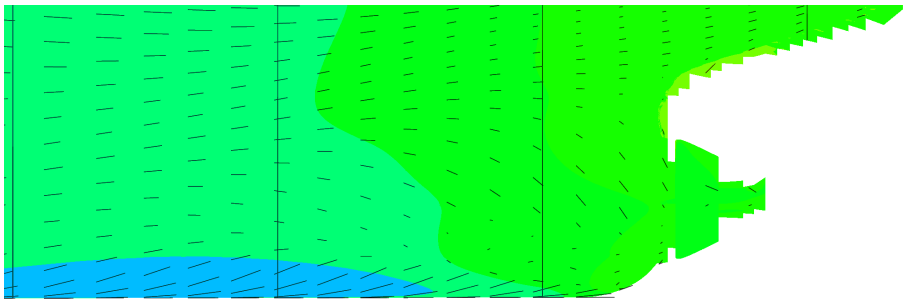

(b) Side view limiting streamlines at the stern region of the JBC hull with ESD

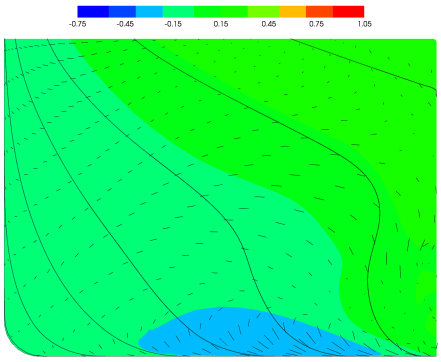

(c) Stern view limiting streamlines at the stern region of the JBC bare hull

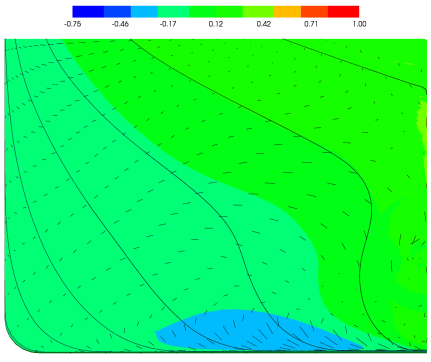

(d) Stern view limiting streamlines at the stern region of the JBC hull with ESD

Figure 4.59: Limiting streamlines at the stern region of the JBC

4.4.4 Q-Criterion

Q-Criterion is a method of vortex identification. According to Holmén (2012) Q-criterion identifies vortices as flow regions where second invariant of ∇U is positive. Characteristic equation of velocity gradient tensor

$$\lambda^3 + P\lambda^2 + Q\lambda + R = 0 \tag{4.3}$$

where P,Q and R are the invariants of the velocity gradient tensor. ∇U can be expressed as summation of strain-rate tensor $S_{ij} = \frac{1}{2}(\frac{\partial U_i}{\partial x_j} + \frac{\partial U_j}{\partial x_i})$ and vorticity tensor $\Omega_{ij} = \frac{1}{2}(\frac{\partial U_i}{\partial x_j} - \frac{\partial U_j}{\partial x_i})$

$$\nabla U = D_{ij} = S_{ij} + \Omega_{ij} \tag{4.4}$$

Using the decomposition into symmetric and anti-symmetric invariants of Equation 4.3, Q can be expressed as follows (Holmén, 2012)

$$Q = \frac{1}{2}(tr(\bar{D})^2 - tr(\bar{D})^2) = \frac{1}{2}||\bar{\Omega}||^2 - ||\bar{S}||^2 \tag{4.5}$$

Hence Q is a local measure of the local balance between shear strain-rate and vorticity magnitude. Condition of Q>0 indicates a flow region where rotation rate exceeds the strain rate. Additionally the pressure is required to be lower than the ambient pressure in the vortex.

Different Q values such as 50,500 and 2000 are used for visualising the vortex for simulation Case 1.3a(NMRI) and Case 1.4a(NMRI). The region where the selected Q value is matched, iso-surfaces are created and coloured with pressure coefficient C_P.

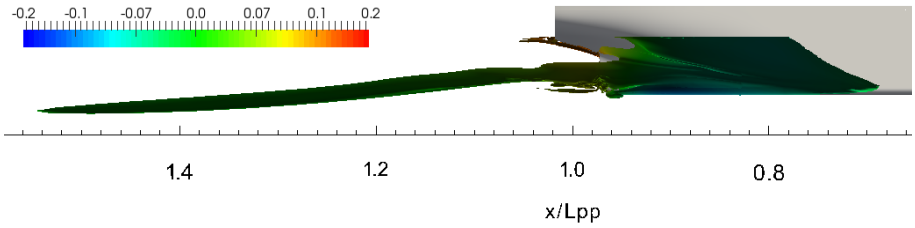

(a) Side view of the JBC bare hull for Q-Criterion (Q=50)

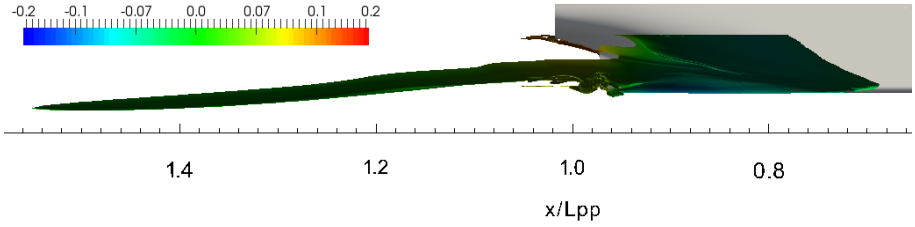

(b) Side view of the JBC hull with ESD for Q-Criterion (Q=50)

Figure 4.60: Side view of the JBC for Q-Criterion (Q=50)

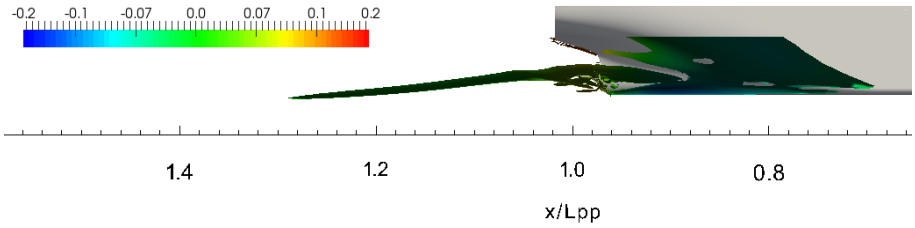

(a) Side view of the JBC bare hull for Q-Criterion (Q=500)

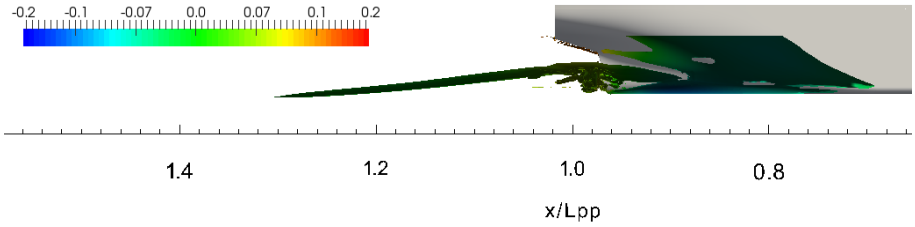

(b) Side view of the JBC hull with ESD for Q-Criterion (Q=500)

Figure 4.61: Side view of the JBC for Q-Criterion (Q=500)

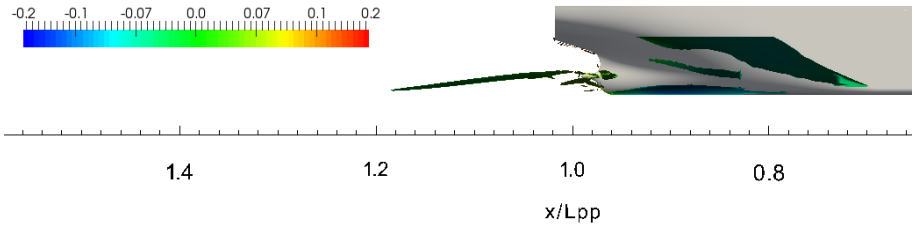

(a) Side view of the JBC bare hull for Q-Criterion (Q=2000)

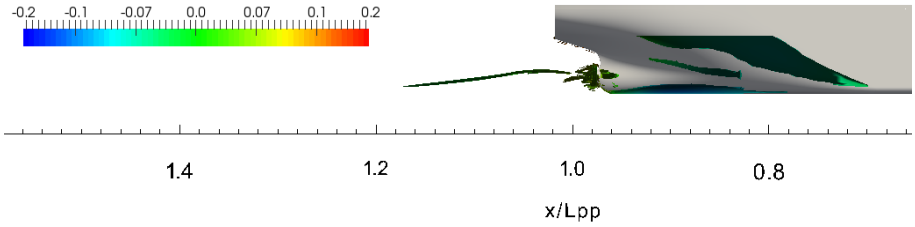

(b) Side view of the JBC hull with ESD for Q-Criterion (Q=2000)

Figure 4.62: Side view of the JBC for Q-Criterion (Q=2000)

Figure 4.60 shows the Q-criterion at $Q = 50$. Except the regions close to the ESD, there is no significant difference between hull with and without ESD. When Q value is increased to 500, the vortex system that continues towards down-flow gets smaller. However there is a rather small change at the aft shoulder as can be seen in Figure 4.61. If Q value is further increased to 2000, it is observed that the vortex system which continues downflow is actually detached from the hull and vortex systems at the aft shoulders declined noticeably. As seen from Figure 4.62, even though the detached vortex system is rather smaller at the hull with ESD, there is an additional vortex system around the duct compared to bare hull. Figure 4.63 shows that vortex density around the aft bulb is significantly higher at the hull with ESD.

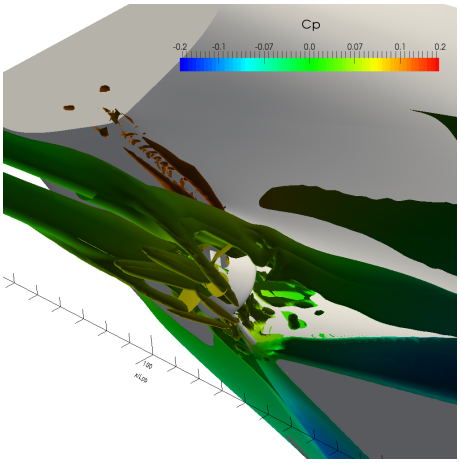

(a) Perspective view of the JBC bare hull for Q-Criterion (Q=500)

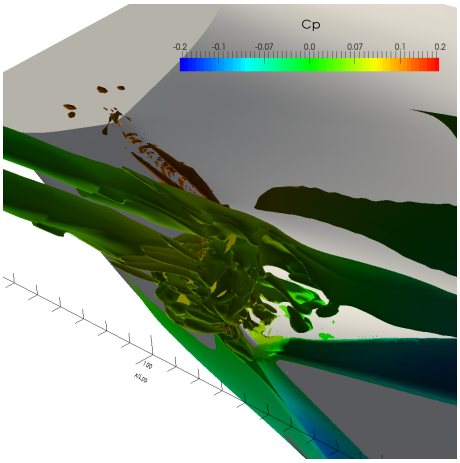

(b) Perspective view of the JBC hull with ESD for Q-Criterion (Q=500)

Figure 4.63: Perspective view of the JBC for Q-Criterion (Q=500)

4.5 Comparison Between Hull with and without ESD

Grid dependence studies were performed and presented for resistance, POW and self propulsion tests. Therefore, there is sufficient data for calculating the delivered power which is the most important outcome of all these tests. Comparing the propulsive factors such as thrust coefficient, effective (mean) wake fraction, relative rotative efficiency, etc. between EFD measurements and CFD predictions is thought to help understanding the error sources of K_T, K_Q and n. Finest grids of all grid dependence studies are used for this investigation. Resistance and propulsive predictions are presented in Table 4.33 as comparison errors $E\%D = (D - S)/D \times 100$ where D is measured values and S.

As presented in Table 4.33, it can be concluded that $E\%D$ of resistance and thrust predictions are rather small for both cases; the hull with and without ESD. Hence thrust deduction factor is predicted with a reasonable accuracy. However axial flow velocity V_{AT} under-predicted with and $E\%D$ of 11.8% to 15.8%. As shown in Figure 4.51 and Figure 4.52, especially for the local flow predictions of hull with ESD, it was observed that axial velocities were lower compared to EFD measurements. As follows, effective wake fraction w_{TM} and hull efficiency η_H is over-predicted due to the error of V_{AT}.

Table 4.33: Comparison errors of resistance and propulsion predictions for JBC with and without ESD

	$E\%D$ of hull without ESD		$E\%D$ of hull with ESD	
	Grid 1 & Refinement1	Grid 1 & Refinement3	Grid 1 & Refinement1	Grid 1 & Refinement3
R	0.8	0.8	0.3	0.3
T	1.6	1.6	0.4	0.9
Q	5.5	5.5	5.5	6.0
t	0.2	0.2	-0.9	1.1
J_{TM}	9.4	9.4	12.9	13.5
w_{TM}	-14.5	-14.5	-13.6	-14.6
V_{AT}	11.8	11.8	14.8	15.8
η_H	-13.3	-13.3	-17.1	-19.0
η_O	5.9	5.9	9.5	10.1
η_R	0.1	0.1	-0.6	-0.6
η_D	-6.6	-6.6	-6.6	-7.7
P_E	0.8	0.8	0.3	0.3
P_D	6.9	6.9	6.5	7.4

From thrust identity, J_{TM} is read from the POW results. Similar as V_{AT}, J_{TM} is under-predicted with a big comparison error, meaning that propeller efficiency η_O is also under-predicted. Note that having a lower effective wake fraction, cause a lower propeller efficiency η_O, but on the other hand higher hull efficiency η_H. Since they are multiplied by each other and with relative rotative efficiency η_R in order to calculate the propulsive efficiency η_D, η_O and η_H cancels each other to up to some degree. As a result propulsive efficiency η_D tends to be more reasonable.

The argument brought up in POW and self propulsion investigations was that K_T and K_Q are predicted with high errors because of n, since K_T and K_Q are nondimensionalized by n. This argument is justified with the current investigation. As presented in Table 4.33, thrust values are predicted with rather small $E\%D$ but not the n. When K_T is nondimensionalized, n^2 is in the denominator; causing K_T and n to be inversely proportional. This behaviour is clearly observed for both hull with ESD and without ESD. Similar conclusion can be made for computed K_Q values. Even though torque is under-predicted by 5.5% to 6.0%, $E\%D$ of torque coefficient is between 0.3% and $1,2\%$. Because when Q is non-nondimensionalized under-predicted n makes the $E\%D$ of K_Q smaller. Moreover, n is expected to be under-predicted because of the lower axial velocities coming to the propeller as discussed earlier.

Table 4.34 shows the delivered power reductions as difference of hull with and without ESD in percent of hull without ESD. Despite the $E\%D$ of 6.5% to 7.5% in P_D predictions for hull with and without ESD, the trend for reduction of P_D is captured quite well for both of the grids.

Table 4.34: Delivered power reductions as difference of hull with and without ESD in percent

	EFD	Grid 1 & Refinement1	Grid 1 & Refinement3
P_D reduction %	6.87	6.45	6.89

5
Conclusion and Future Work

5.1 Conclusions

In this thesis work, CFD has been used for a series of systematic and comprehensive predictions for resistance, POW and self propulsion tests. Computations were performed using SHIPFLOW code, potential flow method, lifting line method and RANS method with EASM turbulence model. In order to assess the numerical and modelling errors, verification and validation studies were performed. Addition to grid dependence studies, extensive investigations were performed to find the best settings for POW and self propulsion tests in SHIPFLOW Code. In order to make the conclusions more distinct, different stages of the thesis work have been listed in separate items.

Resistance, Sinkage & Trim

1. Wave resistance, sinkage and trim were computed by potential flow solver XPAN while ESD is disregarded. Comparison between the hull with and without ESD has only 1% difference in sinkage and trim in EFD data (provided by NMRI). Therefore disregarding the ESD in CFD computations is thought to be fair. Comparison error $E\%D$ for sinkage is -1% however prediction of trim is 20%. It is thought that, the high error in prediction of trim is due to flow separations which is not possible to capture by potential flow.

2. Grid dependence study for viscous resistance have been performed for bare hull and hull with ESD. Monotonic convergence is obtained according to LSR method for all resistance components C_F, C_{PV}, C_V and C_T.

3. Bare hull and and hull with ESD convergence tendencies for C_F, C_{PV}, C_V and C_T are observed to be higher than the theoretical order.

4. Comparison error of total resistance for bare hull and and hull with ESD are 0.8% and 0.3% which is quite accurate.

POW

1. Default POW test settings in SHIPFLOW needs to be improved. The grid dependence study showed the fluid domain is too coarse which gives a poor interaction between fluid domain grid and propeller grid.

2. One must be aware of the error of between the active and passive forces in x-direction. This error is inevitable due to interpolation between overlapping grids, however if fluid domain is fine enough $A\%P$ become negligible.

3. When the length of cylindrical propeller grid is reduced, the risk of having high error $A\%P$ increases significantly. Therefore, an extra care is required if shorter length of the propeller grid than default value is used.

Self Propulsion

1. In order to investigate the effect of the rake of the propeller and interaction between the grids, fluid domain grid, propeller grid and its axial position was varied.

   (a) Except the default propeller grid (Prop 2) with default fluid domain grid (Grid 4), all other variations showed poor interpolation.

   (b) Smallest comparison error for total resistance in self propulsion is observed at x_2 which is the axial position at the intersection point of generator line and $0.7\times$ the radius of the propeller. Therefore grid converge studies were performed at this axial position.

2. For finding the sufficient grid density of fluid domain grid around the propeller grid, systematic refinements were applied to the fluid domain grid (Grid 3) while propeller grid and its axial position was varied.

   (a) It is observed that when the grid density around the propeller grid is increased one step more, there is no need for increasing the refinement region far downstream. A refinement region that covers the propeller grid with a safe distance can provide the same results.

   (b) Likewise, when the refinement region covering the propeller grid is used for one more step increased of refinement, $A\%P$ values become very small indicating a good interpolation except the slimmest propeller grid (Prop 4).

3. Grid dependence study for self propulsion has been carried out for hull with and without ESD and two different refinements each.

   (a) Monotonic convergence is obtained according to LSR method for resistance and propulsive factors K_T, K_Q, n and C_T.

   (b) Bare hull and and hull with ESD convergence tendencies of grids with Refinement 1 are observed to be much higher than the grids with Refinement 3. It is shown that Refinement 1 cannot provide sufficient nodes for a good interpolation therefore in coarse grids there is an significant variation. Refinement 3 on the other hand eliminates the $A\%P$ more effectively, causing a much less grid dependent behaviour and small observed order of accuracies.

4. Comparison errors of self propulsion are thought to be within acceptable limits.

Local Flow Prediction

1. Even though there is a general agreement between EFD and CFD, the wake is over-predicted especially for the hull with ESD at the gap between the propeller and duct.

2. v and w contours shows a good agreement with all measurement planes

3. At the measurement plane SS 3/8, separation is observed in hull with and without ESD for CFD predictions. However in EFD measurements for only hull without ESD, exhibited separation at the lower part of the gondola. It is obvious that EFD measurements for this section are unclear close to hull. Therefore more consistent measurement data is needed.

5.2 Future Work

In this thesis work, main focus was placed on prediction of resistance and propulsive factors with numerical computations. Even though resistance predictions were very accurate, it is hard to conclude the same for self propulsion tests. Some sources of numerical errors and modelling errors have been addressed.

All viscous simulations have been carried out with double model which is based on the assumption that effects of the free surface are limited. However it may not be the case. Hence, VOF simulations may help understanding weather this assumption is valid or not. Since potential flow solver was not able to calculate the flow for hull with ESD, ESD was disregarded in potential flow simulations. VOF simulations will enable the calculations of the sinkage and trim for hull with ESD too.

Investigations on settings of self propulsion test in SHIPFLOW have been performed for only one speed. Therefore having the same tests with different speeds will strengthen the findings if they are valid.

Comparison between EFD measurements and CFD predictions for hull with and without ESD for delivered power revealed that effective (mean) wake fraction is considerably higher in CFD predictions. Although the EASM turbulence model which was used for all viscous simulations is an advanced model, $k-\omega\ SST$ turbulence model can be used for checking if it provides more reasonable propulsive factors. Another possibility in SHIPFLOW is to run the simulations with zonal approach instead of global.

Local flow predictions can be investigated more thoroughly if more consistent and clear EFD data is provided for mean flow and turbulent quantities.

References

Broberg, L., & Orych, M. (2012). An Efficient Numerical Technique to Simulate the Propeller Hull Interaction. *International Journal of Innovative Research & Development*, *14*.

Broberg, L., Regnström, B., & Östberg, M. (2007). XCHAP Theoretical Manual [Computer software manual]. FLOWTECH International AB, Gothenburg, Sweden.

Broberg, L., Regnström, B., & Östberg, M. (2014). SHIPFLOW Users Manual [Computer software manual]. FLOWTECH International AB, Gothenburg, Sweden.

Holmén, V. (2012). *Methods for Vortex Identification* (Master's Thesis). Faculty Technology, Mathematics, Lund University, Lund.

Kim, K., Leer-Andersen, M., & Orych, M. (2014). Hydrodynamic Optimization of Energy Saving Devices in Full Scale. In 30^{th} *Symposium on Naval Hydrodynamics.* Hobart, Tasmania, Australia.

Lars Larsson and Hoyte C. Raven. (2010). *Ship Resistance and Flow.* Jersey City, New Jersey: The Society of Naval Architects and Marine Engineers.

Larsson, L., Stern, F., & Visonneau, M. (2014). *Numerical Ship Hydrodynamics, An Assessment of the Gothenburg 2010 Workshop.* Dordrecht: Springer.

NMRI. (2015). *Tokyo 2015 A Workshop on CFD in Ship Hydrodynamics.* Retrieved from `http://www.t2015.nmri.go.jp/`

Regnström, B. (2008). Introduction to Overlapping Grids in SHIPFLOW [Computer software manual]. FLOWTECH International AB, Gothenburg, Sweden.

Schneekluth, H., & Bertram, V. (1998). *Ship Fesign for Efficiency and Economy* (2^{nd} ed.). Linacre House, Jordan Hill, Oxford: Butterworth-Heinemann.

Versteeg, H. K., & Malalasekera, W. (2007). *An Introduction to Computational Fluid Dynamics* (2^{nd} ed.). Harlow, Essex CM20 2JE, England: Pearson Education Limited.

Zhang, D. (1990). *Numerical Computation of Ship Stern/Propeller Flow* (Doctoral dissertation). Department of Shipping and Marine Technology, Chalmers University of Technology, Gothenburg.

Zou, L. (2012). *CFD Predictions Including Verification and Validation of Hydrodynamic Forces and Moments on Ship in Restricted Waters* (Doctoral dissertation). Department of Shipping and Marine Technology, Chalmers University of Technology, Gothenburg.

Zou, L., & Larsson, L. (2014). CFD Verification and Validation in Practice - A Study Based on Resistance Submission to the Gothenburg 2010 Workshop on Numerical Ship Hydrodynamics. In 30^{th} *Symposium on Naval Hydrodynamics.* Hobart, Tasmania, Australia.

A

Appendix : Grid Dependence Study for Resistance

Table A.1: EFD results for C_T, sinkage and trim

	EFD Results from NMRI		
	$C_T \times 10^3$	sinkage [% L_{PP}] upward positive	trim [% L_{PP}] bow up positive
Bare hull	4.289	-0.086	-0.180
Hull with ESD	4.263	-0.085	-0.182

Table A.2: Computed C_F, C_{PV}, C_V and C_T values for Case1.1(NMRI)

	Case 1.1a(NMRI)			
	$C_F \times 10^3$	$C_{PV} \times 10^3$	$C_V \times 10^3$	$C_T \times 10^3$
Grid 1	3.099	1.002	4.102	4.254
Grid 2	3.065	1.019	4.093	4.246
Grid 3	3.071	1.020	4.091	4.244
Grid 4	3.029	1.063	4.091	4.244
Grid 5	2.967	1.108	4.076	4.229

Table A.3: Computed C_F, C_{PV}, C_V and C_T values for Case1.2(NMRI)

	Case 1.2a(NMRI)			
	$C_F \times 10^3$	$C_{PV} \times 10^3$	$C_V \times 10^3$	$C_T \times 10^3$
Grid 1	3.091	1.006	4.097	4.250
Grid 2	3.079	1.016	4.096	4.249
Grid 3	3.064	1.016	4.080	4.232
Grid 4	3.021	1.054	4.075	4.227
Grid 5	2.960	1.093	4.055	4.207

B
Appendix : POW Simulations

Table B.1: POW EFD measurements for K_T, $10K_Q$ and η_o (NMRI, 2015)

J	K_T	$10K_Q$	η_o
0.1	0.3267	0.3748	0.1387
0.15	0.3112	0.3629	0.2047
0.2	0.2949	0.35	0.2681
0.25	0.2777	0.3361	0.3288
0.3	0.2598	0.321	0.3864
0.35	0.241	0.3047	0.4406
0.4	0.2214	0.2871	0.4909
0.45	0.201	0.2682	0.5367
0.5	0.1798	0.2479	0.5771
0.55	0.1577	0.2261	0.6107
0.6	0.1349	0.2027	0.6354
0.65	0.1112	0.1777	0.6475
0.7	0.0867	0.1509	0.64
0.75	0.0614	0.1224	0.5986
0.8	0.0353	0.0921	0.4879

Table B.2: Computed K_T, $10K_Q$, F_A, F_P and errors for POW Prop 1 ($J = 0.6$)

Grid No.	K_T	$10K_Q$	F_A	F_P	$A\%P$	$E\%D, KT$	$E\%D, KQ$
Grid 1	0.1298	0.1947	0.3622	0.3615	0.19	3.77	3.93
Grid 2	0.1302	0.1951	0.3599	0.3609	-0.28	3.51	3.75
Grid 3	0.1316	0.1966	0.3569	0.3655	-2.41	2.43	2.99
Grid 4	0.1337	0.1987	0.3547	0.3717	-4.79	0.91	1.96
Grid 5	0.1259	0.1906	0.3681	0.3495	5.07	6.70	5.96

Table B.3: Iterative convergence data for K_T and K_Q for POW Prop 1 ($J = 0.6$)

iterations	K_T	$10K_Q$	F_A	F_P	$A\%P$	$E\%D, KT$	$E\%D, KQ$
500	0.1298	0.1947	0.3622	0.3615	0.19	3.77	3.93
1000	0.1299	0.1948	0.3607	0.3600	0.19	3.74	3.91
1500	0.1298	0.1947	0.3611	0.3604	0.19	3.78	3.93
2000	0.1298	0.1947	0.3613	0.3606	0.19	3.77	3.93

Table B.4: POW CFD computations for Prop 1, Grid 1

J	K_T	$10K_Q$	η_o	$E\%D, KT$	$E\%D, KQ$	$E\%D, \eta_o$
0.3	0.2510	0.3030	0.3956	3.38	5.62	-2.38
0.4	0.3030	0.2739	0.5005	2.73	4.58	-1.95
0.5	0.3956	0.2382	0.5851	2.59	3.90	-1.38
0.6	0.2154	0.1947	0.6366	3.77	3.93	-0.18
0.7	0.2739	0.1442	0.6226	7.08	4.47	2.72
0.75	0.5005	0.1154	0.5599	11.83	5.70	6.47
0.8	0.1751	0.0843	0.4054	23.93	8.44	16.90

Table B.5: POW CFD computations for Prop 1, Grid 5

J	K_T	$10K_Q$	η_o	$E\%D, KT$	$E\%D, KQ$	$E\%D, \eta_o$
0.3	0.2433	0.2959	0.3925	6.36	7.81	-1.58
0.4	0.2085	0.2673	0.4964	5.85	6.89	-1.13
0.5	0.1693	0.2324	0.5798	5.82	6.24	-0.46
0.6	0.1259	0.1906	0.6306	6.70	5.96	0.76
0.7	0.0779	0.1412	0.6146	10.13	6.41	3.97
0.75	0.0524	0.1134	0.5520	14.61	7.37	7.79
0.8	0.0263	0.0834	0.4011	25.60	9.49	17.78

Table B.6: POW CFD computations for Prop 2, Grid 1

J	K_T	$10K_Q$	η_o	$E\%D, KT$	$E\%D, KQ$	$E\%D, \eta_o$
0.3	0.2759	0.3255	0.4047	-6.19	-1.40	-4.73
0.4	0.2352	0.2930	0.5112	-6.25	-2.04	-4.13
0.5	0.1906	0.2538	0.5975	-5.98	-2.37	-3.54
0.6	0.1412	0.2069	0.6517	-4.69	-2.09	-2.57
0.7	0.0873	0.1519	0.6407	-0.73	-0.64	-0.10
0.75	0.0588	0.1210	0.5807	4.16	1.18	2.99
0.8	0.0295	0.0876	0.4286	16.45	4.87	12.15

Table B.7: POW CFD computations for Prop 2, Grid 5

J	K_T	$10K_Q$	η_o	$E\%D, KT$	$E\%D, KQ$	$E\%D, \eta_o$
0.3	0.2671	0.3176	0.4016	-2.81	1.07	-3.93
0.4	0.2277	0.2857	0.5073	-2.83	0.48	-3.33
0.5	0.1841	0.2474	0.5922	-2.39	0.20	-2.61
0.6	0.1364	0.2019	0.6450	-1.08	0.41	-1.52
0.7	0.0843	0.1485	0.6324	2.75	1.57	1.18
0.75	0.0569	0.1186	0.5722	7.39	3.10	4.40
0.8	0.0287	0.0864	0.4231	18.62	6.14	13.28

Table B.8: POW CFD computations for Prop 3, Grid 1

J	K_T	$10K_Q$	η_o	$E\%D, KT$	$E\%D, KQ$	$E\%D, \eta_o$
0.3	0.2766	0.3265	0.4044	-6.45	-1.71	-4.67
0.4	0.2361	0.2940	0.5113	-6.64	-2.39	-4.16
0.5	0.1914	0.2547	0.5980	-6.47	-2.75	-3.62
0.6	0.1420	0.2078	0.6526	-5.24	-2.50	-2.70
0.7	0.0879	0.1525	0.6419	-1.33	-1.04	-0.30
0.75	0.0592	0.1214	0.5822	3.56	0.81	2.74
0.8	0.0297	0.0879	0.4302	15.86	4.56	11.82

Table B.9: POW CFD computations for Prop 3, Grid 5

J	K_T	$10K_Q$	η_o	$E\%D, KT$	$E\%D, KQ$	$E\%D, \eta_o$
0.3	0.2760	0.3259	0.4043	-6.24	-1.54	-4.64
0.4	0.2360	0.2938	0.5113	-6.58	-2.34	-4.16
0.5	0.1912	0.2546	0.5976	-6.35	-2.71	-3.56
0.6	0.1420	0.2078	0.6522	-5.23	-2.54	-2.64
0.7	0.0880	0.1527	0.6420	-1.49	-1.19	-0.31
0.75	0.0595	0.1217	0.5834	3.11	0.56	2.53
0.8	0.0302	0.0883	0.4351	14.54	4.15	10.82

Table B.10: POW CFD computations for Prop 4, Grid 1

J	K_T	$10K_Q$	η_o	$E\%D, KT$	$E\%D, KQ$	$E\%D, \eta_o$
0.3	0.2555	0.3094	0.3944	1.64	3.62	-2.06
0.4	0.2186	0.2786	0.4995	1.28	2.97	-1.75
0.5	0.1774	0.2415	0.5846	1.32	2.57	-1.30
0.6	0.1317	0.1974	0.6372	2.38	2.63	-0.28
0.7	0.0815	0.1456	0.6236	6.03	3.54	2.57
0.75	0.0549	0.1165	0.5621	10.62	4.80	6.09
0.8	0.0275	0.0852	0.4101	22.22	7.46	15.94

Table B.11: POW CFD computations for Prop 4, Grid 5

J	K_T	$10K_Q$	η_o	$E\%D, KT$	$E\%D, KQ$	$E\%D, \eta_o$
0.3	0.2575	0.3103	0.3962	0.89	3.34	-2.54
0.4	0.2241	0.2825	0.5050	-1.24	1.59	-2.88
0.5	0.1839	0.2467	0.5932	-2.30	0.47	-2.79
0.6	0.1384	0.2034	0.6497	-2.60	-0.36	-2.25
0.7	0.0866	0.1507	0.6407	0.07	0.16	-0.11
0.75	0.0587	0.1203	0.5819	4.45	1.69	2.78
0.8	0.0295	0.0872	0.4308	16.46	5.36	11.70

C

Appendix : Variation of Propeller Axial Positions and Grids

Table C.1: Computed C_T and $E\%D$ values for Grid 2

	$C_T \times 10^3$			$E\%D$		
	Prop 4	Prop 3	Prop 2	Prop 4	Prop 3	Prop 2
x_1	4.795	4.759	4.773	0.34	1.08	0.78
x_2	4.787	4.785	4.785	0.51	0.55	0.55
x_3	4.695	4.735	4.743	2.41	1.58	1.42
x_4	4.767	4.763	4.764	0.91	0.99	0.97

Table C.2: Computed C_T and $E\%D$ values for Grid 3

	$C_T \times 10^3$			$E\%D$		
	Prop 4	Prop 3	Prop 2	Prop 4	Prop 3	Prop 2
x_1	4.881	4.830	4.751	-1.46	-0.40	1.25
x_2	4.543	4.698	4.755	5.56	2.35	1.16
x_3	4.855	4.809	4.729	-0.91	0.04	1.71
x_4	4.643	4.681	4.736	3.49	2.71	1.56

Table C.3: Computed C_T and $E\%D$ values for Grid 4

	$C_T \times 10^3$			$E\%D$		
	Prop 4	Prop 3	Prop 2	Prop 4	Prop 3	Prop 2
x_1	4.604	4.800	4.780	4.29	0.23	0.65
x_2	4.996	4.658	4.723	-3.85	3.17	1.84
x_3	4.599	4.771	4.736	4.40	0.82	1.56
x_4	4.592	4.777	4.741	4.55	0.72	1.46

Table C.4: Computed C_T and $E\%D$ values for Grid 5

	$C_T \times 10^3$			$E\%D$		
	Prop 4	Prop 3	Prop 2	Prop 4	Prop 3	Prop 2
x_1	4.787	4.677	4.802	0.51	2.79	0.19
x_2	4.667	4.737	4.686	3.00	1.54	2.60
x_3	4.717	4.807	4.665	1.94	0.08	3.05
x_4	4.669	4.656	4.747	2.96	3.21	1.33

Table C.5: Computed n and $E\%D$ values for Grid 2

	n			$E\%D$		
	Prop 4	Prop 3	Prop 2	Prop 4	Prop 3	Prop 2
x_1	7.99	7.37	7.30	-2.40	5.57	6.41
x_2	7.84	7.50	7.44	-0.47	3.87	4.66
x_3	7.24	7.25	7.26	7.17	7.05	6.97
x_4	7.80	7.48	7.43	0.06	4.15	4.74

Table C.6: Computed n and $E\%D$ values for Grid 3

	n			$E\%D$		
	Prop 4	Prop 3	Prop 2	Prop 4	Prop 3	Prop 2
x_1	8.19	7.72	7.29	-5.03	0.98	6.52
x_2	6.94	7.21	7.39	11.01	7.62	5.28
x_3	8.21	7.76	7.29	-5.27	0.46	6.50
x_4	7.34	7.11	7.31	5.84	8.90	6.31

Table C.7: Computed n and $E\%D$ values for Grid 4

	n			$E\%D$		
	Prop 4	Prop 3	Prop 2	Prop 4	Prop 3	Prop 2
x_1	7.15	7.52	7.42	8.40	3.59	4.88
x_2	8.79	7.09	7.15	-12.68	9.08	8.30
x_3	6.98	7.43	7.37	10.48	4.70	5.48
x_4	7.47	7.65	7.33	4.19	1.99	6.07

Table C.8: Computed n and $E\%D$ values for Grid 5

	n			$E\%D$		
	Prop 4	Prop 3	Prop 2	Prop 4	Prop 3	Prop 2
x_1	8.30	7.08	7.54	-6.37	9.21	3.29
x_2	7.50	7.60	7.02	3.88	2.52	10.00
x_3	8.10	7.69	7.04	-3.87	1.36	9.79
x_4	8.04	7.08	7.46	-3.07	9.29	4.38

Table C.9: Computed K_T and $E\%D$ values for Grid 2

	K_T			$E\%D$		
	Prop 4	Prop 3	Prop 2	Prop 4	Prop 3	Prop 2
x_1	0.207	0.240	0.245	4.8	-10.5	-13.0
x_2	0.214	0.233	0.237	1.5	-7.5	-9.3
x_3	0.242	0.245	0.246	-11.6	-12.9	-13.2
x_4	0.215	0.233	0.236	1.0	-7.5	-8.8

Table C.10: Computed K_T and $E\%D$ values for Grid 3

	K_T			$E\%D$		
	Prop 4	Prop 3	Prop 2	Prop 4	Prop 3	Prop 2
x_1	0.202	0.223	0.243	6.8	-2.9	-12.2
x_2	0.247	0.245	0.237	-13.9	-12.7	-9.4
x_3	0.200	0.220	0.241	8.0	-1.2	-11.0
x_4	0.230	0.250	0.241	-6.1	-15.1	-11.2

Table C.11: Computed K_T and $E\%D$ values for Grid 4

	K_T			$E\%D$		
	Prop 4	Prop 3	Prop 2	Prop 4	Prop 3	Prop 2
x_1	0.239	0.233	0.238	-10.3	-7.6	-9.6
x_2	0.184	0.249	0.250	15.4	-14.6	-15.1
x_3	0.250	0.236	0.236	-15.3	-8.6	-8.9
x_4	0.218	0.223	0.241	-0.4	-2.9	-11.0

Table C.12: Computed K_T and $E\%D$ values for Grid 5

	K_T			$E\%D$		
	Prop 4	Prop 3	Prop 2	Prop 4	Prop 3	Prop 2
x_1	0.191	0.251	0.232	12.1	-15.6	-6.9
x_2	0.223	0.223	0.256	-2.7	-2.6	-18.1
x_3	0.195	0.224	0.253	10.1	-3.0	-16.5
x_4	0.194	0.249	0.232	10.6	-14.9	-7.1

Table C.13: Computed K_Q and $E\%D$ values for Grid 2

	K_Q			$E\%D$		
	Prop 4	Prop 3	Prop 2	Prop 4	Prop 3	Prop 2
x_1	0.0260	0.0291	0.0296	6.72	-4.46	-6.04
x_2	0.0269	0.0286	0.0289	3.65	-2.52	-3.65
x_3	0.0296	0.0297	0.0297	-6.02	-6.38	-6.35
x_4	0.0270	0.0286	0.0289	3.08	-2.63	-3.46

Table C.14: Computed K_Q and $E\%D$ values for Grid 3

	K_Q			$E\%D$		
	Prop 4	Prop 3	Prop 2	Prop 4	Prop 3	Prop 2
x_1	0.0259	0.0277	0.0294	7.14	0.82	-5.39
x_2	0.0296	0.0295	0.0288	-6.09	-5.61	-3.23
x_3	0.0257	0.0273	0.0292	8.06	2.28	-4.73
x_4	0.0282	0.0301	0.0292	-1.10	-7.98	-4.59

Table C.15: Computed K_Q and $E\%D$ values for Grid 4

	K_Q			$E\%D$		
	Prop 4	Prop 3	Prop 2	Prop 4	Prop 3	Prop 2
x_1	0.0290	0.0287	0.0290	-4.01	-2.75	-3.80
x_2	0.0242	0.0300	0.0300	13.29	-7.35	-7.60
x_3	0.0301	0.0289	0.0288	-7.77	-3.67	-3.30
x_4	0.0270	0.0277	0.0293	3.13	0.61	-5.03

Table C.16: Computed K_Q and $E\%D$ values for Grid 5

	K_Q			$E\%D$		
	Prop 4	Prop 3	Prop 2	Prop 4	Prop 3	Prop 2
x_1	0.0246	0.0302	0.0284	11.93	-8.29	-1.93
x_2	0.0277	0.0276	0.0306	0.82	1.09	-9.69
x_3	0.0250	0.0278	0.0303	10.45	0.26	-8.51
x_4	0.0248	0.0301	0.0285	11.15	-8.00	-2.15

D

Appendix : Variation of Refinement Around the Propeller Grid

Table D.1: Computed C_T and $E\%D$ values for Refinement 2

	$C_T \times 10^3$			$E\%D$		
	Prop 4	Prop 3	Prop 2	Prop 4	Prop 3	Prop 2
x_1	4.827	4.771	4.789	-0.34	0.82	0.46
x_2	4.833	4.760	4.773	-0.45	1.06	0.78
x_3	4.812	4.755	4.768	-0.02	1.16	0.89
x_4	4.726	4.765	4.760	1.78	0.95	1.06

Table D.2: Computed C_T and $E\%D$ values for Refinement 3

	$C_T \times 10^3$			$E\%D$		
	Prop 4	Prop 3	Prop 2	Prop 4	Prop 3	Prop 2
x_1	4.795	4.740	4.756	0.34	1.48	1.14
x_2	4.799	4.727	4.741	0.25	1.75	1.46
x_3	4.779	4.722	4.735	0.67	1.86	1.58
x_4	4.692	4.732	4.728	2.47	1.65	1.73

Table D.3: Computed C_T and $E\%D$ values for Refinement 4

	$C_T \times 10^3$			$E\%D$		
	Prop 4	Prop 3	Prop 2	Prop 4	Prop 3	Prop 2
x_1	4.753	4.755	4.758	1.20	1.16	1.10
x_2	4.733	4.741	4.744	1.63	1.46	1.39
x_3	4.731	4.732	4.733	1.67	1.65	1.63
x_4	4.737	4.727	4.725	1.54	1.75	1.80

Table D.4: Computed n and $E\%D$ values for Refinement 2

	n			$E\%D$		
	Prop 4	Prop 3	Prop 2	Prop 4	Prop 3	Prop 2
x_1	7.65	7.30	7.32	1.92	6.43	6.15
x_2	7.69	7.29	7.31	1.36	6.55	6.32
x_3	7.68	7.32	7.33	1.52	6.13	6.01
x_4	7.33	7.41	7.33	6.05	5.06	5.99

Table D.5: Computed n and $E\%D$ values for Refinement 3

	n			$E\%D$		
	Prop 4	Prop 3	Prop 2	Prop 4	Prop 3	Prop 2
x_1	7.61	7.27	7.28	2.45	6.80	6.66
x_2	7.65	7.25	7.27	1.90	7.06	6.83
x_3	7.64	7.28	7.29	2.06	6.64	6.52
x_4	7.29	7.36	7.29	6.57	5.58	6.49

Table D.6: Computed n and $E\%D$ values for Refinement 4

	n			$E\%D$		
	Prop 4	Prop 3	Prop 2	Prop 4	Prop 3	Prop 2
x_1	7.39	7.31	7.27	5.31	6.34	6.81
x_2	7.33	7.33	7.28	5.96	6.06	6.66
x_3	7.38	7.31	7.28	5.32	6.25	6.70
x_4	7.44	7.34	7.28	4.63	5.87	6.71

Table D.7: Computed K_T and $E\%D$ values for Refinement 2

	K_T			$E\%D$		
	Prop 4	Prop 3	Prop 2	Prop 4	Prop 3	Prop 2
x_1	0.228	0.245	0.245	-5.0	-12.7	-13.1
x_2	0.226	0.245	0.245	-4.0	-12.8	-12.8
x_3	0.225	0.242	0.243	-3.6	-11.5	-11.8
x_4	0.239	0.238	0.242	-10.1	-9.5	-11.4

Table D.8: Computed K_T and $E\%D$ values for Refinement 3

	K_T			$E\%D$		
	Prop 4	Prop 3	Prop 2	Prop 4	Prop 3	Prop 2
x_1	0.228	0.244	0.245	-4.8	-12.5	-12.9
x_2	0.225	0.244	0.244	-3.8	-12.6	-12.6
x_3	0.224	0.242	0.242	-3.4	-11.3	-11.6
x_4	0.238	0.237	0.241	-9.9	-9.3	-11.2

Table D.9: Computed K_T and $E\%D$ values for Refinement 4

	K_T			$E\%D$		
	Prop 4	Prop 3	Prop 2	Prop 4	Prop 3	Prop 2
x_1	0.238	0.243	0.246	-9.6	-12.1	-13.3
x_2	0.239	0.241	0.244	-10.3	-10.8	-12.4
x_3	0.236	0.241	0.243	-8.7	-10.9	-12.0
x_4	0.231	0.238	0.242	-6.6	-9.8	-11.7

Table D.10: Computed K_Q and $E\%D$ values for Refinement 2

	K_Q			$E\%D$		
	Prop 4	Prop 3	Prop 2	Prop 4	Prop 3	Prop 2
x_1	0.0281	0.0296	0.0296	-0.8	-5.9	-6.1
x_2	0.0280	0.0296	0.0296	-0.5	-6.1	-6.0
x_3	0.0279	0.0294	0.0294	0.1	-5.3	-5.4
x_4	0.0291	0.0290	0.0293	-4.4	-4.0	-5.2

Table D.11: Computed K_Q and $E\%D$ values for Refinement 3

	K_Q			$E\%D$		
	Prop 4	Prop 3	Prop 2	Prop 4	Prop 3	Prop 2
x_1	0.0281	0.0295	0.0296	-0.7	-5.9	-5.9
x_2	0.0280	0.0296	0.0295	-0.4	-6.0	-5.9
x_3	0.0278	0.0294	0.0294	0.2	-5.2	-5.2
x_4	0.0291	0.0290	0.0293	-4.2	-3.9	-5.0

Table D.12: Computed K_Q and $E\%D$ values for Refinement 4

	K_Q			$E\%D$		
	Prop 4	Prop 3	Prop 2	Prop 4	Prop 3	Prop 2
x_1	0.0290	0.0295	0.0296	-4.1	-5.6	-6.2
x_2	0.0292	0.0293	0.0295	-4.6	-4.8	-5.7
x_3	0.0289	0.0293	0.0294	-3.6	-5.0	-5.6
x_4	0.0285	0.0291	0.0294	-2.3	-4.2	-5.3

E

Appendix : Grid Dependence Study for Self Propulsion

Table E.1: EFD results for C_T, K_T, K_Q and n

	EFD Results from NMRI			
	$C_T \times 10^3$	K_T	K_Q	n
Hull without ESD	4.811	0.217	0.0279	7.8
Hull with ESD	4.762	0.233	0.0295	7.5

Table E.2: Computed C_T, K_T, K_Q and n values for Case1.5a(NMRI), grids with Refinement 1

	Case 1.5a(NMRI)			
	$C_T \times 10^3$	K_T	K_Q	n
Grid 1	4.761	0.225	0.0278	7.59
Grid 2	4.783	0.220	0.0274	7.72
Grid 3	4.753	0.221	0.0274	7.66
Grid 4	4.724	0.233	0.0285	7.41
Grid 5	4.687	0.241	0.0292	7.25

Table E.3: Computed C_T, K_T, K_Q and n values for Case1.5a(NMRI), grids with Refinement 3

	Case 1.5a(NMRI)			
	$C_T \times 10^3$	K_T	K_Q	n
Grid 1	4.754	0.226	0.0279	7.57
Grid 2	4.761	0.227	0.0279	7.58
Grid 3	4.742	0.227	0.0279	7.55
Grid 4	4.734	0.229	0.0281	7.50
Grid 5	4.730	0.227	0.0280	7.51

Table E.4: Computed C_T, K_T, K_Q and n values for Case1.6a(NMRI), grids with Refinement 1

	Case 1.6a(NMRI)			
	$C_T \times 10^3$	K_T	K_Q	n
Grid 1	4.751	0.243	0.0291	7.34
Grid 2	4.739	0.240	0.0289	7.35
Grid 3	4.711	0.240	0.0290	7.31
Grid 4	4.691	0.247	0.0296	7.18
Grid 5	4.650	0.251	0.0300	7.07

Table E.5: Computed C_T, K_T, K_Q and n values for Case1.6a(NMRI), grids with Refinement 3

	Case 1.6a(NMRI)			
	$C_T \times 10^3$	K_T	K_Q	n
Grid 1	4.740	0.243	0.0292	7.31
Grid 2	4.740	0.243	0.0292	7.31
Grid 3	4.713	0.244	0.0292	7.27
Grid 4	4.704	0.246	0.0294	7.23
Grid 5	4.691	0.245	0.0294	7.22

F

Appendix : Local Flow Predictions

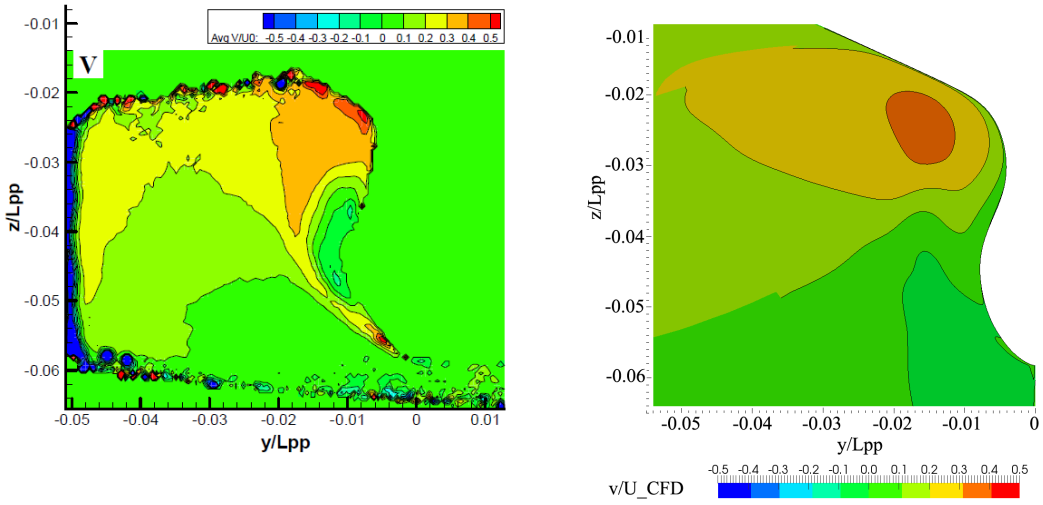

(a) v/U contours of the JBC without ESD from EFD

(b) v/U contours of the JBC without ESD from CFD

Figure F.1: EFD-CFD-Comparison for v/U contours at $x/L_{PP} = 0.96250$ for the JBC bare hull

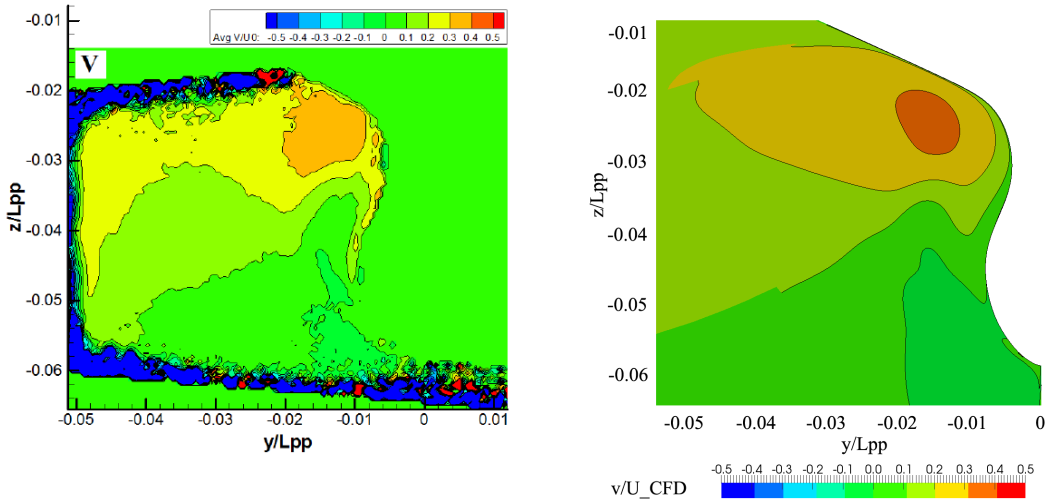

(a) v/U contours of the JBC with ESD from EFD

(b) v/U contours of the JBC with ESD from CFD

Figure F.2: EFD-CFD-Comparison for v/U contours at $x/L_{PP} = 0.96250$ for the JBC hull with ESD

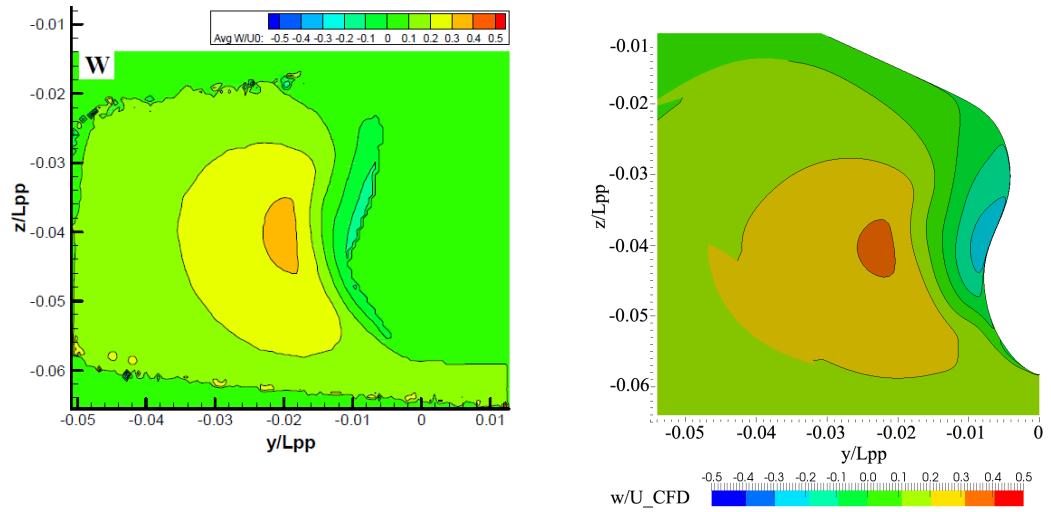

(a) w/U contours of the JBC without ESD from EFD

(b) w/U contours of the JBC without ESD from CFD

Figure F.3: EFD-CFD-Comparison for w/U contours at $x/L_{PP} = 0.96250$ for the JBC bare hull

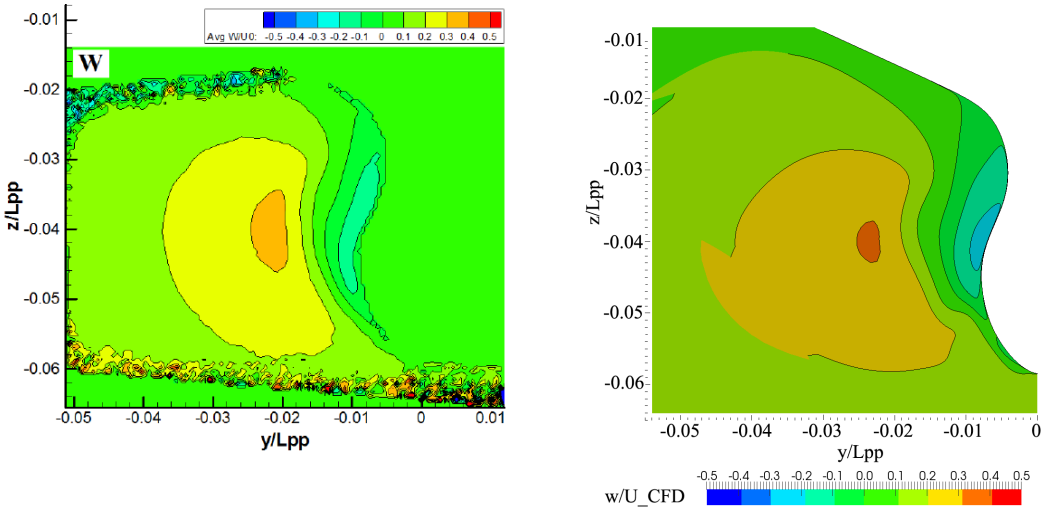

(a) w/U contours of the JBC with ESD from EFD

(b) w/U contours of the JBC with ESD from CFD

Figure F.4: EFD-CFD-Comparison for w/U contours at $x/L_{PP} = 0.96250$ for the JBC hull with ESD

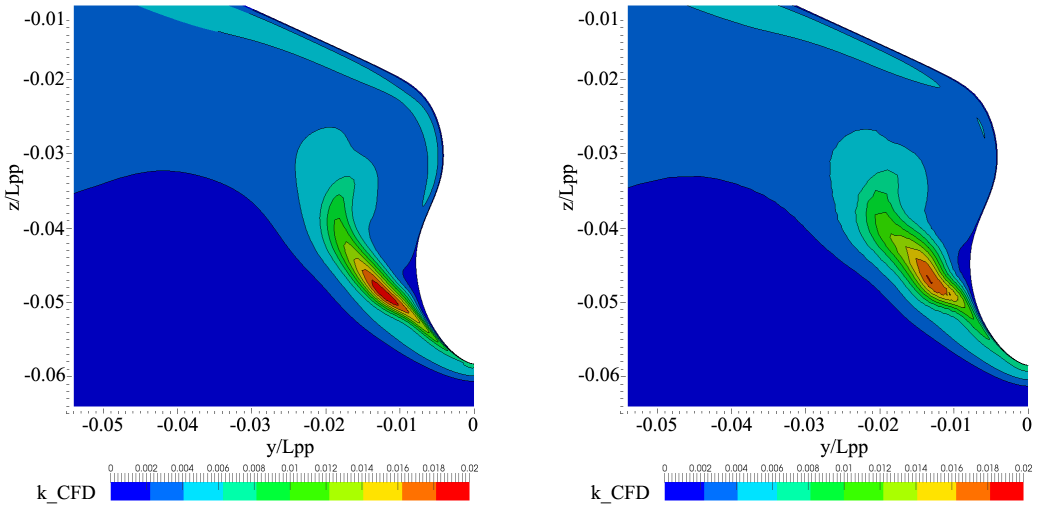

(a) k contours of the JBC without ESD

(b) k contours of the JBC with ESD

Figure F.5: Comparison for computed turbulent kinetic energy contours at $x/L_{PP} = 0.96250$ for the JBC bare hull with and without ESD

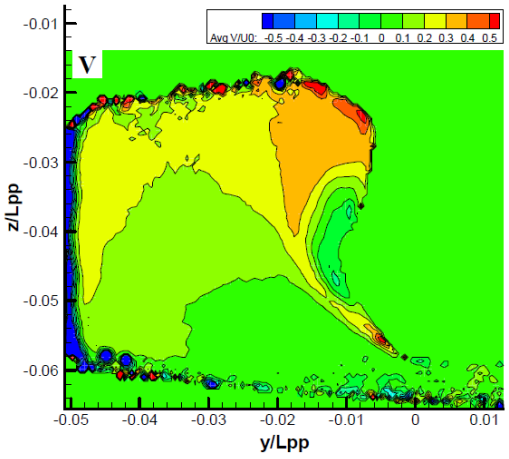

(a) v/U contours of the JBC without ESD from EFD

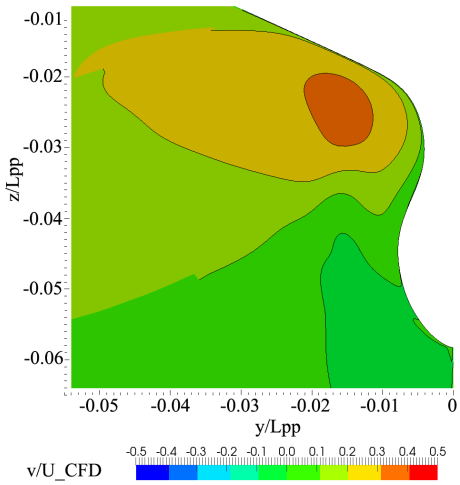

(b) v/U contours of the JBC without ESD from CFD

Figure F.6: EFD-CFD-Comparison for v/U contours at $x/L_{PP} = 0.98428$ for the JBC bare hull

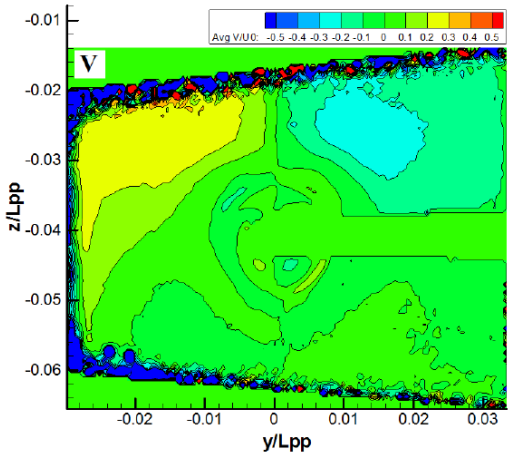

(a) v/U contours of the JBC with ESD from EFD

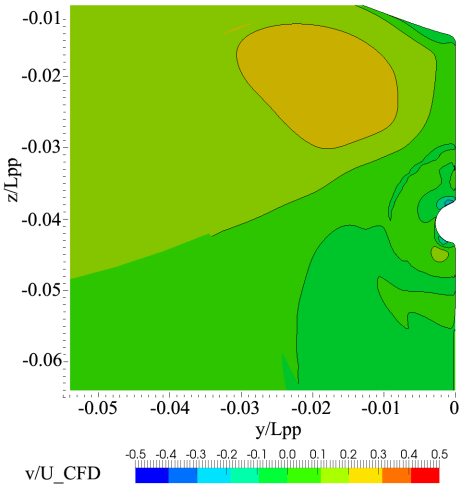

(b) v/U contours of the JBC with ESD from CFD

Figure F.7: EFD-CFD-Comparison for v/U contours at $x/L_{PP} = 0.98428$ for the JBC hull with ESD

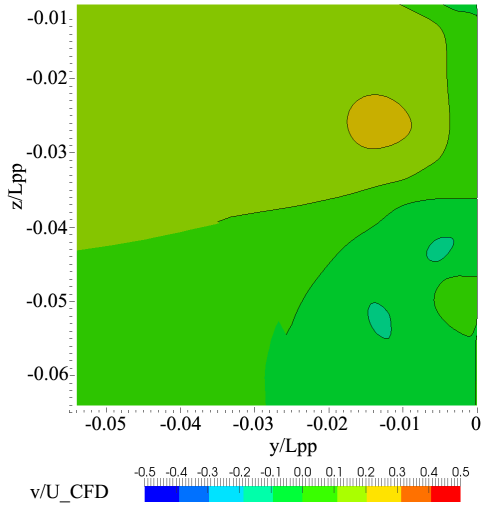

(a) v/U contours of the JBC without ESD

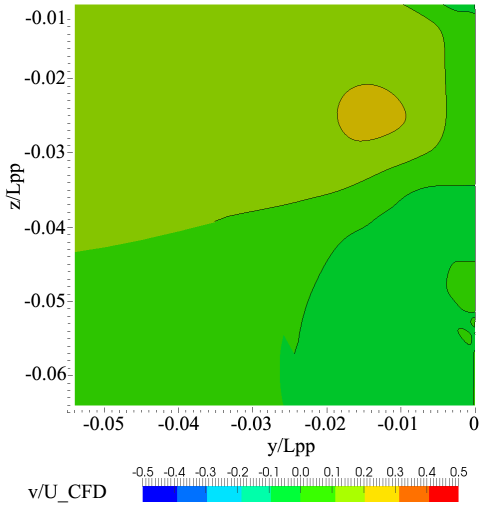

(b) v/U contours of the JBC with ESD

Figure F.8: Comparison for v/U contours at $x/L_{PP} = 1$ for the JBC with and without ESD

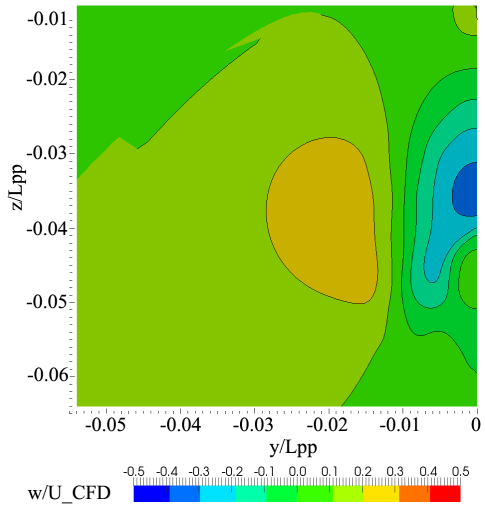

(a) w/U contours of the JBC without ESD

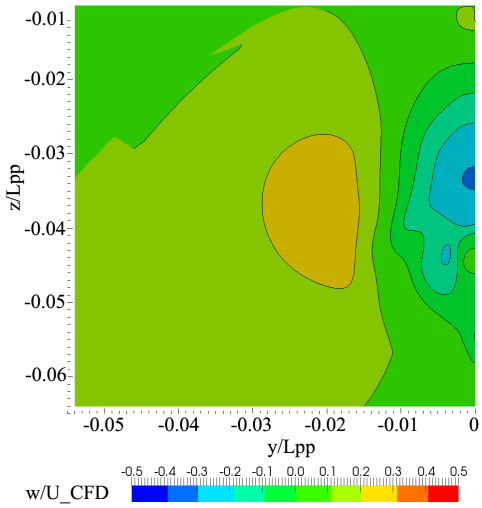

(b) w/U contours of the JBC with ESD

Figure F.9: Comparison for w/U contours at $x/L_{PP} = 1$ for the JBC with and without ESD